SYNTHESIS, MORPHOLOGY AND PROPERTIES OF POLYCRYSTALLINE GRAPHENE MEMBRANES

A Dissertation

Presented to the Faculty of the Graduate School

of Cornell University

in Partial Fulfillment of the Requirements for the Degree of

Doctor of Philosophy

by

Carlos Samuel Ruiz-Vargas

May 2013

SYNTHESIS, MORPHOLOGY AND PROPERTIES OF POLYCRYSTALLINE GRAPHENE MEMBRANES

Carlos Samuel Ruiz-Vargas, Ph.D.

Cornell University 2013

ABSTRACT

Graphene has recently emerged as a promising material for a wide range of potential applications, thanks to its outstanding electrical, mechanical, thermal and optical properties. This interest has fueled many efforts to establish methods for large scale graphene synthesis. One of the most promising scalable approaches is to obtain graphene on metal surfaces, most notably on copper, via chemical vapor deposition (CVD).

We have developed novel fabrication methods to obtain CVD graphene devices in large quantities. This allowed a thorough study of the polycrystalline structure in CVD graphene, as well as the characterization of mechanical and electrical properties, which are affected by graphene's grain structure. We found that grain boundaries are not the dominant factor in determining the electrical properties of devices. However, grain boundaries were observed to strongly affect graphene mechanical properties. For example, tearing and unzipping along grain boundaries were observed in graphene membranes, as a result of nanoindentation.

Finally, we have fabricated microcapsules featuring atomically thin windows made of reinforced double-layer CVD graphene. We have demonstrated the use of these windows for scanning electron microscopy (SEM) of samples in water. As proof of principle, we have imaged metallic nanoparticles in solution, with resolution and signal to noise ratio superior to those obtained with polyimide-based commercially available environmental cells.

BIOGRAPHICAL SKETCH

Carlos S. Ruiz-Vargas was born in 1983, in Puebla, Mexico. After living in various cities, most notably Cuernavaca, and later Merida, his family briefly visited the United States in 1999 (his parents travelled to Princeton, NJ for a sabbatical stay). It was around this time that Carlos started considering studying outside of Mexico after high school. He arrived in Ithaca, NY in 2002, to commence his studies at Cornell University. Little did he know that ten years later he would still be in Ithaca. He obtained his BA in January 2006 majoring in physics.

After a few months backpacking through Europe, Carlos returned to Cornell in August 2006, enrolling in the Master of Engineering program, in engineering physics. For his masters research project, Carlos joined Jiwoong Park's research group, and started working on his first graphene project. Carlos completed the M.Eng degree in 2007, but instead of going elsewhere, Carlos stayed in the Park group to pursue a PhD in applied physics, continuing to work on graphene. He was partially supported for most of his doctoral studies by a CONACyT fellowship (Mexican government funded, Consejo Nacional de Ciencia y Tecnologia). After completing his PhD, he will travel to Switzerland to work as a postdoctoral fellow at ETH Zurich.

A mi padres

ACKNOWLEDGMENTS

First, I would like to thank Jiwoong Park, who in 2006 gave me the opportunity to join his newly created research group, and then again in 2007 gave me the opportunity to stay in his group as a PhD student. Since Jiwoong had just arrived at Cornell University, there were no senior graduate students in his group to immediately mentor me. He had to bear with even the most basic of questions, with great patience and care. Through the years, witnessing how Jiwoong built up his research group, with patience, diligence, curiosity and impressive talent has been an incredible experience. I am ever so grateful for his support and patient mentoring.

I would also like to thank other professors from whom I have learned a great deal during my time at Cornell. I would like to thank Paul McEuen (one could say he is my "academic grandfather", having previously been Jiwoong's adviser), David Muller, Farhan Rana, Michael Spencer. Of course, I would also like to thank Dan Ralph and Richard Hennig, who are part of my final special committee.

It was incredibly fortunate that my labmates were not just people I was able to learn from in lab, but also outside of it, developing friendships that made the time spent in Ithaca not just bearable, but truly enjoyable. Mark Levendorf and Wei Tsen have been a constant for many years, in the good and bad times, and more recently also Lola Brown and Robin Havener. While distance might take a toll once we go in separate directions, the bonds formed will not be torn. Robert Hovden is not in our group, but I will thank him now as well. It was great living with him the first few years of graduate school. We shared many academic pains and joys. I would also like to thank Lihong Herman, Michael Segal, Daniel Joh, Chuljoo Kim, Sang-Yong Ju, and undergraduate students Shivank Garg and Michal Wojcik, and the rest of the Park group.

I have interacted and learned from many students during my time at Cornell outside of the Park research group. The first student to show me the ropes as I started to work with graphene was Arend van der Zande. This did not stop after the first few years, and collaborating with him was one of the determining factors in the completion of my PhD work. Other students from other research groups, with whom collaborations were crucial in many collaborative research efforts, are Pinshane Huang and Houlong Zhuang, not only bringing expertise in electron microscopy and molecular simulations, respectively, but also enthusiasm and insight.

There are many more people I have had the enormous pleasure to meet, interact with and learn from. I would like to thank Samantha Roberts, Melina Blees, Jonathan Alden, Nathan Gabor and all of the wonderful "McEuen-ites" I have had the pleasure of knowing. I would also like to thank Shriram Shivaraman, Robert Barton, Thomas Alava, Haining Wang and Jared Strait. Among many other people, I should mention Rob Ilic, Dan Woodie, Ed Camacho and Daron Westly, who answered countless questions and gave countless suggestions when dealing with the joys and frustrations of fabrication at the CNF.

Other people have also played important roles during my time in graduate school: Brian B., David H, Nichole N., Thea W., and many others. Of course, there's also the "white house" dudes, who gave me a second home: Justin, Watsan, Vikram, Ben, Phil, Alisa, Daniel, Nikolas, Gayane and many more (and of course, Levon A., who we all miss immensely).

Finally, I would like to thank my family. My parents have given me unconditional support throughout my life. I can only hope to one day do in my life what they have done in theirs. And my siblings, Andres and Sofia, make of this world a more enjoyable place to live in.

Thank you all.

TABLE OF CONTENTS

PREFACE

It seems innately human to be fascinated by extremes. It appears that in our search for knowledge, we seek to define bounds on what is possible in this world (and universe). By limiting what is possible, whether accurately or not, we give room to our imagination to freely roam and fill in our perceived gaps of understanding. Our fascination for extremes is not always rewarded with absolute limits. This is not the case for graphene. One cannot make a crystal any thinner than one layer of atoms and this limit is realized in graphene. By understanding its properties, we can explore many of the implications and potential uses of having reached the ultimate limit in reducing the thickness of a material.

CHAPTER 1

INTRODUCTION

1.1 Nano, in science and technology

During a speech at a meeting of the American Physical Society, in the closing days of 1959, the late Richard Feynman pondered on the fantastical possibilities of a new field in which very small things, even molecules and atoms, could be manipulated and controlled [1]. While the term 'nanotechnology' had still not been coined, Feynman’s speech has been often credited for providing inspiration for the development of a new field. Regardless of the actual influence this speech may or may not have had, on subsequent efforts to push the boundaries of fabrication and characterization of old and new materials into the nanoscale, an air of fantastical yet achievable development makes nanotechnology an attractive area of study.

Nanotechnology relies on the application of many fields within physics, chemistry and biology, to manipulate materials and fabricate structures in which one or more of their dimensions are limited to the nanoscale. The motivation for such manipulation and control is manifold. On one hand, interesting quantum phenomena become relevant in materials and structures with restricted dimensions. On the other hand, the bulk properties of materials can be tailored, through advances in synthesis and fabrication, to address specific needs for the potential development of applications in areas such as electronics, medicine, energy conversion and storage, materials development, among others.

1.1.1 Carbon nanostructures

The study of carbon nanostructures has developed as a prolific subfield of materials research. Since the discovery of fullerenes in 1985 (R. Smalley *et al.*) [2], and nanotubes not much later (S. Ijima) [3], carbon nanostructures have been the subject of extensive investigation. While these structures had been investigated in previous decades [4], interaction between researchers in different parts of the world was quite limited, so most reports did not attract much attention. This changed in the 1990s, when series of nanoscience and nanotechnology initiatives began increasing collaboration between researchers interested in these new structures, and a fruitful conversation between theoretical predictions and experimental observations solidified. By the time the pioneering graphene work surfaced in 2004 (Novoselov *et al.)* [5], a large number of people were already interested in the field, and were able to appreciate the significance of the latest developments. Many researchers were eager to jump right in and the field grew even more.

The field has benefitted from wide coverage not only from scientific journals, but also from public media, further contributing to an expanding recognition. While this could be a double-edged sword, as unrealistic expectations can often develop from uninformed coverage from the mass media, the potential of new applications has certainly allowed for an important flux of funding both from government agencies as well as the private sector.

1.2 Graphene: 2D in 3D

Graphene is made of carbon atoms arranged in a honeycomb lattice. Each carbon atom in graphene is bonded to its three nearest neighbors by strong sp^2 bonds, with bond length of 1.42Å. The remaining 2p electron in each carbon atom contributes to π-orbitals. One significant advantage for graphene, in comparison to other carbon nanostructures, is that in all but one dimension, graphene can extend to micrometer scales and beyond. As this made its identification and characterization easier, graphene has allowed for a much more practical platform to study the properties of carbon nanostructures.

Graphene is commonly described as a 2-dimensional material, because one only needs two dimensions to describe the positions of the carbon atoms in its lattice. However, graphene exists in a 3-dimensional space. Graphene can be thus considered as the building block for creating other graphitic forms, taking advantage of that extra dimension. For example, graphite is composed of graphene sheets vertically stacked. Graphene can also bend: if rolled onto itself, it can form nanotubes, and if wrapped into a sphere it can form fullerenes such as C_{60}.

Also pertaining to graphene's 3-dimensional existence, and of great relevance to this thesis, is the fact that graphene can stretch and bend. It can, seemingly effortlessly, conform to a surface, folding and climbing over steps and edges, or also hang freely with the help of a supporting substrate. It can vibrate like a drumhead, and it can ripple like the plastic wrap on a food dish. However, graphene too has its limits. Understanding what graphene can withstand, mechanically, chemically and

electrically is of great importance in the design of new graphene structures and devices.

Finally, even a perfectly flat graphene sheet is a 3-dimensional object. After all, the diameter of one atom is still a finite number, and graphene has a measurable thickness. Graphite's interlayer distance, 3.42Å, is widely used as the thickness of

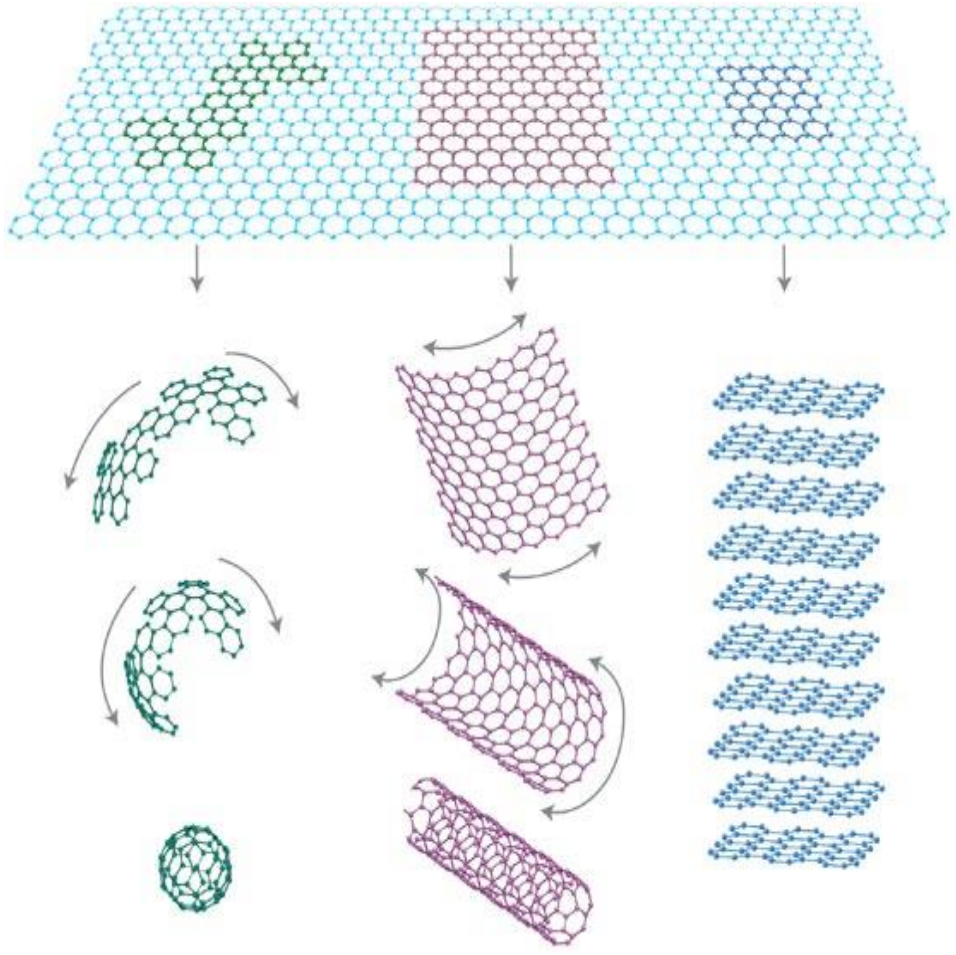

Figure 1.1 Graphene, the so called mother of all graphitic forms. Graphene can be stacked into multilayer graphite, rolled into nanotubes. It can also form buckyballs (from [6]).

one graphene layer. To compare its properties to those of a bulk material, one can use a simple relation. Given a physical property A_{2D}, with units per area, the corresponding 3D property, A_{3D}, with units per volume, will be given by:

$$A_{3D} = {}^{A_{2D}}/_{t} \tag{1.1}$$

Here, t is the thickness of the membrane, and it can vary if one is dealing with multiple graphene sheets stacked on top of each other. When multi-layer graphene is thick enough, its properties eventually can be described as those of bulk graphite.

1.3 From graphite to graphene

Before describing some of the properties that have contributed in propelling graphene research, it is important to look back to see what were some of the early steps in the discovery of this material (useful aids for this purpose are the many review articles on graphene, such as A. Geim and K. Novoselov's "The rise of graphene" [6]). Graphene had been studied theoretically for many decades [7,8], but it was not believed to exist in an isolated state [9]. In fact, 2D crystals had been argued to be thermodynamically unstable. Atomic monolayers were only known as part of bulk structures, existing as the capping layer of a 3D crystal, or at the interface of two crystals [10], but had not been observed supported by an amorphous substrate or freely-suspended.

When looking back at graphene's history, a good starting point may be the observation by Benjamin Brodie, who in 1859 described what he thought was a new form of carbon, which he called 'graphon' [11]. Brodie obtained his samples by exposing graphite to strong acids. As we now know, a process like this would yield

small graphene oxide crystals suspended in solution. More than a century later, U. Hofmann and Hanns-Peter Boehm, building on previous work, claimed to have identified on a TEM grid, graphite oxide fragments as thin as a single layer. It was Boehm and his colleagues who in 1986 coined the term ‘graphene’ [12].

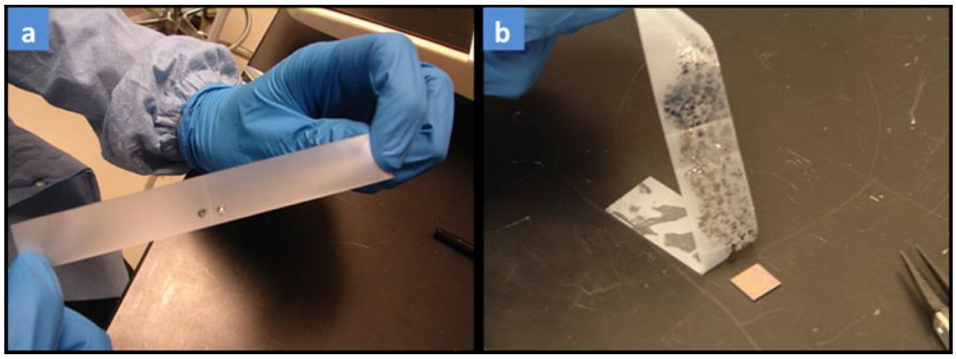

Figure 1.2 a) Starting with a graphite flake, on a piece of adhesive tape b) the flake is peeled off several times resulting in many more flakes, with decreasing thickness. What is seen in b) is finally rubbed and pressed down onto a receiving substrate (from [29]).

There had been earlier attempts to obtain thin layers of graphite by exfoliation. Graphite layers which were thin enough to be optically transparent were already reported in 1990 [13]. R. Ruoff also attempted to exfoliated thin graphene from graphite pillars [14]. However, it was not until a series of papers in 2004 and 2005 that graphene attracted the attention beyond the limits of the previously established community [5,15,16]. While it seems that many researchers were heading in the right direction, A. Geim's group reported an easy method for obtaining very thin graphitic films on oxidized silicon wafers. The new method consisted of

exfoliating a few layers of graphene from a high quality graphite crystal, such as highly oriented pyrolytic graphite (HOPG) or Kish graphite (a byproduct of steelmaking, which resembles natural graphite). The exfoliation was done with sticky tape (Scotch tape), and it required repeating the process many times until very thin flakes were present on the tape. Finally, the sticky tape can be pressed down and rubbed onto a receiving substrate (Figure 1.3), where thin flakes can be searched for optically.

Two important aspects seemed to combine to rapidly generate a great amount of interest in graphene. First, the method was exceedingly simple, so a minimal amount of equipment and resources were needed for any group to attempt obtaining their own graphene samples. Second, the pioneering papers of 2004 and 2005 went beyond reporting the observation of these thin graphite sheets. Since their method yielded graphene ideally placed on a substrate, this facilitated further studies such as the investigation of the electric field effect on graphene's conductance. A. Geim, and a member of his group, K. Novoselov, went on to win the Nobel prize in physics for their work. In 2005, this group and a group at Columbia University [15,16] further demonstrated that charge carriers in graphene obeyed a quantum mechanical behavior known as the quantum Hall effect. These reports made many researchers, who previously thought of graphene as just a niche and interesting topic, pay close attention.

1.4 Seeing graphene

When making very small things, one must be able to see very small things. Many advances in nanotechnology and related fields have been fueled by our ability

to image microscopic objects. At the same time, many needs in nanotechnology have likewise fueled efforts to improve imaging techniques. As discussed earlier, graphene is thin but not necessarily small (the first exfoliated graphene samples were as large as 10 microns), with lateral dimensions well within the resolution limits of optical microscopy.

1.4.1 Optical approach

At first glance, optically imaging a single layer of atoms seems a difficult task. The optical absorbance of graphene is known to be 2.3% over a broad range of frequencies including the visible spectrum, and is given by a simple relation, $\pi\alpha$, where α is the fine structure constant (~1/137) [17].

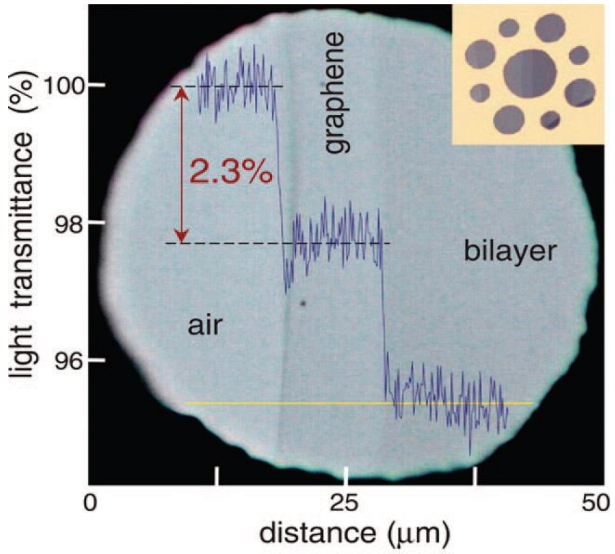

Figure 1.3 Optical transmittance of graphene, with each layer absorbing 2.3% (from [17]).

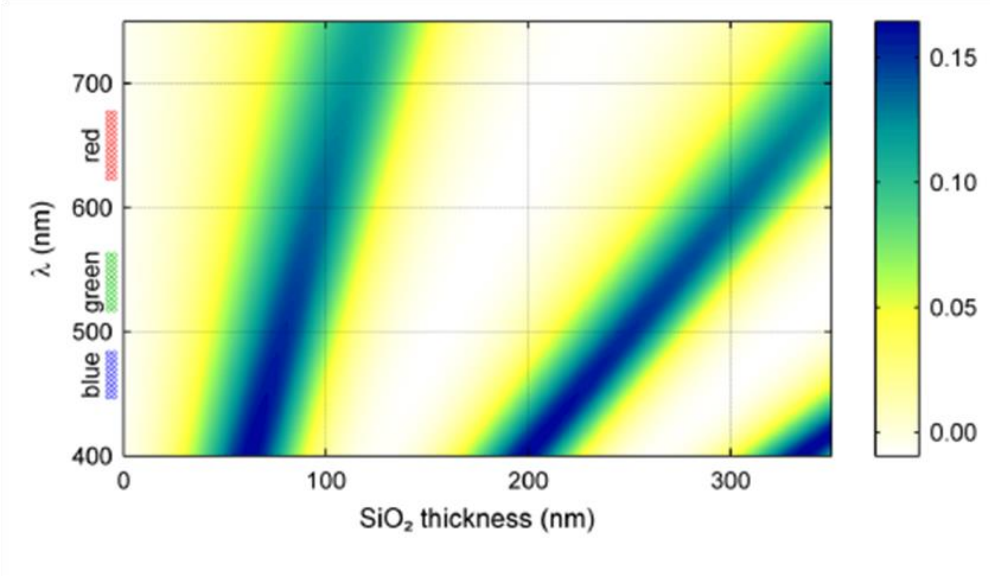

Figure 1.4 Optical contrast as a function of oxide thickness and illumination wavelength, for a single layer graphene on an oxidized silicon wafer [18].

While 2.3% is not enough light absorption for direct visualization under most conditions, interference effects can make it easier to identify even a single layer of graphene. Silicon wafers with a 285nm layer of SiO_2 became the standard substrate to identify graphene in a conventional optical microscope under white light illumination [18]. It was found that the index of refraction of graphite, $n = 2.6 - 1.3i$, was sufficient to describe the optical contrast observed on oxidized Si wafers.

The optical contrast, defined as a relative intensity of reflected light in the presence of single layer graphene, compared to the intensity of reflected light from a bare substrate, is shown in Figure 1.4. It is derived from a simple multilayer interference model. Figure 1.5 shows examples of experimental observations. This simple technique allowed many researchers around the globe to rapidly prepare graphene samples for further studies.

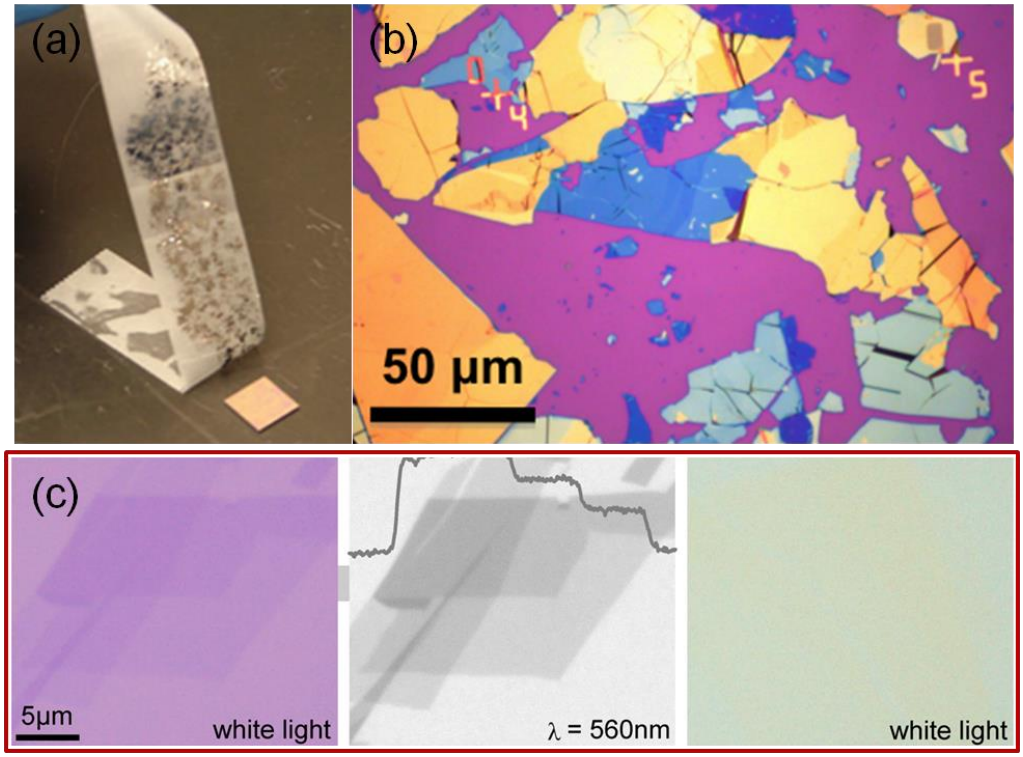

Figure 1.5 a) Scotch tape with thin graphite flakes [29]. b) Exfoliated graphite on a thermally oxidized silicon wafer surface. Most flakes seen here are thick [29]. c) Optical images of few layer graphene and single layer graphene, as seen on a Si wafer with a 285nm SiO_2 layer under white light (left) under green light (center) and a different sample on a 200nm SiO_2 layer [18].

1.4.2 Non-optical eyes

The resolution limits of optical microscopy are well known, so additional imaging techniques are useful to image at the nanometer scale. The early electron microscope was designed and built in the early 1930's (Figure 1.6). Within a decade, the resolution obtained by conventional optical microscopy was surpassed [19], and commercial electron microscopes became available, including scanning electron microscopes. Another important development, in 1981, was the invention of the scanning tunneling microscope [20], the first scanning probe microscope. The main

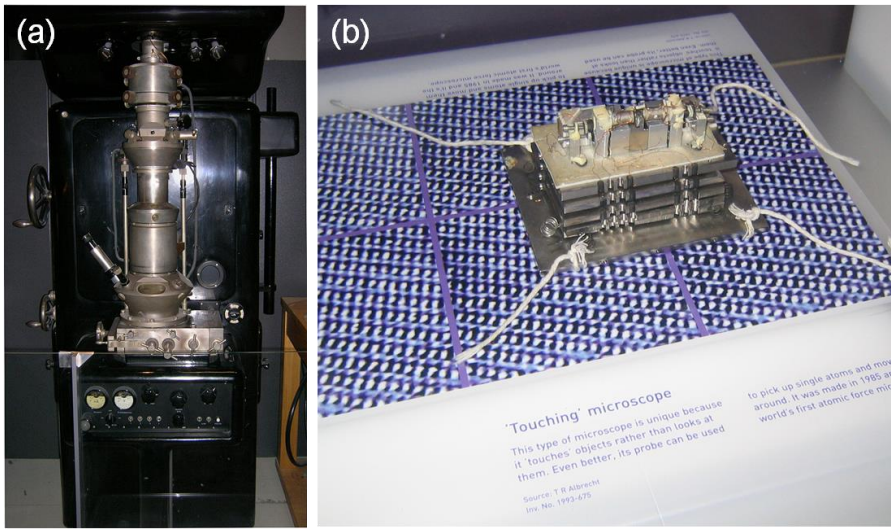

Figure 1.6 a) Replica of 1933 electron microscope, which was the first to surpass the resolution power of optical microscopy, with a magnification of 12,000 (from [30]). b) First atomic force microscope, in display in London's Science Museum, in the UK (from [30]).

feature of scanning probe microscopes is a tip scanned over a sample with very high spatially precise piezoelectric components. The tip's motion, or other measurable properties such as electric transport through the tip, are affected by physical and chemical interactions with the sample. These are recorded generating high resolution images, where different properties of the sample can be mapped. Another well known scanning probe microscope is the atomic force microscope (AFM), such as the one shown in Figure 1.6. With an AFM, the surface topography can be obtained, and various mechanical properties studied with nanometer scale resolution. The results presented in this thesis have used both electron microscopy, and atomic force microscopy techniques.

1.5 From carbon to graphene

A different route towards obtaining graphene is to grow it from smaller building blocks, rather than taking graphite apart. Several promising synthesis methods have been reported in this fashion. For example, graphene can be grown epitaxially from SiC [21], where carbon is provided by the solid underlying substrate.

1.5.1 Graphite on metal surfaces

Another method relies instead on precipitation or aggregation of carbon onto the surface of a metal surface, either from impurities in the metal, or from gaseous or solid sources. Perhaps the earliest work in this direction was the observation of graphene on the surface of ruthenium [22] and on the surface of nickel [23].

For graphene grown on nickel, J.M. Blakely and co-workers at Cornell University found that carbon impurities can segregate to the surface of a nickel substrate after thermal cycling, forming a graphitic layer, as shown in Figure 1.7 [24]. In those days, however, carbon was an unwanted presence on the surface of these metals.

The interaction of each graphene layer with each other, in graphite, is quite weak in comparison with the extremely strong carbon-carbon bonds (~7.4 eV per carbon atom). This also holds true for the interaction of graphene with most transition metals serving as an underlying substrate. The weak van der Waals interactions are less than 100 meV per atom [25]. An implication of this is that one can remove the metal substrate from underneath, usually by chemical etching, leaving graphene relatively undamaged.

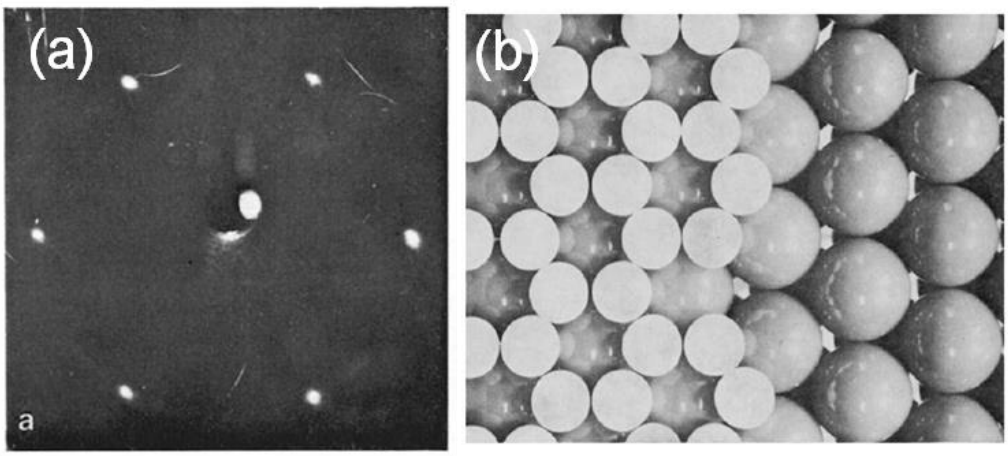

Figure 1.7 a) Hexagonal pattern obtained by LEED, from the surface of a (111) nickel surface. b) Ball model of the proposed arrangement of the first layer of carbon atoms on the nickel surface, showing the characteristic graphene honeycomb lattice (from [24]).

1.5.2 Graphene growth on copper

While most of the early work on graphite growth on metal received very little attention, soon after the initial "graphene-rush" of the early 2000s, the idea of getting graphene from metal surfaces was revisited with rapid success. This time, the importance of transferring graphene to arbitrary substrates was recognized, decoupling it from the metal substrate from which it was synthesized.

First, the direct growth of graphene on thin nickel films and subsequent transfer was reported by a few research groups [26,27]. Variations of this transfer protocol will be described in detail throughout this thesis. The results from graphene

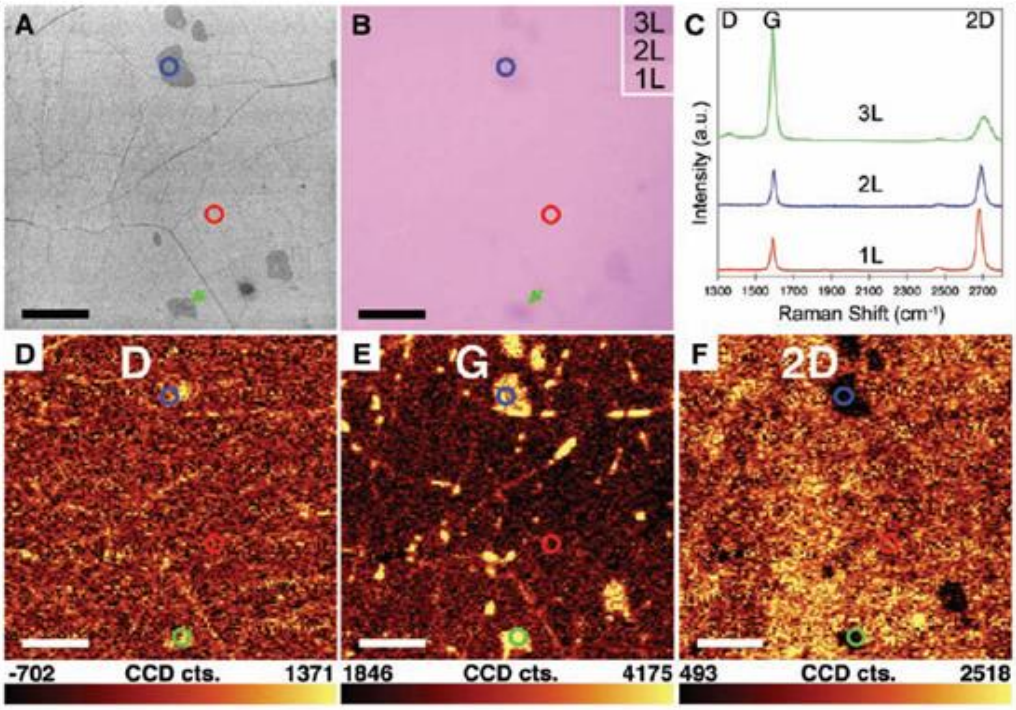

Figure 1.8 SEM, optical and Raman imaging of single layer graphene grown on copper, reported by Li *et al.* (from [28]).

grown on nickel showed excellent physical properties, most notably the quantum Hall effect [27]. It was also shown that further optimization leads to the formation of nearly 90% in area of single or double layer.

Soon after, it was shown that copper foil was an even better substrate for growing single layer graphene films [28]. Not only copper is an inexpensive alternative in comparison to other metals, it is also easily removable by etchants which do not chemically affect graphene. And most importantly, due to a very small solubility of carbon in copper, the carbon deposition process was found to be largely self limiting [28], producing mostly single layer graphene (Figure 1.8) with promising electrical properties.

The work on this thesis was done on graphene grown on copper surfaces, via chemical vapor deposition (CVD). 'CVD graphene' is now a commonly used term to distinguish this material from exfoliated graphene. Details of the synthesis and fabrication will also be discussed in detail in later chapters.

1.6 Thesis summary and outline

This thesis discusses and exploration of the properties CVD graphene as a new 2D material. One could naively assume that CVD graphene will behave exactly like its exfoliated counterpart. However, new synthesis and fabrication methods bring about many questions and technical challenges that must be addressed.

This introductory chapter has purposefully avoided technical and scientific details. In Chapter 2, the physical and chemical properties of graphene will be reviewed. Graphene's properties are largely responsible for an explosion in interest

and research efforts all around the world. Of great relevance to this thesis is that thanks to its remarkable physical strength graphene can be freely-suspended.

Chemical vapor deposition has emerged as a powerful approach for the large scale production of graphene. In Chapter 3, the chemical vapor deposition (CVD) route to obtain graphene will be reviewed, together with several fabrication techniques to produce CVD graphene devices. Chapter 4 presents an AFM study, which aims to understand CVD graphene's topography and mechanical properties. The mechanical properties of CVD graphene are compared to those found in exfoliated graphene. We find that graphene's polycrystalline nature plays an important role, affecting graphene's properties. Chapter 5 presents one of the first detailed investigations of CVD graphene structure, further confirming that CVD graphene is polycrystalline. Finally, Chapter 6 will explore the use of CVD graphene membranes as electron transparent windows, addressing the potential application of electron microscopy of samples in water with graphene-based environmental cells.

Chapters 3 through 6 are, in their majority, adapted from the following manuscripts (* denotes authors with equal contribution):

Chapter 3 -- M.P. Levendorf*****, C. S. Ruiz-Vargas*****, S. Garg, and J. Park, "Transfer-Free Batch Fabrication of Single Layer Graphene Transistors", ***Nano Letters*** 9, 4479-4483 (2009).

Chapter 4 -- C. S. Ruiz-Vargas, H. Zhuang, S. Garg, P. Y. Huang, A. M. van der Zande, P. L. McEuen, D. A. Muller, R. Hennig, and J. Park, "Softened elastic response and unzipping in CVD graphene membranes," ***Nano Letters*** 11, 2259-2263 (2011).

Chapter 5 -- P. Y. Huang*****, C. S. Ruiz-Vargas*****, A. M. van der Zande*****, W. S. Whitney, M. P. Levendorf, J. W. Kevek, S. Garg, J. S. Alden, C. J. Hustedt, Y. Zhu, J. Park, P. L. McEuen, D. A. Muller, "Grains and Grain Boundaries in Single-Layer Graphene Atomic Patchwork Quilts," ***Nature*** 469, 389-392 (2011).

Chapter 6 -- C. S. Ruiz-Vargas, M. Wojcik, and J. Park, "Graphene windows for low-voltage scanning electron microscopy of samples in water," ***(unpublished)***.

REFERENCES

[1] R. P. Feynman, J. of Microelectromechanical Systems, 60 (1992).

[2] H. W. Kroto, *et al.* Nature **318**, 162 (1985).

[3] S. Iijima, Nature **354**, 56 (1991).

[4] R. Bacon, *et al.* J. Appl. Phys. **31**, 283 (1960).

[5] K. S. Novoselov, *et al.* Science **306**, 666 (2004).

[6] A. K. Geim, *et al.* Nat Mater **6**, 183 (2007).

[7] P. R. Wallace, *et al.* Phys. Rev. **71**, 622 (1947).

[8] J. C. Slonczewski, *et al.* Phys. Rev. **109**, 272 (1958).

[9] F. D. M. Haldane, *et al.* Phys. Rev. Lett. **61**, 2015 (1988).

[10] J. A. Venables, *et al.* Rep. Prog. Phys. **47**, 399 (1984).

[11] B. C. Brodie, Philosophical Transactions of the Royal Society of London **149**, 249 (1859).

[12] H. P. Boehm, *et al.* Carbon **24**, 241 (1986).

[13] K. Seibert, *et al.* Phys. Rev. B **42**, 2842 (1990).

[14] X. Lu, *et al.* Appl. Phys. Lett. **75**, 193 (1999).

[15] K. S. Novoselov, *et al.* Nature **438**, 197 (2005).

[16] Y. Zhang, *et al.* Nature **438**, 201 (2005).

[17] R. R. Nair, *et al.* Science **320**, 1308 (2008).

[18] P. Blake, *et al.* Appl. Phys. Lett. **91**, 063124 (2007).

[19] E. Ruska, Kolloid Z. **100**, 212 (1942).

[20] G. Binnig, *et al.* Appl. Phys. Lett. **40**, 178 (1982).

[21] C. Berger, *et al.* J Phys Chem B **108**, 19912 (2004).

[22] J. T. Grant, *et al.* Surf. Sci. **21**, 76 (1970).

[23] J. M. Blakely, *et al.* J. Appl. Phys. **41**, 2693 (1970).

[24] J. C. Shelton, *et al.* Surf. Sci. **43**, 493 (1974).

[25] M. Vanin, *et al.* Phys. Rev. B **81**, 081408 (2010).

[26] A. Reina, *et al.* Nano Letters **9**, 30 (2009).

[27] K. S. Kim, *et al.* Nature **457**, 706 (2009).

[28] X. Li, *et al.* Science **324**, 1312 (2009).

[29] van der Zande, A. PhD Thesis. Cornell University (2011).

[30] Wikipedia Commons (accessed 2012).

CHAPTER 2

CHARACTERIZING GRAPHENE'S PROPERTIES

2.1 Before CVD graphene

In this chapter, we review some of the techniques which have been used to characterize graphene [1], including the approaches and results most relevant to this thesis. These techniques have become valuable tools for exploring the properties of CVD graphene.

2.2 Determining thickness

As reviewed in Chapter 1, one of the most approachable ways of detemining the approximate thickness of a graphitic sample is by evaluating its optical reflection on a known substrate, or the transmittance of light if the substrate is transparent (or graphene is suspended). For example, a trained eye will be able to identify single layer graphene on a 285nm SiO^2/Si substrate, as a faint purple shade, barely darker than the bare substrate.

However, to be confident with a qualitative evaluation of thickness, one must complement these observations with quantitative measurements that directly measure the number of layers of a graphene sample. If the substrate is transparent, or the sample is freely suspended, optical absorption measurements can be performed. However, this is not always possible, so other methods are often employed.

2.2.1 Atomic force microscope

One useful tool for determining thickness is the atomic force microscope (AFM). An AFM operates by manipulating an extremely sharp tip over a relatively flat sample. This tip is located at one end of a cantilever, and its vertical position is optically monitored by a laser's reflection on a photodiode. For imaging, the position of the cantilever relative to the sample is controlled in all directions. Figure 2.1 is a basic AFM schematic. The simplest mode of operation for an AFM is the contact mode, where the tip is pushed against the sample. A feedback mechanism maintains the deflection of the cantilever constant, while scanning the tip, obtaining a topographic image.

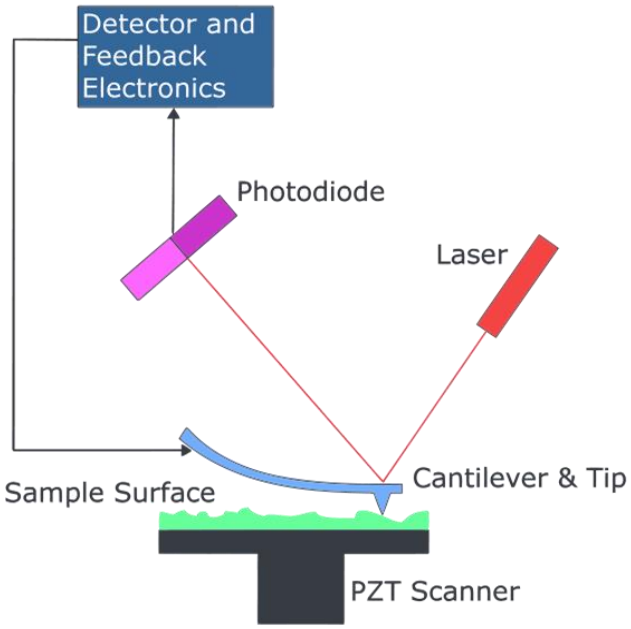

Figure 2.1 Simplified schematic of AFM operation [12].

A more gentle approach is the tapping mode, which allows the cantilever to oscillate at its resonance frequency. As the oscillating cantilever approaches the sample, the amplitude of oscillation is reduced. Similarly to the contact mode, a feedback mechanism adjusts the vertical position of the cantilever, keeping the oscillation amplitude constant. If this is done while the sample (or the cantilever) is being scanned, a topography map can also be obtained.

An example of an AFM image of a graphene flake is shown in Figure 2.2. Here, a single layer of graphene was imaged on a silicon dioxide surface. The thickness of this particular graphene sample was measured to be ~0.9 nm. However, the graphene folds reveal an increase in height much closer to inter-layer spacing of

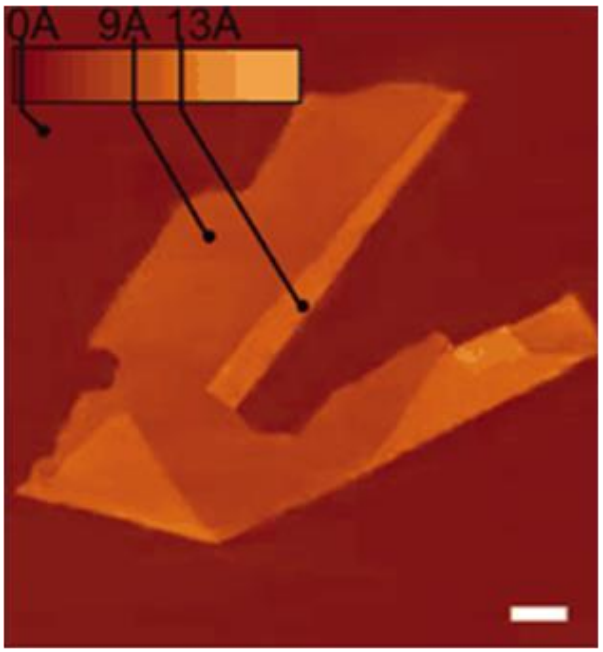

Figure 2.2 AFM height image of a single layer of graphene, folded onto itself. Scale bar: 1 micron. (from [1]).

graphite (0.34 nm). The discrepancy in height with respect to the inter-layer spacing is attributed to differences in van der Waals distances for different substrates, as well as adsorbates trapped at the silicon oxide/graphene interface. Height measurements of single layer graphene can vary in the range of 0.6-1.0 nm.

2.2.2 Raman spectroscopy

While scanning probe methods are ideal to study 2-dimensional crystals, these techniques can be time consuming. Raman spectroscopy is one alternative approach which has proved to be useful for the quick characterization of graphene samples [2]. This optical method relies on the detection of photons inelastically scattered by the sample due to electron-phonon interactions, thus providing information on its electronic and phonon degrees of freedom. A sample is illuminated with light of a particular wavelength, and small shifts in the energy of a small portion of photons, which are scattered inelastically, are measured.

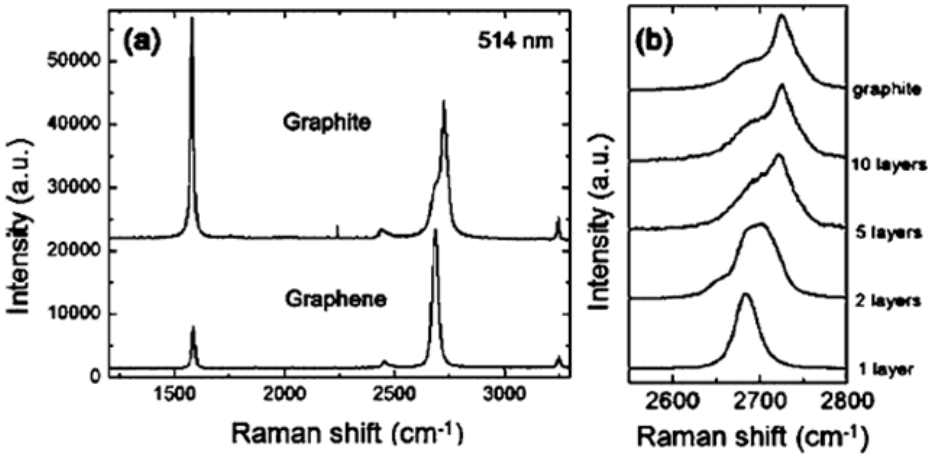

Figure 2.3 a) Raman spectra of graphite and single layer graphene.

b) Spectra as a function of thickness ([2]).

.

As graphene's electronic band structure changes with the stacking of additional layers, the way photons interact with graphene by coupling with various phonon modes can be used as "fingerprints". This is a useful route to rapidly determine the thickness of Bernal stacked graphene samples.

The main features in a Raman spectrum of graphene are the 2D (also known as G') peak at roughly 2700 cm^{-1}, the G peak at ~1584 $cm^{-1,}$ and the D peak at ~1350 cm^{-1}. The characteristics of the first two modes are summarized in the results by Ferrari *et al.*, shown in Figure 2.3. The G peak is caused by in-plane carbon-carbon bond vibrations, and the 2D peak is caused by a double-resonance scattering mechanism. Variations in thickness in a graphene sample will give rise to changes in the position and relative intensities of the 2D and G peaks. The 2D peak also changes shape, as for graphite samples this peak is actually composed of multiple convoluted bands. The D peak, due to graphene's breathing mode, is suppressed due to its hexagonal symmetry, except in cases where graphene's symmetry is broken by defects in the lattice. Thus, Raman spectroscopy is not only useful to determine the thickness, but also the quality of a particular sample.

2.2.3 Other methods

In addition to the methods previously described, there are more specialized modes which can be at times more appropriate. In the family of scanned probe techniques, for example, the scanning tunneling microscope (STM) can provide atomic resolution information on the local electronic density of states in a sample. While this information is of high scientific valuable, this technique is less versatile

due to the scanning size restrictions, as well as the requirement for ultra-clean and flat samples.

More relevant to this thesis, however, are the transmission modes of electron microscopy: transmission electron microscopy (TEM) and scanning transmission electron microscopy (STEM). These two techniques provide direct evidence regarding the thickness and stacking order of a sample. They can also probe the crystallographic orientation and structure. Furthermore STEM can provide atomic resolution, as it will be discussed in Chapter 5.

2.3 Electronic properties

We will now address some of the properties that make graphene an interesting material. One basic electric property of a two-dimensional semiconductor material is how conductive it is:

$$\sigma = e(n\mu_e + p\mu_h) \tag{2.1}$$

Here, σ is the electrical conductivity, n and p are the electron and hole charge density, respectively, and μ is the mobility for each type of carrier. This equation applies for semiconductors, where both electrons and holes are responsible for charge transport. Finally, e is the elementary charge.

Charge mobility describes how fast charge carriers move in a material in the presence of an electric field. A mobile charge, will accelerate in the presence of an electric field, until its accumulated energy is lost due to a scattering event. The average velocity of these carriers is also called drift velocity, denoted by v_d, and is related to mobility and the electric field:

$$v_d = \mu E \tag{2.2}$$

2.3.1 Graphene field-effect transistors

A field-effect transistor (FET) is a device that utilizes an electric field to change the conductance of its active channel. The three basic components of a FET are its source, drain and gate, as shown in the schematic of Figure 2.4. The active conducting channel in a transistor carries a current 'injected' at the source, which is then 'collected' at its drain. The gate is electrically isolated from the rest of the device, and is utilized to apply an electric field to the active component of the transistor, reducing the width of the conductive channel and thus the overall conductance of the device. Being able to turn a transistor on and off is one of the most basic pillars of current day electronics.

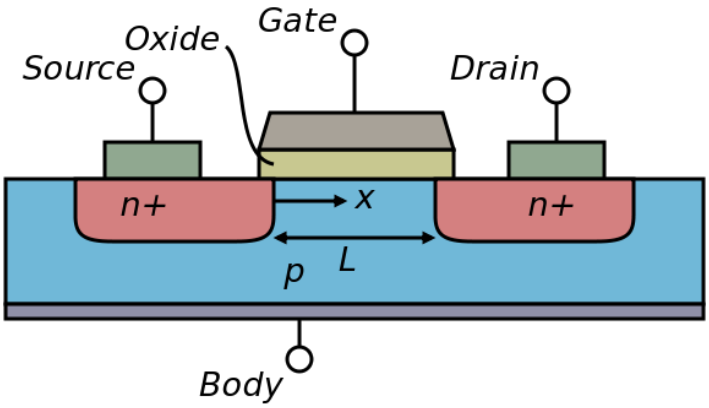

Figure 2.4 Schematic of a n-type field-effect transistor, where the body of the transistor is composed of a bulk semiconducting material [12].

The idea is similar if one uses graphene as the conductive channel. A graphene-based FET schematic is shown in Figure 2.5. However, graphene is a semi-metal, or a zero-gap semiconductor. Thus, in graphene FETs the field-effect is limited when varying graphene's carrier density. The band structure of graphene, which can be derived using tight-binding model calculations, is shown in Figure 2.6. The details of this calculation are summarized throughout the literature [3]. As it can be seen in Figure 2.6a, the conduction and valence bands in graphene touch at six points. These points are widely known as the Dirac points. Near a Dirac point, the band structure can be well described as being linear, yielding the conic structure shown in the insets in Figure 2.6b. One important implication from this symmetric dispersion relation, above and below E = 0, is that electrons and holes behave similarly (by applying a magnetic field one can still distinguish between the two types of carriers). A second implication, which physicists were really able to

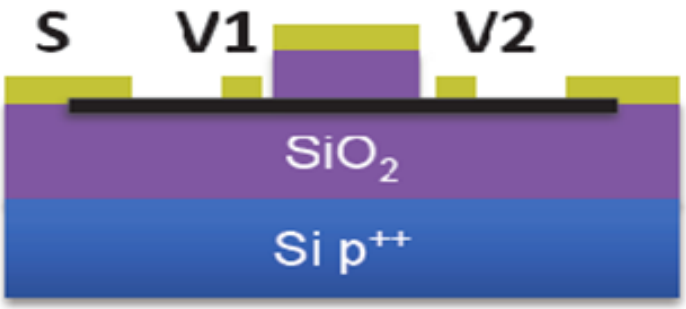

Figure 2.5 Schematic of graphene transistor, with a four-point probe geometry, with both a top and bottom gates able to tune the device conductivity.

appreciate, is that near the Dirac points graphene's dispersion relation can be described by the following expression: $E = \hbar v_F |\boldsymbol{k}|$, with charge carrier velocity, v_F, independent of energy. Such an expression usually characterizes the behavior of relativistic particles. Carriers in graphene, which behave as if they had no effective mass, are responsible for many of graphene's exotic electronic properties [4], such as an unconventional quantization for its quantum Hall effect [5] and Klein tunneling [6].

A vertical electric field can be applied to a graphene FET by controlling a gate bias. This will directly affect its charge density, and as shown in equation 2.1, vary the conductivity of graphene. Figure 2.6b is an example of the effect of a gate bias sweep on a graphene device's resistivity [7], the inverse of its conductivity. It should be noted that for an undoped graphene sheet, the charge density might be expected to drop to zero at $V_g = 0$, effectively leaving graphene as an insulator.

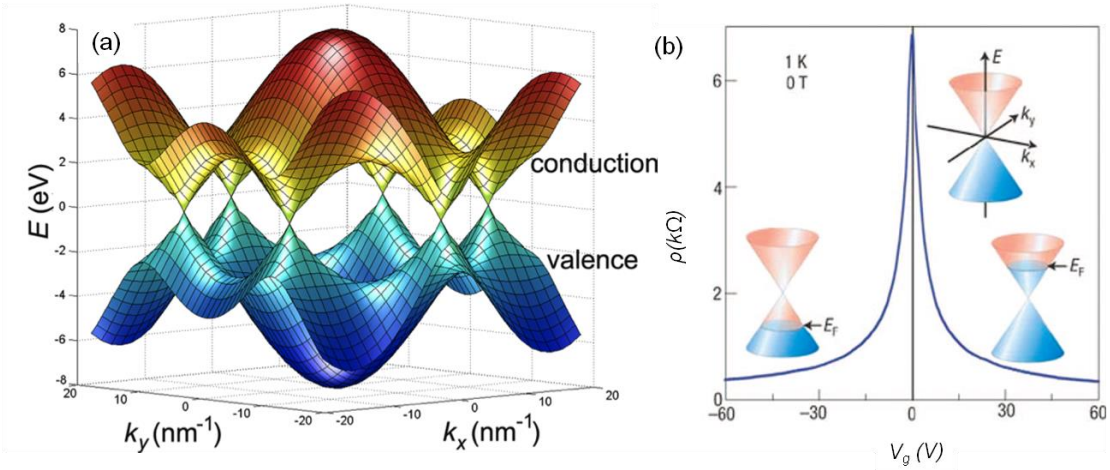

Figure 2.6 a) Band structure of graphene [13], and b) transport in graphene as a function of gate voltage, in a field-effect transistor geometry (from [7]).

However, long-range interactions and other effects impede graphene's resistivity from diverging at the Dirac point, instead saturating at ~6.5 kΩ per square. This value is the inverse of the conductivity quantum [7]:

$$G_{\blacksquare} = 4\frac{e^2}{h} \tag{2.3}$$

For non-zero gate bias, the conductivity increases. The slope of this change, as a function of gate voltage, is directly related to graphene's mobility. From the conductivity of a graphene device, as a function of gate bias, one can obtain a good estimate of charge carrier mobilities:

$$1/C_g \cdot (dg_{ds}/dV_{g\text{-}s}) \tag{2.4}$$

In this equation, C_g is the gate capacitance. When obtaining a graphene sample with new methods, or exploring different fabrication techniques, one widely used benchmark for determining the quality of a graphene sample is its charge carrier mobility.

2.3.2 Mobility as measure of sample quality

Mobility is limited by scattering events, which can be caused by defects and impurities or interaction with phonons. In graphene, because of its band structure, backscattering is largely suppressed, thus allowing extremely high mobility [8] even at room temperature (in the order or 10^4 $cm^2/V \cdot s$). In freely suspended devices, where the interaction with an underlying substrate is removed, charge mobility can exceed 10^5 $cm^2/V \cdot s$. As a comparison, silicon has a mobility of roughly 1400 $cm^2/V \cdot s$. Electrons move more than 100 times faster in graphene than in silicon.

A theoretical calculation can predict the electrical properties of a perfect graphene crystal, lying flat on a substrate free of defects. However, graphene

samples under experimental investigation can be far from perfect, often deposited on rough, amorphous silicon dioxide substrates, with abundant charge puddles near their surface. The graphene sample itself is often covered by relatively large amounts of residue (such a photoresist and leftovers from chemical etching processes). Nevertheless, these types of samples were still found to exhibit exotic behaviors predicted by many theoretical studies. The quality of the graphene crystals obtained by the simple exfoliation method was sufficient to observe many interesting effects.

2.4 Mechanical properties

In addition to its electrical properties, graphene's mechanical properties are also very impressive, due to its extremely strong carbon-carbon bonds. The same technique used to deposit graphene flakes on a supporting substrate can be used to obtain freely-suspended graphene membranes. By depositing graphene on a pre-patterned substrate, such as arrays of holes or trenches, the graphene will sit on top of the top surface, and hang over depressed features. Various groups utilized this approach, to produce graphene membranes, as shown in Figure 2.7 [9-11].

A suspended geometry allowed for the investigation of graphene's mechanical properties with unprecedented sensitivity, allowing for the first time a direct comparison of experimental results with theoretical predictions, rather than deducing them from extrapolation of the properties of other graphitic materials.

Graphene's in-plane elastic response is nonlinear, and its isotropic elastic behavior can be described by the following relation:

$$\sigma = E\varepsilon + D\varepsilon^2 \tag{2.3}$$

Here σ (not to be confused with the electrical conductivity of a material) represents stress and ε is uniaxial strain. *E* and *D* are Young's modulus and the third-order elastic modulus, respectively. Indentation force measurements performed with an AFM tip can be used to determine *E* and *D* [11]. Graphene's elastic response to the

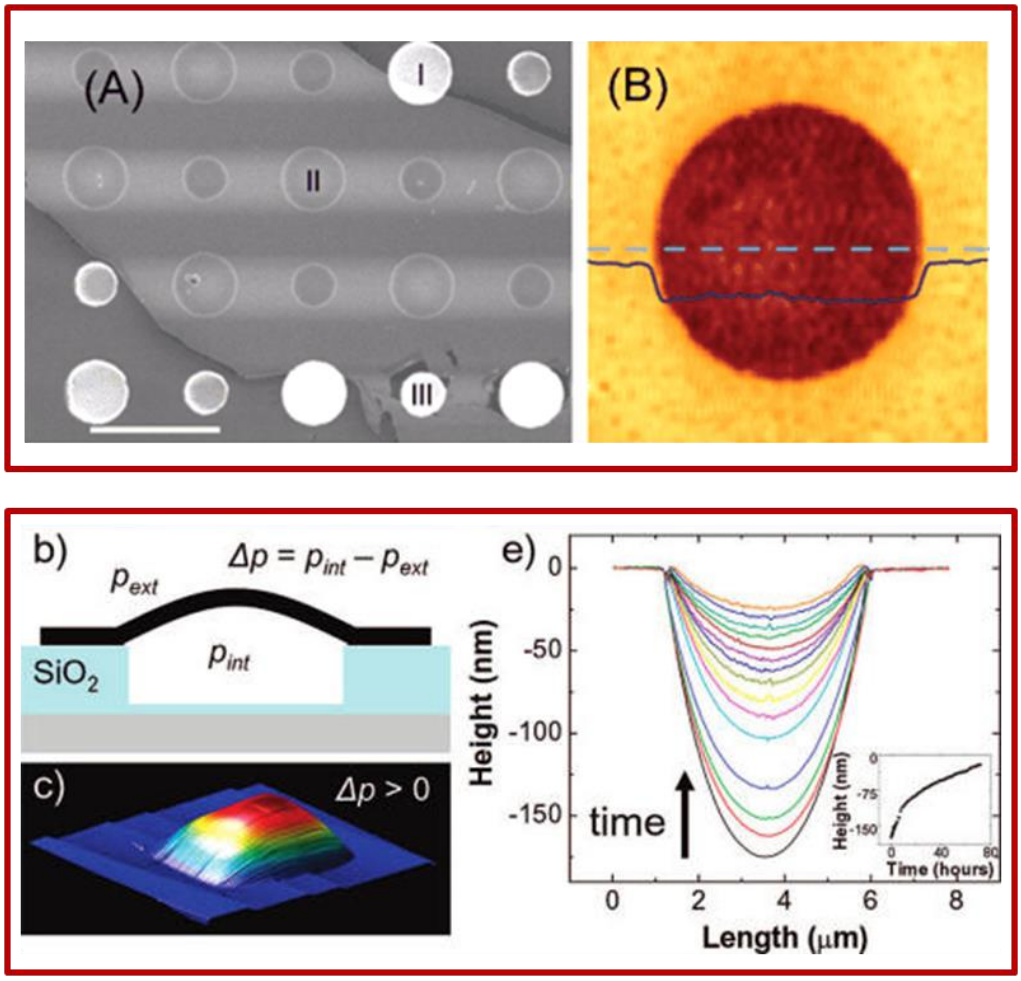

Figure 2.7 Examples of suspended graphene. Top: SEM and AFM images of suspended graphene over holes 1.0 and 1.5 microns in diameter [11].

Bottom: Schematic and AFM image of suspended graphene subject to a pressure difference [10].

tip's indentation is largely insensitive to the nonlinear component in equation 2.3, because only a small fraction of the graphene sheet stretches sufficiently. As shown in Figure 2.8, strain rapidly decreases away from the AFM tip. This allows for a simplification of the problem to a linear one, and the 2D Young's modulus was measured to be ~340 N/m, which corresponds to a bulk Young's modulus of 1.0 terapascals. In addition, by stretching graphene to its limit, the intrinsic breaking strength was found to be $\sigma_{int} \approx 130$ gigapascals, which is the largest bulk stress value ever measured. This further allows the value of *D* to be inferred [11], as $\sigma_{int} = -E^2/4D$. The nonlinear term in equation 2.3, *D*, was estimated to be -690 N/m (corresponding to a bulk value of -2.0 terapascals). This value is generally negative; at sufficiently large tensile strain a material will soften, and for sufficiently large compressive strains the material will increasingly stiffen.

For the measurements described, graphene's Poisson's ratio is needed. This number describes how much a material will contract, in the direction perpendicular

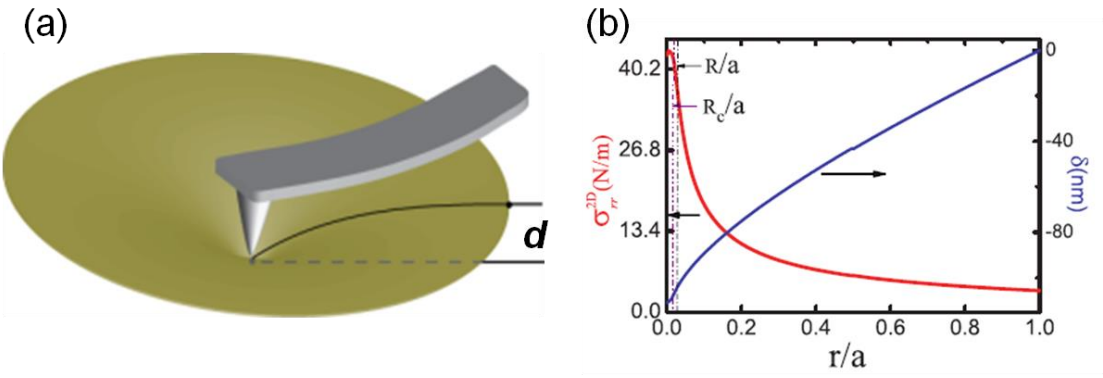

Figure 2.8 a) Schematic of AFM indentation on a circular membrane, and b) calculated 2D strain (σ^{2D}) and deflection (δ) for indentation on a graphene membrane, as a function of normalized position (r/a) (from [11]).

to an applied strain. In graphite this value is 0.17, and it accurately fits the models describing the observed graphene's elastic response.

The out-of-plane rigidity of a graphene membrane cannot be inferred from the properties previously listed. Bending in a 3-dimensional material causes stretching along its outer portion, while its inner portion contracts. Thus, parameters such as E and D are useful in describing the response of a material to a bending force. However, graphene is 2-dimensional. An ideal graphene sheet does not need to stretch to be able to bend, so its rigidity is a result of orbital overlaps; as it bends the direction of carbon-carbon bonds changes relative to the direction of neighboring bonds.

Theoretically, graphene's bending modulus has been estimated to be $B \approx 1$ eV. This is essentially the energy required to bend a material with area A, into a cylinder with radius of curvature in the order of $A^{1/2}$. However, an experimental determination of graphene's intrinsic bending rigidity is challenging. Since graphene can bend much more easily than it can stretch or compress, any deviation from uniaxial stress, which can arise from imperfect boundary conditions, will result in bending and rippling of the membrane. Thus, most bending rigidity measurements will be convoluted by the addition of extrinsic bending rigidity, arising from out of plane deformations.

2.5 Impermeability

It is perhaps not too surprising that a graphene membrane will also be able to withstand very large and even evenly distributed pressures without breaking. What is perhaps surprising is that atomically thin graphene membranes have been found to be

completely impermeable to even the smallest molecules [10]. As seen in the gas leak rates from graphene sealed enclosures, shown in Figure 2.9, leak rates are not related to the thickness of the graphene membrane. This means that gases leak through the glassy walls of the enclosures, or through the interface between graphene and the rest of the enclosure.

This remarkable property can be exploited to separate two very different environments. For example, if graphene is impermeable to gas molecules, one could expect graphene to be impermeable to liquids as well. One potential application which exploits this property will be discussed in Chapter 6.

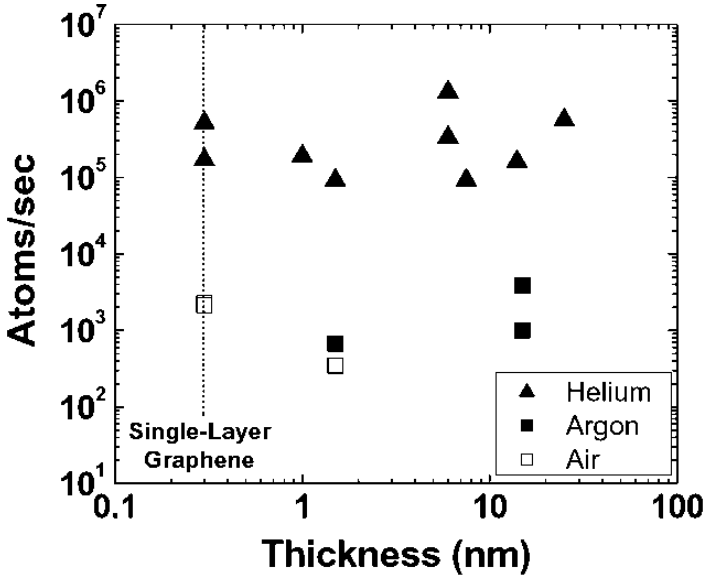

Figure 2.9 Gas leak rates for helium, argon and air as a function of graphene thickness (from [10]).

2.6 Towards CVD graphene

Having reviewed some of the most relevant properties intrinsic to graphene, we will turn our attention to CVD graphene. The task at hand is to determine if CVD graphene, which holds great advantages in terms of large scale batch production, is a viable method to produce graphene with the remarkable intrinsic properties of exfoliated graphene. As a new material, new fabrication methods must be adapted for its use. Some of these methods will be described in the following chapter.

REFERENCES

[1] K. S. Novoselov, *et al.* Proc. Natl. Acad. Sci. USA **102**, 10451 (2005).

[2] A. C. Ferrari, *et al.* Phys. Rev. Lett. **97**, 187401 (2006).

[3] J. C. Slonczewski, *et al.* Phys. Rev. **109**, 272 (1958).

[4] Y. Zhang, *et al.* Nature **438**, 201 (2005).

[5] V. M. Apalkov, *et al.* Phys. Rev. Lett. **97**, 126801 (2006).

[6] M. Katsnelson, *et al.* Nature Phys **2**, 620 (2006).

[7] K. S. Novoselov, *et al.* Nature **438**, 197 (2005).

[8] A. K. Geim, *et al.* Nat Mater **6**, 183 (2007).

[9] J. S. Bunch, *et al.* Science **315**, 490 (2007).

[10] J. S. Bunch, *et al.* Nano Letters **8**, 2458 (2008).

[11] C. Lee, *et al.* Science **321**, 385 (2008).

[12] Wikipedia Commons (accessed 2012).

[13] van der Zande, PhD Thesis, Cornell University (2011).

CHAPTER 3

CVD GRAPHENE:
SYNTHESIS AND FABRICATION

3.1 Introduction

This chapter is, in its majority, adapted from M.P. Levendorf*, C. S. Ruiz-Vargas*, S. Garg, and J. Park, ***Nano Letters*** 9 (2009).

Since the reports of isolation of thin graphitic films on an oxidized wafer [1] and the observation of the quantum Hall effect [2,3] single layer graphene (SLG) attracted intense research efforts both from academic and industrial communities. While the original exfoliation method led to many exciting discoveries in this unique crystal [4-8] the key question of large scale production of SLG remained a significant challenge. To fully utilize its exciting physical properties and integrate them into conventional electronic, mechanical, and optoelectronic circuitry, it is paramount to produce SLG with the physical properties similar to those of exfoliated graphene and with minimal spatial variation over extended areas.

Several studies were reported in 2009, describing the direct growth of graphene on thin nickel films [9,10], focusing on making these films as thin as possible with the goal of obtaining single layer. Soon after, it was shown that copper foil was an even better choice to obtain graphene films. Due in part to a very small solubility of carbon in copper, the deposition process was found to be largely self limiting [11] in obtaining SLG with promising electrical properties.

3.2 Transfer-free approach

Using CVD graphene materials for device applications often requires a transfer step, to electrically insulate graphene and because metal growth substrate is not compatible with device fabrication procedures. Graphene growth on insulating devices is possible, but so far has not been shown to be of comparable quality to growth on metal.

The extra transfer step can pose a number of challenges. First, the mechanically delicate SLGs can be damaged during the transfer. Second, the alignment between the graphene film and the target substrate presents additional technical challenges. Third, these transfer procedures are often performed in aqueous solutions and it is difficult to remove residues trapped between graphene and the target substrate. One possible approach to circumvent some of these challenges is to directly fabricate graphene devices on the growth substrate. While the basic mechanism is similar to the one reported by Li *et al.*[11] we used an evaporated copper film instead of a copper foil. This allows us to directly fabricate uniform transistor arrays without a transfer process. This technique is easily scalable to larger dimensions, limited only by the size of the substrate and growth chamber, and is compatible with conventional thin film technologies.

3.2.1 CVD on an evaporated copper film

We first discuss the synthesis of SLG. Our growth substrate is a copper film with a thin Ni adhesion layer, both directly evaporated onto a silicon wafer covered with a thermal oxide. Prior to evaporation of the Cu/Ni layer, wafers were rigorously

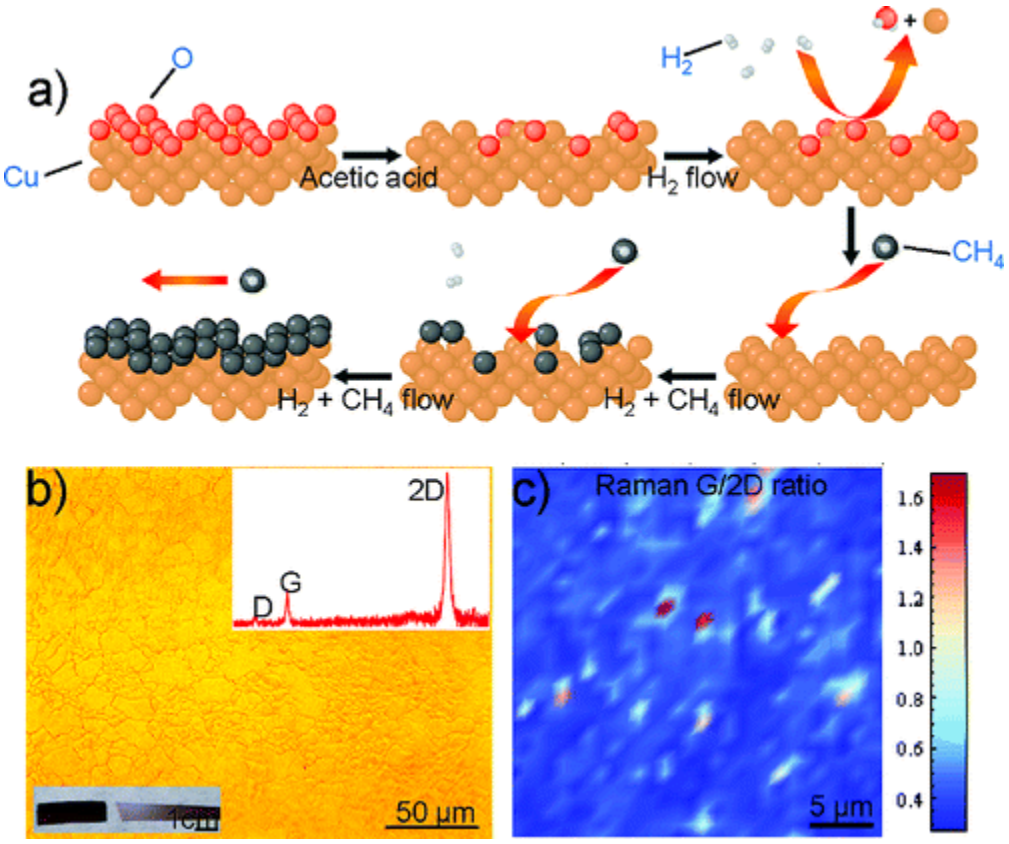

Figure 3.1 Method of graphene synthesis on evaporated copper. (a) Substrates are first immersed in acetic acid at 35 °C for 10 min and then quickly loaded into the reaction chamber. Samples are then exposed to 200 sccm H_2 at ~2 Torr while heating. Growths are carried out for 20 min at 1000 °C under 200 sccm H_2 and 875 sccm CH_4 at ~11 Torr. (b) Contrast enhanced optical image (100×,NA = 0.9) of a typical sample after synthesis of graphene. Copper oxide is present at grain boundaries if care is not taken to etch it before growth. Upper inset: representative Raman spectra of substrates after growth (Cu background subtracted). Lower inset: sample substrates before (left) and after (right) growth. After growth,the film appears to be a lighter in color and slightly speckled. (c) Two-dimensional map of G/2D ratio for as grown graphene which suggests at least 93% single layer graphene coverage.

cleaned in heated base and acid baths, following procedures equivalent to those for CMOS processing. Wafers pieces were immediately loaded into an e-beam evaporator for metal deposition. 5 nm of Ni were evaporated, followed by 495 nm of Cu without breaking vacuum.

Growths were carried out in a low pressure hot-walled chemical vapor deposition system. Before graphene growth, strips of the wafer are cleaved and then immersed in acetic acid at 35 °C for 10 min in order to remove most of the copper oxide. Even though the copper oxide would be removed prior to growth, this eliminates the need for a lengthy anneal which can deteriorate the quality of the copper film. The samples were then quickly loaded into the quartz reaction tube and pumped to a base pressure of 10 mTorr. A constant flow of H_2 (50-200 sccm) was then introduced into the chamber at a pressure of 2 Torr while the reaction tube was heated to the growth temperature of 1000 °C at a rate of ~ 40 °C/min. After reaching this temperature, 875 sccm of CH_4 was flowed for the growth step and the total pressure was maintained to 11 Torr. Standard growths lasted between 10 and 20 minutes, after which the system was slowly cooled at a rate of ~ 20 °C/min without altering the gas flow. After reaching 200 °C the system was then purged and pressurized with 1000 sccm of Ar. We found that one of the key variables is the thickness of the Cu film. While graphene grows continuously on Cu films thicker than 500 nm, poor film quality at high temperatures for thinner Cu films prohibits such growth. We thus used 500 nm thick Cu as our growth substrate. Ni was added as an adhesion layer for subsequent fabrication procedures, which does not affect the quality of the grown graphene as confirmed by Raman spectroscopy.

Figure 3.1b shows a contrast-enhanced brightfield image of a typical sample substrate after growth. Despite the presence of copper grains that are smaller than those found on Cu foils, we find that graphene is continuous across these visible Cu features as confirmed by Raman and electrical measurements. The inset to Figure 3.1b presents a Raman spectrum that is representative of the grown graphene. A single symmetric 2D peak (full width at half-maximum ~36 cm^{-1}), a small G/2D ratio, and a small D peak are observed, which strongly suggest that our graphene is a single layer and the quality of the sheet is not significantly affected by the visible features of the Cu film [12]. The growth of SLG was further investigated via spatially resolved Raman spectroscopy. The relative intensities of graphene's G and 2D bands are helpful to determine the number of graphene layers. Figure 3.1c shows a map of the Raman G/2D ratio that exhibits consistently small values (0.40 ± 0.06) except for a few localized spots. From this, we estimate the SLG coverage to be a minimum of 93%. The counts for the D peak were generally low and did not present any visible structures, which is consistent with high quality graphene synthesis. We note, however, that if care is not taken to strip the oxide beforehand, or if a slight leak into the reaction chamber is present, the quality of the SLG is reduced considerably.

3.2.2 Batch fabrication

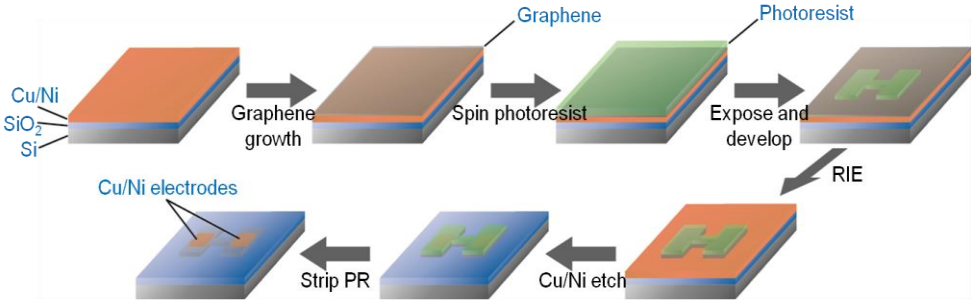

Figure 3.2 Schematic of device fabrication procedure.

Our SLG uniformly grown on a Cu-coated Si wafer substrate allows the fabrication of a large scale device array with a simple photolithography process. A schematic of our device fabrication method is shown in Figure 3.2. Our device design consists of two large pads connected by a thin strip, patterned using standard photolithography techniques. The photoresist covering the devices acts as a protective layer for the remaining processes. Sample substrates are subjected to a brief (30s) oxygen plasma etch to remove unwanted photoresist residue and graphene. Whole samples are then exposed to a continually refreshed etch solution long enough to remove the Cu/Ni in the unprotected areas and beneath the connecting photoresist/graphene strips. This results in two large pads of SLG/Cu/Ni connected by a narrow channel of SLG all protected by photoresist. Lastly, the photoresist is stripped in a solvent (acetone or N-Nethylpyrrolidone, for example) leaving the graphene channel resting on the substrate connected to the two pads. We find that the order of the last two steps is important. If the photoresist is instead removed first, extensive damage of the graphene sheet can occur.

3.2.3 Fabrication details

Our substrates with grown SLG were spin coated with photoresist. Standard photolithography defined a pattern in photoresist in the shape of the devices. A 30 second oxygen plasma (60 mTorr, 50 sccm O2, 150W RF power) was used to pattern SLG by etching away areas unprotected by photoresist. We then etched the unwanted Cu/Ni with a continuously refreshed dilute solution of $FeCl_3$:HCl:H_2O in order to slowly etch the excess Cu/Ni, while removing the etch products. The Cu/Ni etch was timed to allow for the etchant to undercut the photoresist and define the SLG channel, while leaving behind two appropriately sized SLG/Cu/Ni pads to be used for making electric contact with the device. Immediately following the etch, substrates were gently flushed with deionized water for several seconds. Samples were then carefully blown dry with N_2 before being placed into a vacuum chamber and heated to ~70 °C for 15 minutes. The photoresist layer was then vigorously stripped with acetone and a subsequent isopropyl alcohol rinsing.

For the fabrication of the top gates, a 100 nm thick layer of SiO_2 was evaporated directly onto the devices via e-beam evaporation. An additional step of standard photolithography was used, with a lift-off resist/photoresist bilayer. An adhesion layer of Cr (5 nm), followed by 45 nm of Au were then evaporated to define the top gate electrodes. Lift-off was carried out in an NMP based solvent. In order to facilitate uniform electrical contacts with the SLG/Cu/Ni electrode pads, windows in the evaporated SiO_2 layer were opened using standard photolithography followed by a wet oxide etch (30:1 buffered oxide etch).

3.2.4 Results

This fabrication process simultaneously produces a large array of devices. Figure 3.3a shows the optical image of the resulting array where each pair of pads forms a single SLG device. A zoomed-in image of one device is shown in Figure 3.3b that exhibits a clear undercut around the edges of the Cu/Ni as well as the intact SLG channel (more clearly visible in the inset). The differential interference contrast image of a long SLG channel is also provided in Figure 3.4. Here it confirms that the surface of the device channel is very clean without any visible residue underneath it, an important improvement over devices produced by a wet transfer process.

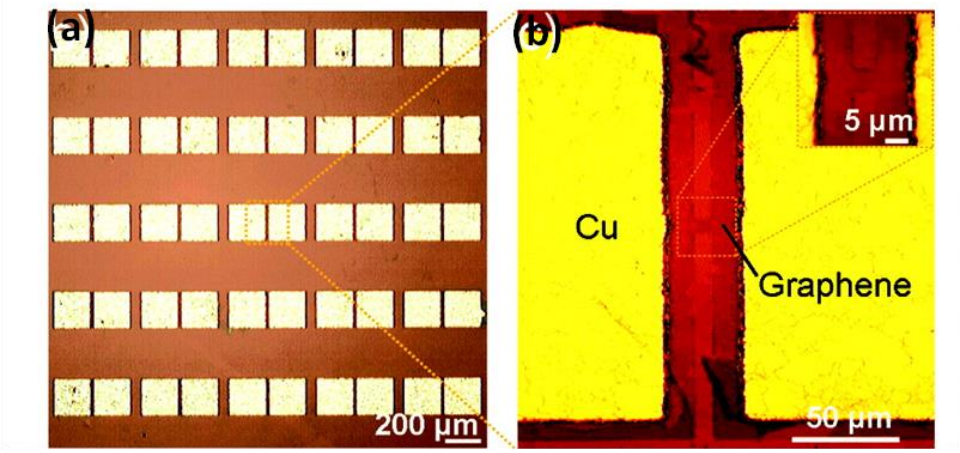

Figure 3.3 (a) Brightfield optical image of a typical sample substrate after fabrication. (b) Close-up brightfield image of the same sample. Graphene connecting the copper pad is just visible (boxed). Inset: Image of the device

3.2.5 Uniformity in electric performance

One key advantage of our fabrication process described above is its high yield and uniform electrical properties. In order to show this we fabricated 95 devices on a single substrate over a large area (~ 3−6 mm) with varying channel length and width (see Figure 3.5). A device schematic is shown in Figure 3.5a. Only 3 out of 95 devices are visibly broken (example shown in the inset of Figure 3.5c). All other devices were conductive, representing a 97% success rate. Two terminal resistance measurements Figure 3.5a showed that nearly 80% of conducting devices have resistances of less than 10 kΩ, as can be seen from the cumulative probability plot for device resistance (Figure 3.5c). In addition, we observe that median device resistance (R_{median}) increases with increasing channel length and decreasing channel

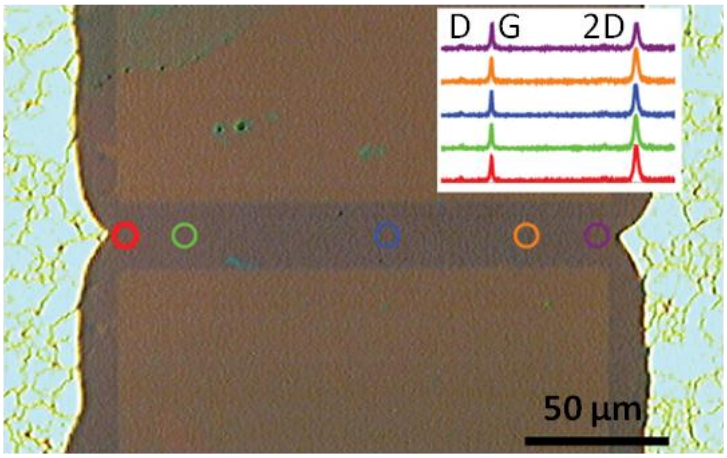

Figure 3.4 Differential interference contrast image of a longer device.
Upper inset: Raman spectra across the length of the graphene strip are highly uniform.

width (Figure 3.5d,e). From these we estimate the sheet resistivity of our SLG to be 25 kΩ with total contact resistance on the order of 3 kΩ (denoted by an arrow in Figure 3.5d). Remarkably, we find that our process allows the fabrication of devices with much longer SLG channels (as long as 0.5 mm). One device with a 0.33 mm long channel (fabricated from a different batch) is shown in Figure 3.5f, which has an exceptionally low two terminal resistance of ~27 kΩ (Fig. 3.5g). The uniform Raman features shown in Figure 3.4 and the high yield of conductive devices discussed above is consistent with continuous growth of SLG over a large area. We also note that the dimensions of the devices exceed the typical feature size in Figure 3.1b. Therefore our SLG allows fabrication of more complicated devices with uniform performance characteristics over a large area, a key step toward integrating graphene into existing technology. One such example is provided in Figure 3.6, where we show an array of field effect transistors fabricated with our SLG. Each transistor has an individually addressable top gate electrode made with Cr(5 nm)/Au(45 nm) defined on top of 100 nm thick film of SiO_2 gate oxide (evaporated directly onto SLG). A close-up image of the SLG channel with the top gate (TG) is shown in Figure 3.6a with a schematic cross section of the device. In Figure 3.6c, the low bias conductance, g_{DS}, as a function of the top gate bias (V_{TG-S}) measured from one of our devices is shown. The minimum conductance was observed near V_{TG-S} = 0.5 V, which corresponds to the Fermi level being at the Dirac point of the SLG. The electron mobility was estimated to be approximately 700 $cm^2/V \cdot s$ using $1/C_{TG} \cdot (dg_{DS}/dV_{TG-S})$, where C_{TG} is the top gate capacitance. The true value can be larger considering the fact that the true top gate capacitance tends to be smaller than

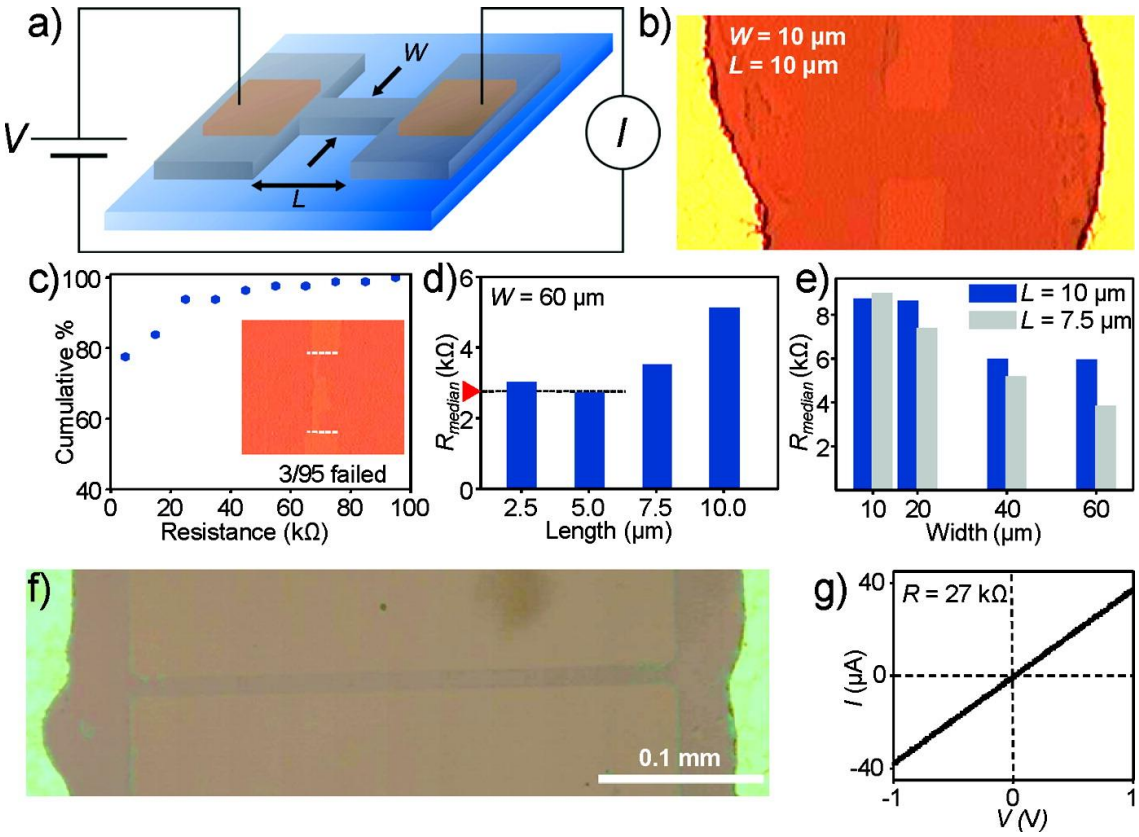

Figure 3.5 Electrical characteristics of SLG devices. (a) Schematic of device with patterned Cu/Ni electrodes contacting graphene from below. (b) Optical microscope image, taken with a 50× objective, of a SLG graphene device (width (W) = 10 μm, length (L) = 10 μm). (c) Cumulative probability plot of device resistance. Ninety-seven percent of the devices were found to be conductive, and 80% were found to have resistance less than 10 kΩ. Inset: broken device, likely damaged during photoresist stripping. (d) Median resistance (R_{median}) for those devices with R_{median} < 10 kΩ, as a function of length (W = 60 μm) (e) and as a function of width for L = 10 μm (blue) and 7.5 μm (gray). (f) Optical image, taken with a 20× objective, of a ~0.33 mm long SLG device and ~10 μm in width. (g) Even though length of this graphene strip is at least an order of magnitude greater than the typical grain size in the evaporated copper film, this device exhibits high conductance with R = 27 kΩ.

the ideal value of 34.5 nF/cm^2 for 100 nm SiO_2 used in our estimate. Unlike in our topgated devices, we observe that the device conductance show much weaker backgate dependence.

While this mobility value is significantly smaller than the one reported by Li *et al.*, [11] it is smaller by only a factor of 2 in comparison to the mobility reported for exfoliated graphene used in a similar device geometry by Meric *et al.* [13] The latter study also showed current saturation and a large transconductance, a key characteristic for many RF and high power device applications. Surprisingly, we observe similar current saturation from many of our devices at relatively low V_{DS}.

Data from the same device in Figure 4c is shown in Figure 4d. As we decrease $V_{TG\text{-}S}$, regions of current saturation become more prominent with a transconductance of at least 8 μS per 1 μm of channel width. Use of a thinner (20 nm) and more efficient gate oxide, such as HfO_2, can thus increase the transconductance by a factor of 20. Considering this, the transconductance from our device could be comparable to the best value reported by Meric *et al.*

We again note that the SLG synthesis and device fabrication method discussed here is compatible with standard thin film technologies and does not involve any nonconventional and delicate steps such as liquid based transfer. Thus, it can allow SLG to be integrated into large scale electronics circuitry with only minor steps that can easily be streamlined and automated. In addition, as anticipated, additional synthesis optimization and materials characterization will further improve already promising electrical and physical characteristics of large scale SLG.

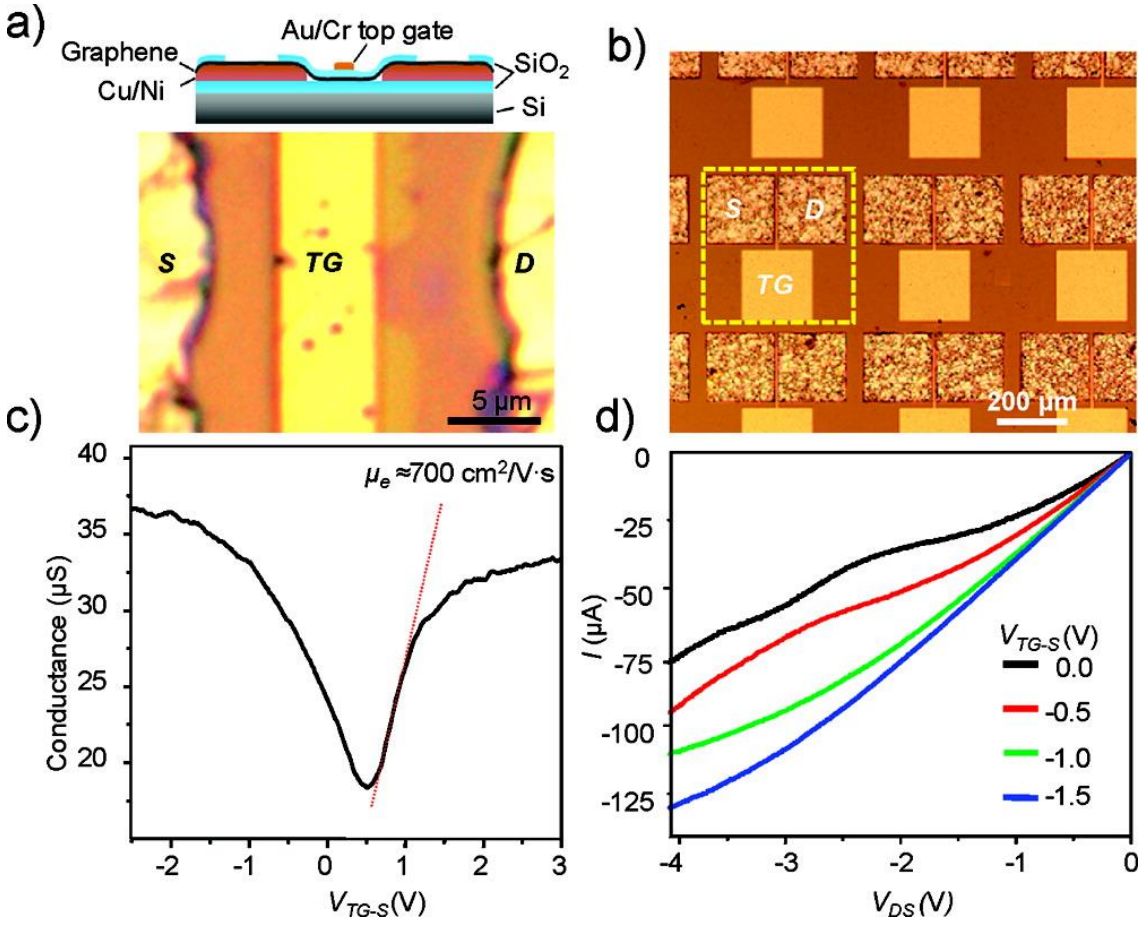

Figure 3.6 Gate dependence of SLG transistors. (a) Top: cross view schematic of top gated SLG transistor. Bottom: optical image of the top gated (*TG*) graphene channel, taken with a 50× objective. (b) Large area view of a region arrayed with SLG transistors in a top gate geometry. (c) Gate dependence for representative device with an electron mobility (μ_e) of ~700 $cm^2/V \cdot s$ for V_{DS} = 100 mV. (d) Saturation current observed for negative DS bias (V_{DS}), and a transconductance of ~8 μS/μm.

3.3 Free-standing CVD graphene membranes

Establishing protocols for transfer-free fabrication of graphene based devices has many advantages. However, for the fabrication of suspended graphene samples, it is often desirable to follow transfer protocols. While a few fabrication methods to obtain transfer-free suspended CVD graphene have been reported [14], they are in general limited by the necessity to control the removal of a specific portion of the underlying metal substrate. This is difficult to control. One failed attempt is shown, as an example, in Figure 3.7. Here, the underlying copper film has been uncontrollably etched. One of the main reasons for these difficulties is that graphene growth on copper is performed at temperatures very close to its melting point, so the thickness of the copper film (or foil) has to be sufficiently large to prevent migration and agglomeration during growth. Then, if the copper layer needs to be thick, this limits the feature size achievable through normal chemical etching processes to remove it, as these etching processes are isotropic.

In this section, we describe the preferred approach, used throughout this thesis, to obtain graphene membranes with high yields. One key innovation developed for this work is the dry release of the graphene membranes, in the last step of fabrication, as described below.

3.3.1 Fabrication details

Single-layer CVD graphene is grown using a similar process as in the previous section, utilizing copper foil (Alfa Aesar #13382) as the growth substrate

instead of the evaporated copper film. Growth was done at 1000° C for 10 minutes in low pressure (~10 torr), with a flow of CH_4:H_2 (875:300 scmm). We again confirmed with Raman spectroscopy that the resulting films were predominantly single layer graphene (SLG).

CVD graphene films are transferred onto the target substrate in order to form suspended membranes. The transfer is done by spinning a thin PMMA layer onto the copper foil (~50 nm) and etching the metal away with a ferric chloride aqueous solution, similarly to Li *et al.* [11] The resulting membrane is scooped into a series of rinsing water baths and finally transferred to the target substrate.

We utilized a very thin protective polymer layer (PMMA) for the transfer, followed by a liquid-free removal of the polymer, as described below, which results in higher yields than previously reported. The graphene sheets adhere well to the supporting surface, which is important for the nanoindentation measurements described later. Our target substrates were usually pre-patterned nitride grids. These

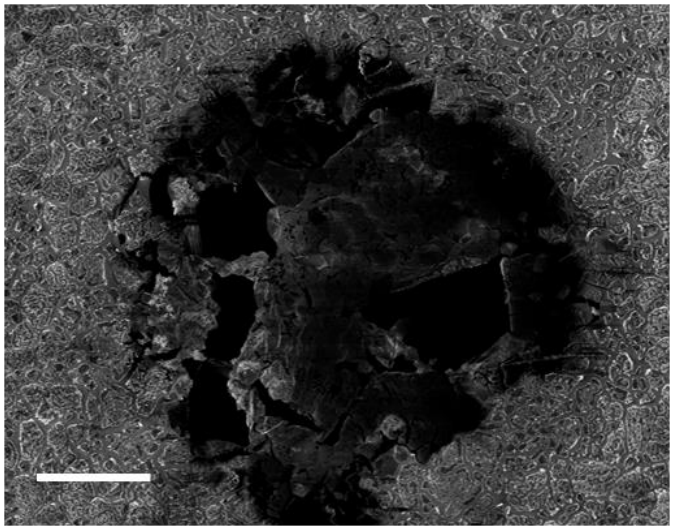

Figure 3.7 SEM image of partially suspended graphene/copper fragments. Scale bar: 20 microns.

were fabricated on Si wafers coated with LPCVD low-stress silicon nitride using standard photolithography and reactive ion etching, followed by an anisotropic KOH etch to expose the silicon nitride layer from the backside. The resulting structures are shown in Fig. 3.8.

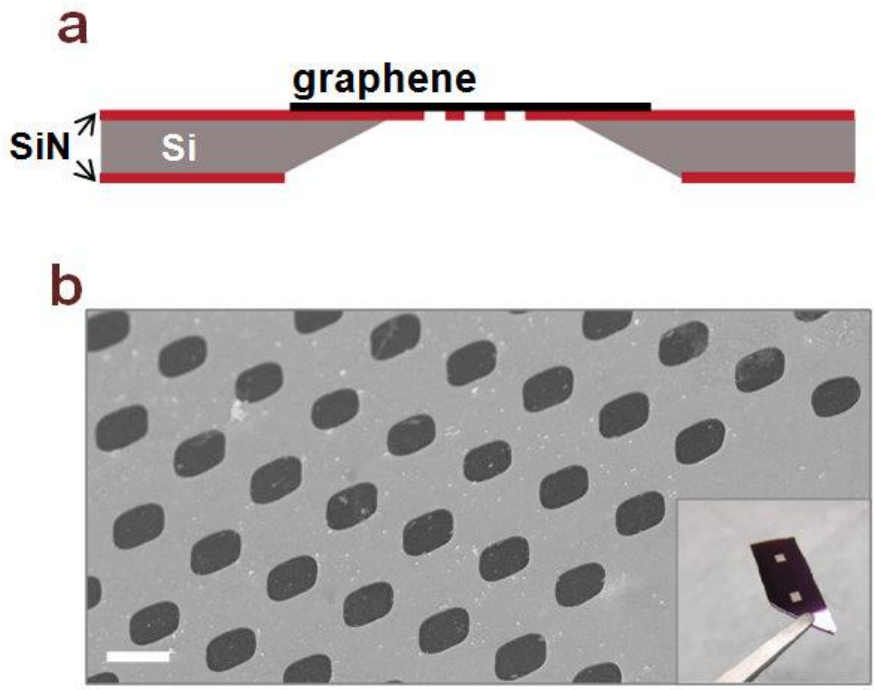

Figure 3.8 a) Schematic of substrate with arrays of suspended graphene and b) SEM image of high yield array of suspended graphene regions. Scale bar: 2 μm. (inset: optical image of a chip with two holey silicon nitride membranes visible).

We found that using very thin protective PMMA layers (< 100nm) is important, since it promotes conformal adhesion of graphene to receiving substrate. Thicker PMMA layers impede this by stiffening the PMMA/graphene film, resulting in extensive tearing in the graphene membranes when the polymer is removed. Once the sample is dry, the samples are baked for 3-4 hours at 300-350°C. PMMA decomposes at these temperatures [15] allowing for a gentler dry release of the graphene membrane from its protective polymer support. We found that baking our samples directly in air resulted in fast PMMA removal. However, it is also possible to do this more slowly under Ar/H_2 flow, which is gentler for the graphene membranes. This fabrication method produces suspended graphene membranes with a high yield exceeding 90% for grids containing more than 10,000 2 μm holes. We were also able to fabricate suspended graphene sheets as large as 30 μm, which were the largest dimensions we attempted to fabricate.

3.4 Summary

In this chapter we have described two different fabrication techniques: a transfer-free method, which is specific for the fabrication of graphene ribbons in electrically addressable devices, and a transfer method to obtain free-standing graphene membranes. In the following two chapters we will explore some of the properties found in free-standing sample obtained with the second method.

REFERENCES

[1] K. S. Novoselov, *et al.* Science **306**, 666 (2004).

[2] Y. Zhang, *et al.* Nature **438**, 201 (2005).

[3] K. S. Novoselov, *et al.* Nature **438**, 197 (2005).

[4] K. S. Novoselev, *et al.* Science **315** (2007).

[5] K. I. Bolotin, Solid State Commun. **146**, 351 (2008).

[6] J. S. Bunch, *et al.* Science **315**, 490 (2007).

[7] C. Lee, *et al.* Science **321**, 385 (2008).

[8] R. R. Nair, *et al.* Science **320**, 1308 (2008).

[9] A. Reina, *et al.* Nano Letters **9**, 30 (2009).

[10] K. S. Kim, *et al.* Nature **457**, 706 (2009).

[11] X. Li, *et al.* Science **324**, 1312 (2009).

[12] A. C. Ferrari, *et al.* Phys. Rev. Lett. **97**, 187401 (2006).

[13] I. Meric, *et al.* Nat. Nanotechnol. **3**, 654 (2008).

[14] B. Aleman, *et al.* ACS Nano **4**, 4762 (2010).

[15] L. Jiao, *et al.* J. Am. Chem. Soc. **130**, 12612 (2008).

CHAPTER 4

MORPHOLOGY AND MECHANICAL PROPERTIES OF CVD GRAPHENE MEMBRANES

4.1 Overview

This chapter is adapted from C. S. Ruiz-Vargas, H. Zhuang, S. Garg, P. Y. Huang, A. M. van der Zande, P. L. McEuen, D. A. Muller, R. Hennig, and J. Park, ***Nano Letters*** 11 (2011).

The excellent mechanical properties of pristine graphene, such as an extremely high in-plane stiffness (Young's modulus) and high breaking strength[1], along with its unusual electronic properties, make graphene an excellent material for use in applications such as flexible electronics [2] and nanomechanical systems [3,4].

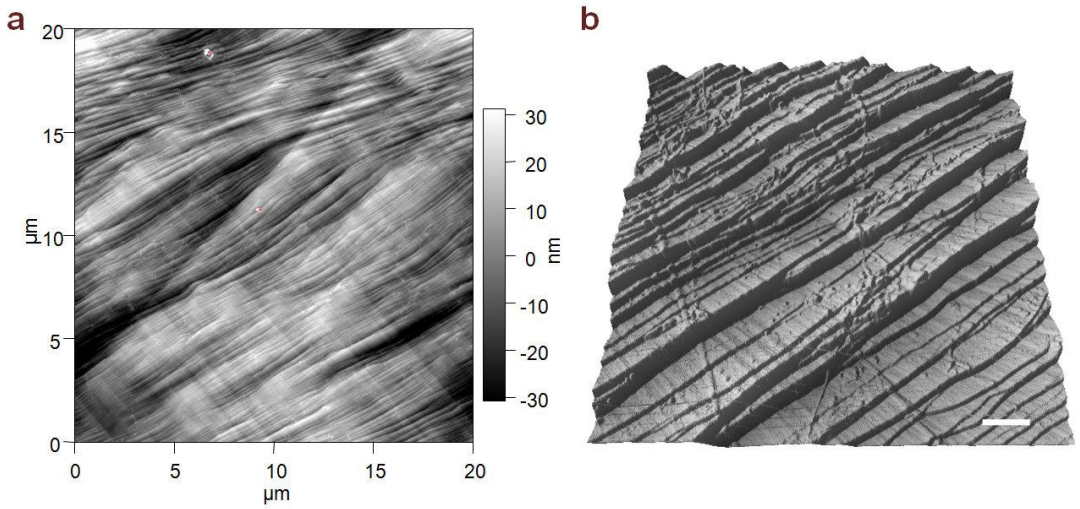

Figure 4.1 AFM height images of a copper substrate after graphene growth. a) Region 20 microns in size b) 3D image from a zoomed in region. Scale bar: 500 nm.

Recent advances using chemical vapor deposition (CVD) have paved the way for the production of single layer graphene on technologically relevant scales. Large-area graphene can be grown on metal surfaces and transferred to a variety of substrates [5-10]. Most notably, graphene growth on copper can be limited to a single layer [8], enabling novel methods for batch fabrication of graphene devices [11-13]. CVD graphene should be an ideal material for mechanical device applications because in theory, it combines practicality with the excellent mechanical properties of exfoliated graphene.

However, as the AFM image in Figure 4.1 shows, the surface of copper after graphene growth is far from flat. Thus, an important question is what will happen when one releases a 2-dimensional crystal from a 3-dimensional growth substrate. Could it truly be flat? Furthermore, strains induced during growth and transfer processes can cause out-of-plane rippling in free-standing membranes. The understanding of these effects on the mechanical properties of CVD graphene is still limited and is critical to achieving the full potential of graphene in mechanical applications. Here, we use atomic force microscopy (AFM) and nanoindentation measurements and molecular dynamic simulations to study the effect of these unique features on the mechanical properties of CVD graphene.

4.2 AFM imaging

First, we characterize the topography and structure of the CVD graphene membranes using AFM. We used a MFP3D scope from Asylum Research, and used silicon AFM probes (Multi75Al, Budget Sensors) with a resonant frequency of

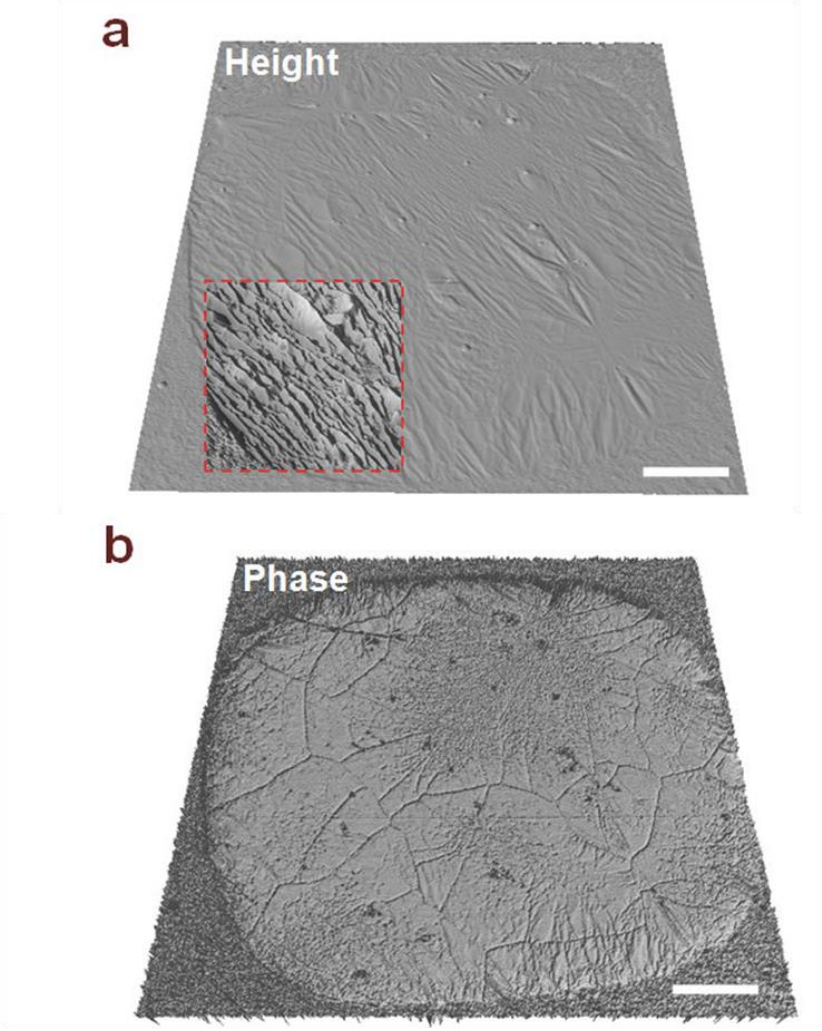

Figure 4.2 a) AFM height and b) phase tapping mode images of a suspended graphene membrane, with grain boundaries clearly visible in the phase image. A region in the image in a) is shown enlarged in the z direction (height) to accentuate the rippling in graphene. Scale bar: 500 nm.

~75 kHz, a force constant of ~3 N m^{-1} and a tip radius of <10 nm. All imaging was done in tapping mode. Images were taken at resolutions of 512 × 512 or 1,024 × 1,024, with acquisition times of at most 10 min.

Fig. 4.2a shows the topography of one suspended membrane, which is clamped on all sides. The membrane appears taut at its edges, without the presence of slack or major corrugations. Detailed imaging, however, reveals that the membranes are rippled on the nanometer scale (Fig. 4.2a, inset). The surface roughness of these sheets is ~3nm (rms), with ripples measuring a few nanometers in amplitude, as shown by the height profile along the dashed line in Figure 4.3

It is likely that the observed ripples in our membranes are the result of a combination of factors inherent in the growth and transfer process. CVD graphene is not flat to begin with, as it is grown on a copper substrate with surface roughness

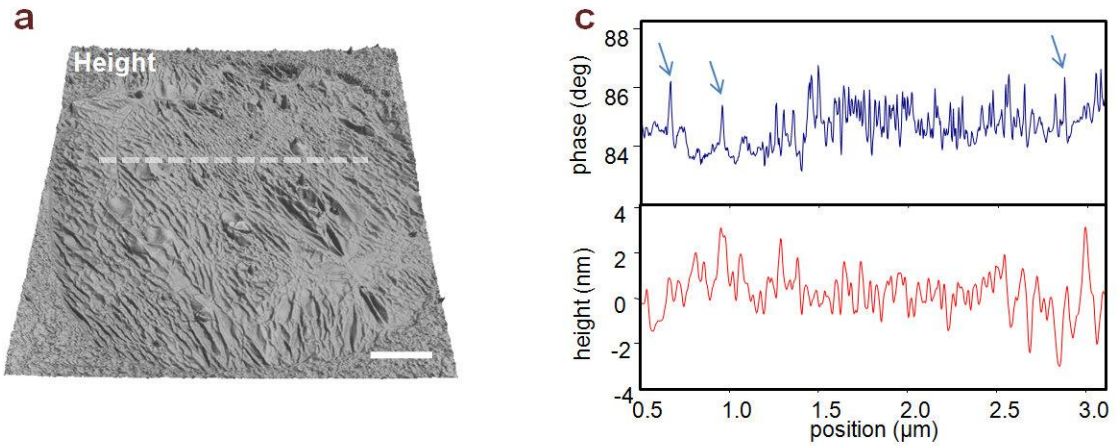

Figure 4.3 a) AFM height image as shown in the main manuscript. b) Phase and height traces taken along the dashed line in a, the locations of visible grain boundaries are denoted in the phase trace by the arrows.

comparable to that of the graphene membranes (Figure 4.1) [14]. This inherent non-flat topography could then in turn lead to rippling once the membrane is transferred and subjected to the constraints imposed by the edges of the holes in the supporting substrate. Non-uniform adhesion of membrane to the edges of the holes [15] could cause anisotropic pretension and the irregular transfer process could cause shear strain, all of which may result in wrinkling in the membrane. For instance, a shear strain as small as 0.5% would result in ripples with a ratio of amplitude to wavelength comparable to the one we have observed in our membranes [16,17]. Furthermore, thermal cycling has been shown to cause corrugations in graphene and graphene oxide membranes [16,18]. We expect that some inward slipping due to graphene's negative thermal expansion coefficient will further affect the final topography of our membranes without bringing them to a fully relaxed state. Finally, the presence of grain boundaries and defects are predicted to induce topography changes in fully suspended graphene, although perhaps to a lesser extent [19,20]. Further experiments would be required to determine the exact origin of the final topography of our membranes, but such experiments would be difficult with the current membrane fabrication techniques. However, the presence of wrinkles and their effect on the membrane mechanics, described below, highlight some of the general challenges that will be encountered when designing and fabricating devices with free-standing single layer graphene, including the large array mechanical resonators recently reported [13].

Fig. 4.2b shows a phase image of the same region as Fig. 4.2a. Strikingly, phase imaging reveals thin lines in the suspended membranes (marked by the arrows

in the line profile in Figure 4.3b), which are barely visible in height images. By direct correlation with STEM imaging (Figure 4.4), we identify these features as graphene grain boundaries. We will expand on the polycrystalline CVD graphene structure in the next chapter, but for now we will focus on our observations during AFM imaging.

STEM and electron energy loss spectroscopy (EELS) characterization of these membranes have identified iron oxide nanoparticles (originating from the $FeCl_3$ Cu etchant) and amorphous carbon adsorbed at the grain boundaries [21]. These surface adsorbates are likely responsible for the contrast in phase images. These imaging details allow for spatially resolved nanoindentation measurements with respect to the location of the graphene grain boundaries.

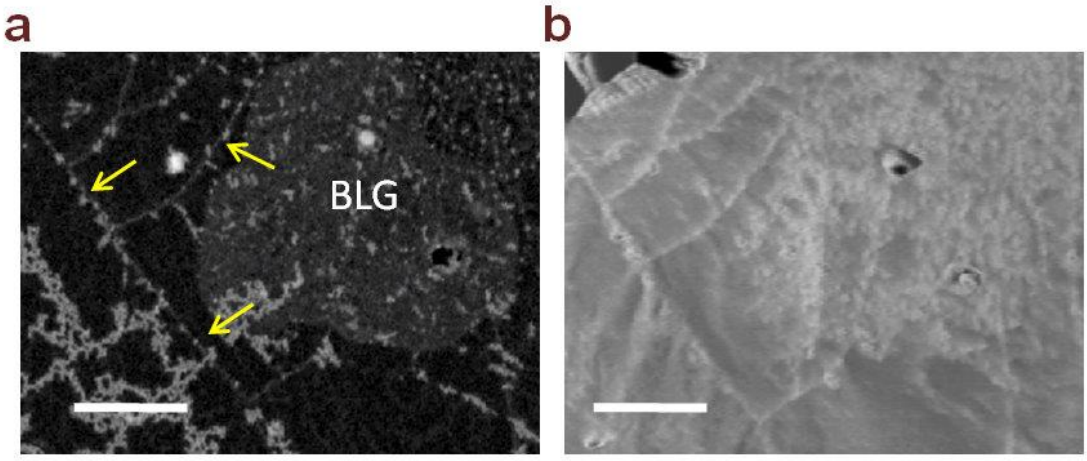

Figure 4.4 a) STEM image of graphene, and bilayer graphene as marked in the image. The arrows show the location of grain boundaries as confirmed by the diffraction pattern obtained across these features. b) AFM phase image of the same region, with the grain boundaries visible. The bilayer graphene region is also discernable. Scale bars: 200 nm.

4.3 Indentation measurements

We performed a series of nanoindentation measurements to measure the mechanical properties of graphene membranes. We were able to identify graphene's grain boundaries in the phase mode, as shown in the previous section. Based on this mapping of grain boundaries, indentation points were selected, and force curves were obtained there. The force-deflection curves are obtained by pushing the AFM tip down onto the graphene membrane. From the measured vertical position of the AFM cantilever and the tip deflection one obtains the distance that the graphene membrane deflects under a given force. Following a model similar to the one described by Lee *et al.*[1], we have calculated values of 2D elastic Young's modulus for our

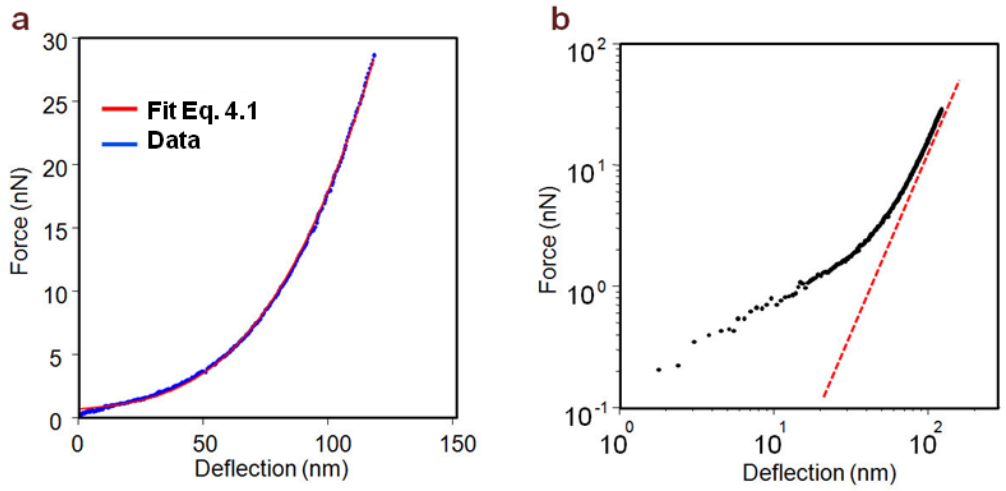

Figure 4.5 a) Force curve showing both the data and the model used to calculate the 2D elastic modulus, a good fit can be seen. b) Same data plotted on a log-log scale, shown approaching cubic behavior (dashed line).

membranes as well as existing pretension, by fitting our data to the following expression:

$$F = 2\pi\sigma d/\ln\frac{a}{r} + E\,(qd)^3/a^2 \qquad (4.1)$$

In equation 4.1, σ and E are the 2D pretension and 2D effective Young's modulus, respectively. The parameters, d, a, and r, are the vertical deflection, the membrane's radius and the radius of the AFM tip, respectively [15,22]. Finally, q (which is roughly 1.02) [1] is a function of the Poisson's ratio. We note that the shape of our membranes is square with rounded corners, and we assume our membranes to be circular, with a radius of 1.75 μm resulting in an uncertainty in our calculation of ~ 5%. This model provides a close fit to our data, as seen in Figure 4.5. The data approaches cubic behavior (dashed line, Fig. 4.5b) for large deflections, the regime from which the effective 2D elastic modulus is calculated. Our model differs slightly from the one described by Lee. *et al.*[1] by taking the size of the indenter into account in the linear term of the equation. This is a geometric consideration [15,22]. From similar measurements taken on 60 membranes, we find an average effective 2D elastic modulus of 55 N/m with a large FWHM distribution of ~50 N/m (Fig. 4.6). Our average value is a factor of ~6 smaller than the intrinsic elastic modulus of graphene [1]. We also find an average pretension of 0.085 N/m, in good agreement with the mechanical resonance frequencies found in similarly fabricated devices [13]. As shown in Fig. 4.6a, reproducible curves are obtained when performing repeated measurements on the same spot. Complete membrane failure is observed in the last force curve in Fig. 4.6a, where a weakened mechanical response is followed by a sudden drop in the force exerted by the tip.

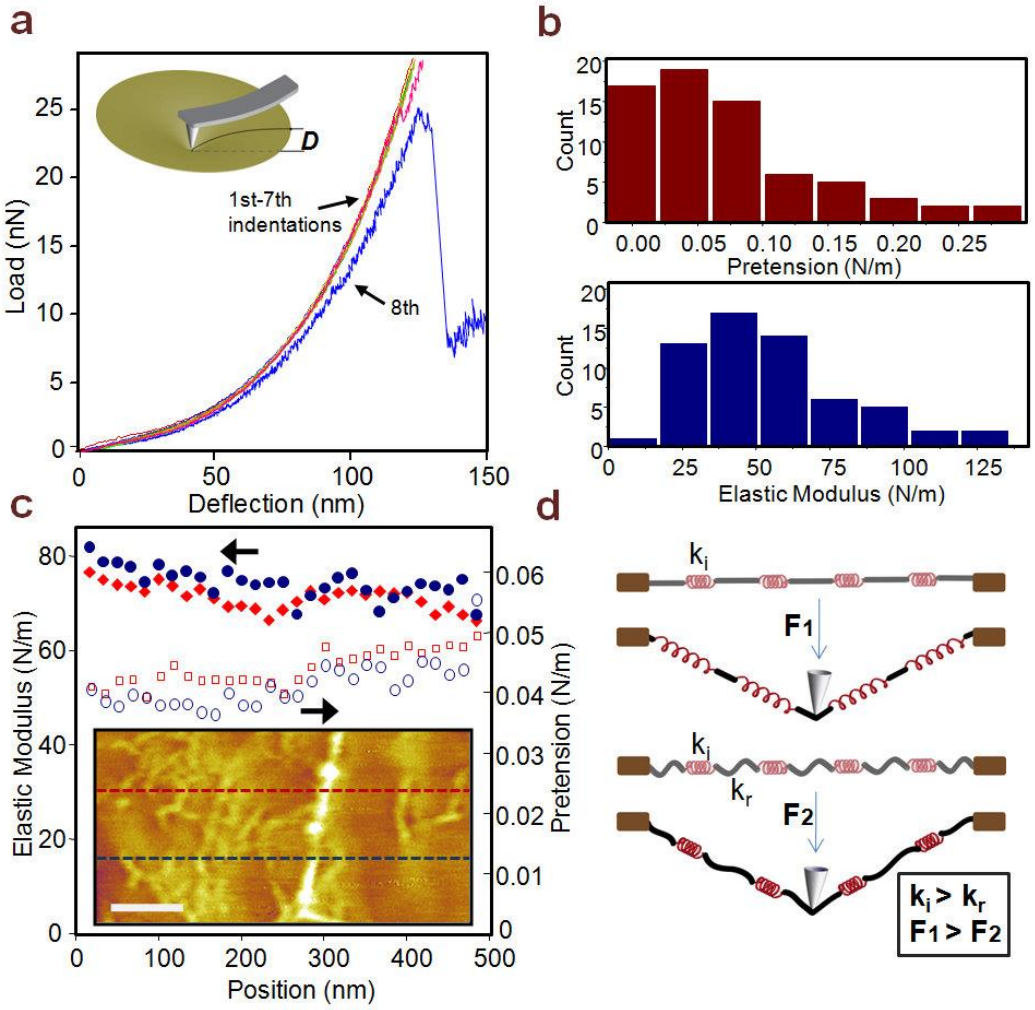

Figure 4.6 a) Consecutive indentation measurements taken at the same location of a graphene membrane with side length ~3.5μm are shown. Inset: schematic of the nanoindentation measurements. b) Histograms of 2D pretension and 2D effective elastic modulus calculated from similar force curves measured from 60 devices of the same dimensions. c) Plots of 2D pretension and effective elastic modulus vs position measured from a graphene sheet. They stay nearly constant, even across grain boundaries. Data points were taken along the dashed line in the AFM phase image shown. Scale bar: 100nm. d) Model illustrating a flat and a rippled graphene cross section. The springs have a spring constant k_i representing graphene's intrinsic elastic modulus. However, flattening ripples, which have a much smaller spring constant k_r, requires less energy than stretching the membrane.

Our measurements were reproducible at the same location, and they also remain approximately constant over a large area. As shown in Fig. 4.6c, the 2D pretension and the effective elastic modulus do not vary significantly when crossing a grain boundary and many graphene ripples. Thus, grain boundaries and ripples do not locally affect the elastic response of the graphene membranes within the limits of our measurements.

We believe that the ripples play a role in the softening of CVD graphene membranes, as previously suggested [23]. To illustrate this, we consider a rippled membrane with negligible bending rigidity. Such a membrane would appear to stretch when subject to an indentation measurement, as its ripples in a given direction flatten out (Fig. 4.6d). In graphene, the bending energy can be neglected for the case of the typical ripples observed on our samples [24]; the force required to flatten out its ripples is considerably less than the force needed to cause in-plan stretching of this membrane. We can approximate a typical height profile across a rippled graphene membrane 3.5 μm in diameter by a sinusoidal function $A\sin(2\pi x/\lambda)$, with amplitude A of ~2nm and wavelength λ of ~70nm. If subject to vertical indentation, ripples along this direction would only completely flatten out for vertical deflections $d > 200$ nm, which is comparable to the maximum deflections we reached in our measurements. Thus, we expect ripple flattening to occur throughout the indentation cycle. The finite effective spring constant of these ripples, and consequently the overall mechanical response of these membranes, will be determined not only by their intrinsic bending modulus but also by the ripples structure and boundary conditions under a given stress field.

4.4 CVD Graphene Unzipping

To better understand the effect of grain boundaries on graphene's breaking strength, we perform spatially resolved nanoindentation measurements, where the vertical load attained before membrane failure is recorded as a function of tip position. Figure 4.7a shows a histogram of the breaking loads of 29 graphene membranes, directly on top of grain boundaries and at average distances 300 nm away from a boundary. The average breaking loads, on and away from a grain boundary, are ~50 nN and ~120 nN respectively. Figure 4.7b shows images of a region in a graphene membrane with a grain boundary before and after indentation. The weakening effect of grain boundaries can be directly visualized in these AFM images, where tears in the membrane can be seen to follow the direction and path of a grain boundary [21]. Once tearing in a membrane starts, a process analogous to unzipping can occur if this tearing happens at a grain boundary.

From indentation measurements performed at grain boundaries, we estimate the upper bound for the in-plane breaking stress to be ~35 GPa, on the majority of membranes. For this estimate we assume that membrane failure starts directly under the indenter and we use the expression:

$$\sigma_{max} = \sqrt{\frac{FE_{int}}{4\pi r}} \tag{4.2}$$

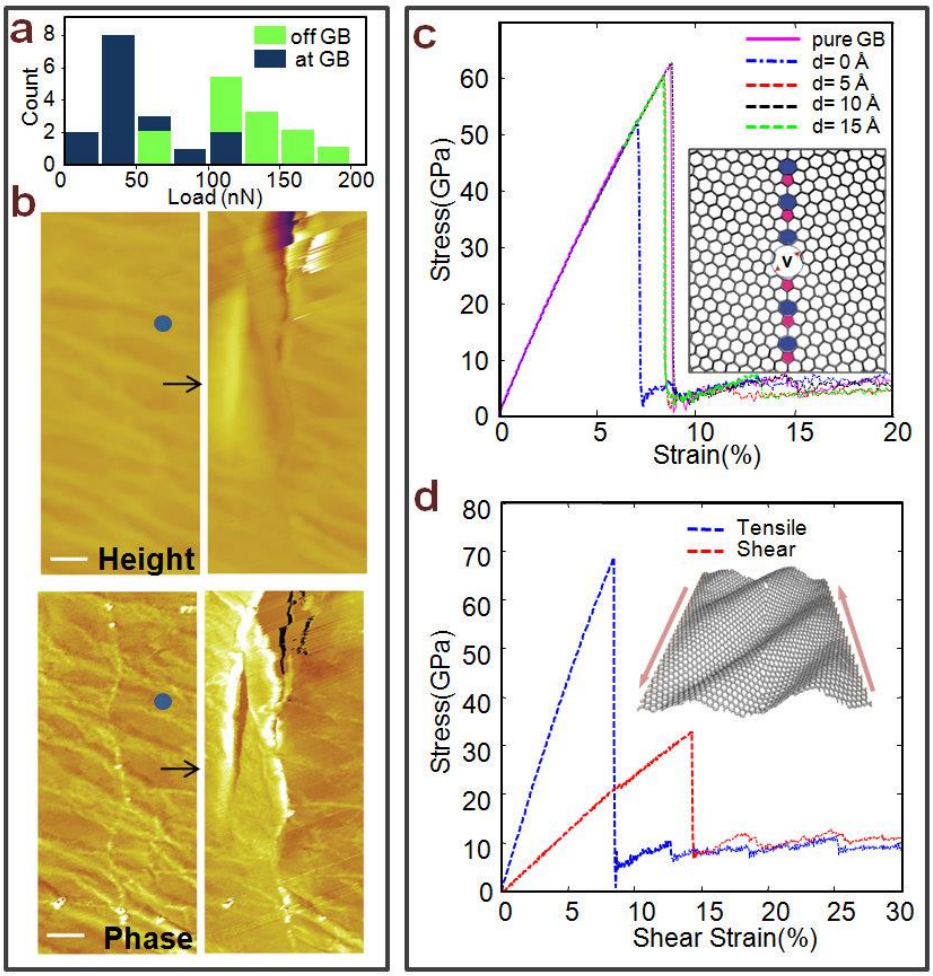

Figure 4.7 a) Breaking load histograms for force measurements performed at a grain boundary or away from a grain boundary (on average, 300 nm from a grain boundary). b) Height and phase AFM images show the region before and after an indentation measurement performed near a grain boundary (at the location indicated by the circle). As seen in the phase image (bottom) graphene tears along a grain boundary. Scale bars: 150nm c) MD simulations of the effect of a void on the strength of a small bicrystalline graphene sheet, varying its position with respect to a grain boundary. Inset: Schematic of model for the simulations for bicrystalline graphene with a void. d) MD simulation of decreased breaking strength due to shearing in the presence of a grain boundary, as shown in the inset.

In Eq. 4.2, F is the vertical breaking force, E_{int} is the intrinsic 2D elastic modulus of graphene and r is the radius of the indenter [1,25].

However, a recent theoretical study predicts the in-plane breaking stress for polycrystalline graphene to be in the range of 50-100 GPa, depending on the type of grain boundary [26].The discrepancy in the breaking stress in our membranes with these theoretical predictions suggests that grain boundaries alone are not responsible for the small breaking forces in our graphene membranes. Molecular dynamics (MD) simulations on a simplified system, undergoing uniaxial strain, shed some light on this issue.

4.4.1 Molecular dynamics simulations

We performed molecular dynamics (MD) simulations of the mechanical response of graphene to tensile load using the second generation reactive empirical bond order (REBO) potential [27] in the LAMMPS program [28]. The REBO potential has been widely applied to various carbon based nanomaterials. To avoid the well-known cutoff problem for bond breaking [29] in the REBO potential, we used the modified cutoff value (2.0Å) of the covalent interaction which minimizes the spurious overestimate of the interatomic forces. Simulations are performed at 300K with a strain rate of 0.0005/picosecond and an integration timestep of 1fs. Before loading the graphene, we equilibrated the different systems for 40 picoseconds in the isothermal-isobaric ensemble at room temperature to minimize stress. Then we applied the engineering strains and monitored the atomic stress tensor. The interlayer distance in graphite (3.4Å) is employed as the graphene thickness in calculating the total stresses. We validated our approach using the stress-

strain curves for perfect graphene and graphene with pure grain boundaries and our results for the stress-strain curves are consistent with other reports either from simulations [26,30] or experiment [1]. The simulated geometry of bicrystalline graphene was based on a dislocation model[31] for small-angle grain boundaries, where the grain boundary consists of a chain of 5-7 membered carbon rings. Depending on the grain boundary angle, the distance between pairs of 5-7 membered rings varies.

We considered an alteration to existing theoretical models, including voids into a bicrystalline model, which may further lower the breaking strength closer to the experimentally measured values. Our model membrane is illustrated in Fig. 4.7c, for a graphene grain boundary with misorientation angle of 21.8º. First, the distance

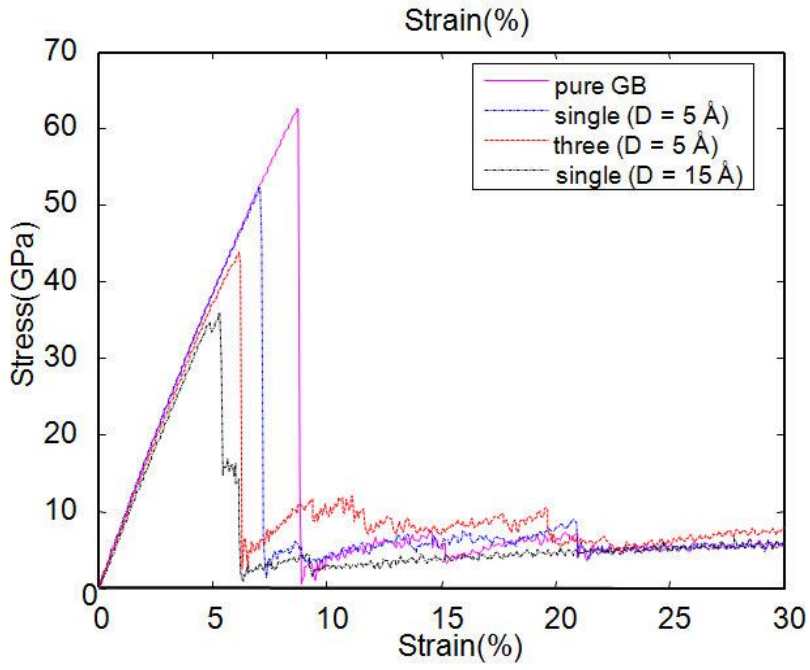

Figure 4.8 MD simulations of the effect of a void at the grain

between a void and a grain boundary is varied (d = 0, 5, 10 and 15 Å); Fig. 4.7c shows the corresponding stress-strain curves. For comparison, we also plotted the stress-strain curve for a pure grain boundary system. When such a void lies exactly along the grain boundary, the maximum stress is reduced about 15%, while voids near but not on the grain boundary have only a minute effect on graphene's mechanical strength. Additional voids along the grain boundary will further decrease the failure stress of the membrane (Fig. 4.8), and likely increasing the probability that unzipping along a grain boundary will occur. Not surprisingly, the effect of void size is even more pronounced in reducing the strength of bicrystalline graphene (Fig. 4.8). In short, the possible existence of different voids in graphene could couple with the grain boundaries formed by 5-7 member pairs, strongly decreasing CVD graphene's mechanical strength.

However, the loading conditions at the grain boundaries during AFM indentation are not a pure tension problem, since grain boundaries will often be oriented at an angle with respect to the radially directed tension induced by indentation, resulting in shear of the grain boundaries. We performed additional simulations to consider shearing. The same grain boundary structure is used, applying a pure shear instead of tension, as shown in Fig. 4.7d. Interestingly, the effect of shearing is significant and can cause additional weakening of graphene in the presence of grain boundaries. Our calculations show that voids with a diameter of 5 Å in the boundary reduces the shear strength from 32 GPa to 25 GPa. This 22% reduction of the shear strength is larger than the 15% reduction observed for the tensile strength.

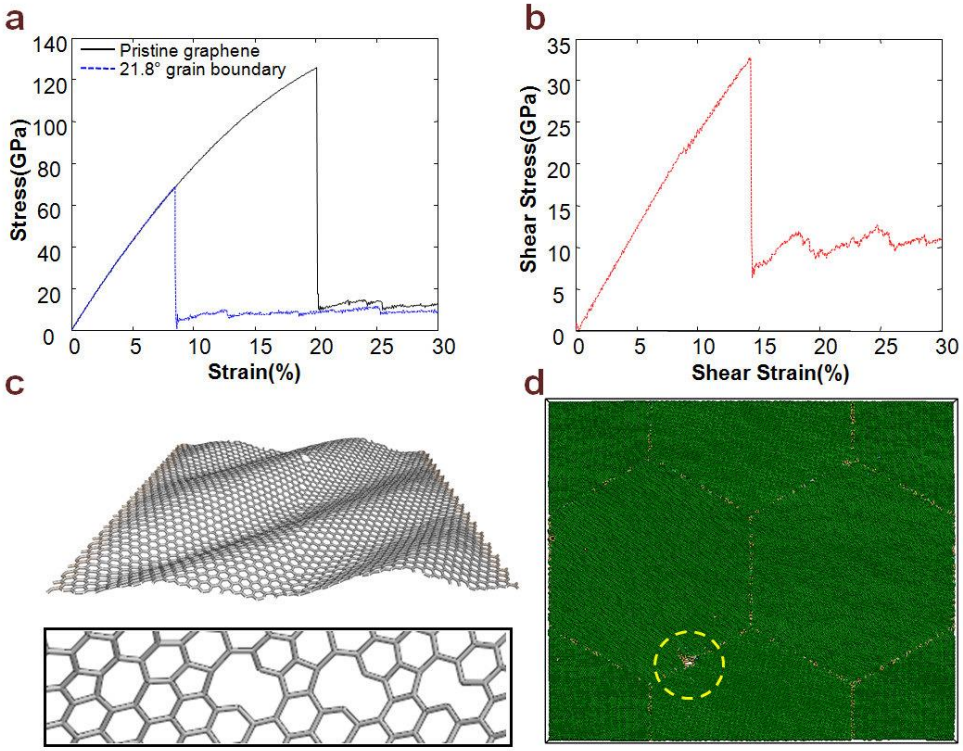

Figure 4.9 a) Stress-strain curves for pristine graphene and graphene with a 21.8° grain boundary. The maximum stresses are 126 GPa and 69 GPa, respectively, which agree well with previously reported values found in the literature. b) Shear stress-strain curve for graphene with a grain boundary. The maximum shear stress of 32 GPa is comparable to the coupling effect of grain boundary and void as discussed in the context. c) Snapshot of pure shear loading at critical strain and zoomed-in region of the grain boundary. Interestingly, the C-C bond in 7-membered rings always break first. d) Polycrystalline graphene model containing four grains with random misorientation angles. Atoms are color coded by coordination number. The region enclosed by the yellow dashed line demonstrates that the fracture starts from the grain boundary that is not normal to the tensile direction.

To further investigate this important role played by shearing loads, we implemented a slightly more complex and realistic model (Fig. 4.9), containing four grains with random misorientation angles. We observed that the fracture starts from a boundary lying at an angle with respect to the tensile direction; under the combined effect of shear and tensile loads, this grain boundary tears before others. Thus, grain boundaries appear to be especially vulnerable to complex load conditions which include a shear component. Together, our experimental and theoretical results suggest that an unzipping process at the grain boundaries can occur for loads smaller than those required to break a pristine grain boundary. As shown in more recent literature (see Chapter 7), a membrane is further weakened at the points where grain boundaries meet.

4.5 Reinforcing graphene membranes

Despite its high throughput in fabrication, the reduced breaking strength in CVD graphene can be undesirable for some applications. Here we demonstrate a possible approach to make stronger CVD graphene membranes. We created double layer membranes by simultaneously transferring a PMMA/graphene layer onto both sides of a nitride grid (Fig. 4.10), and then removing PMMA as previously described. The way PMMA/graphene films were scooped onto the target substrates is modified as shown in the schematic in Fig. 4.10a. Transferring graphene onto both sides of the nitride grids results in double layer graphene over the holes after the removal of PMMA (PMMA is still present in Fig. 4.10b). The yield is noticeably higher for the membranes where PMMA covers both sides of the nitride grid (darker regions), as can be seen in the SEM image in Fig. 4.10c.

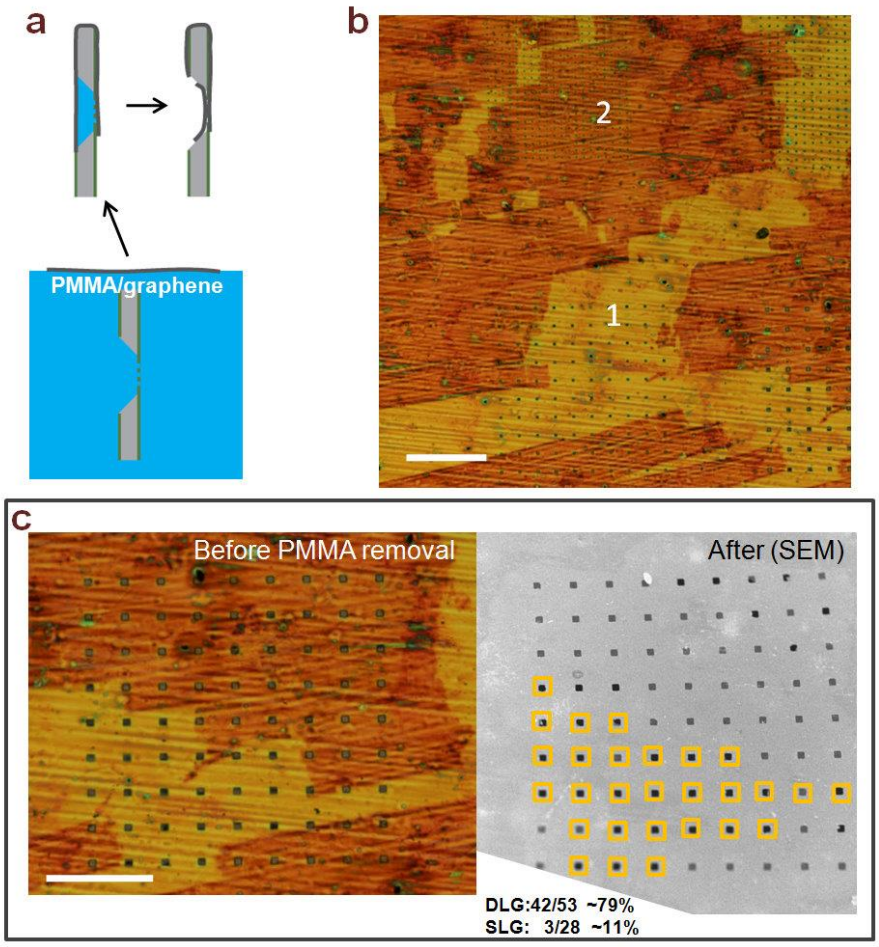

Figure 4.10 a) Schematic of double layer graphene (DLG) fabrication by scooping a PMMA/graphene film vertically, thus transferring it to both sides of a holey nitride membrane. b) Optical image of a nitride membrane after PMMA/graphene transfer. Darker regions (marked 2) have such a layer successfully transferred to both front and back of the nitride membrane. Scale bar: 200 μm. c) Optical image of a nitride membrane with dark regions corresponding to a PMMA/graphene layer on both sides of the nitride membrane. The holes are 10 by 10 μm. b) Scanning electron micrograph of the same region, after PMMA is removed by thermal decomposition. Yield in regions with a double layer is significantly higher (~79%) in comparison with the regions with only a single layer (~11%).

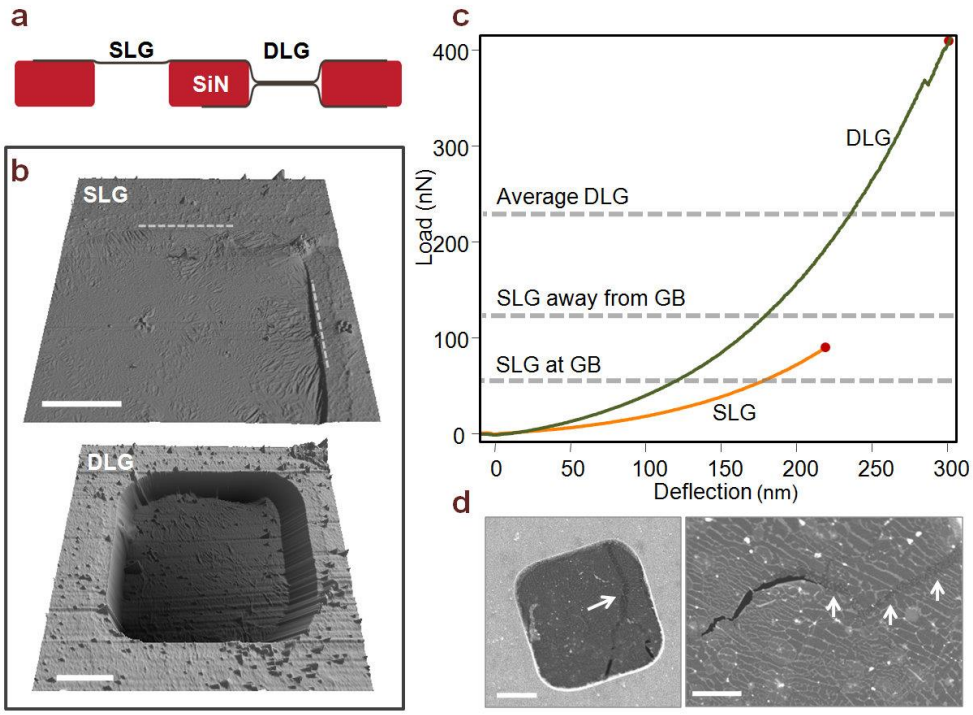

Figure 4.11 a) Cross section schematic of single layer graphene (SLG) and double layer graphene (DLG) on a silicon nitride grid. b) AFM height images of a single layer graphene membrane and a double layer graphene membrane. A single layer graphene membrane lies flatter on the surface of the grid (edge of suspended region indicated by dashed line). Scale bars: 2μm. c) Force curves for single and double layer graphene, indicating the increased breaking force resulting from the strengthening addition of a second layer. Average breaking forces for a double layer and single layers are also shown. d) Scanning electron micrographs of partially broken double layer graphene membrane. The "zebra-like" white lines are caused by residues of the wet transfer process, likely trapped between the two graphene layers. Scale bars: 2μm (left) and 1μm (right).

The process described results in a double layer over the holes in the nitride grid (Fig. 4.11a-b). We measured the resulting membranes and found that the effective 2D elastic modulus measured is roughly doubled compared with results from single layer graphene. We also observed that the strength of the resulting structure increased accordingly. For 13 double-layer graphene samples studied, we found an average breaking force of 230 nN, roughly twice the breaking force of single layer graphene which undergo indentation away from grain boundaries.

One interesting observation in these double layers was the overall mechanical resilience of the membranes during fabrication and indentation measurements. Initial breakages in these double layer membranes, are not immediately followed by complete failure, in contrast to single layer membranes. This can be directly seen when one of the layers starts tearing (Fig. 4.11d), as the other layer will continue to provide structural support for the rest of the membrane (in the scanning electron micrographs, darker shades indicated by the arrows are single layer, and in the black regions both graphene layers are missing). Because of this additional support, the double layer membranes were more likely to survive the fabrication process.

4.6 Conclusion

While we found that CVD graphene membranes behave differently than those fabricated with exfoliated graphene, our results suggest that controlling the ripple structure, either during the graphene growth or through external shear control, could be used as a knob to change a membrane's out of plane stiffness. Furthermore, improved synthesis techniques for producing graphene membranes with larger sizes [21,32] will prove critical for achieving CVD graphene with high breaking strengths.

Novel applications for graphene would greatly benefit from this progress, which can be assessed with these mechanical characterization techniques. CVD graphene membranes could be used, among some examples, as nanomechanical mass sensors, in flexible and transparent electronic devices, or as atomically thin separation windows to isolate different environments.

REFERENCES

[1] C. Lee, *et al.* Science **321**, 385 (2008).

[2] S. Bae, *et al.* Nat Nano **5**, 574 (2010).

[3] J. S. Bunch, *et al.* Science **315**, 490 (2007).

[4] C. Chen, *et al.* Nat Nano **4**, 861 (2009).

[5] Q. Yu, *et al.* Appl. Phys. Lett. **93**, 113103 (2008).

[6] A. Reina, *et al.* Nano Letters **9**, 30 (2009).

[7] K. S. Kim, *et al.* Nature **457**, 706 (2009).

[8] X. Li, *et al.* Science **324**, 1312 (2009).

[9] Y. Lee, *et al.* Nano Letters **10**, 490 (2010).

[10] H. Cao, *et al.* Appl. Phys. Lett. **96**, 122106 (2010).

[11] M. P. Levendorf, *et al.* Nano Letters **9**, 4479 (2009).

[12] B. Aleman, *et al.* ACS Nano **4**, 4762 (2010).

[13] A. van der Zande, *et al.* Nano Letters **10**, 4869 (2010).

[14] H. I. Rasool, *et al.* Nano Letters **11**, 251 (2011).

[15] J. S. Bunch, *et al.* Nano Letters **8**, 2458 (2008).

[16] W. Bao, *et al.* Nat Nano **4**, 562 (2009).

[17] Y. Wong, *et al.* J. Mech. Mater. Struct. **1**, 27 (2006).

[18] J. T. Robinson, *et al.* Nano Letters **8**, 3441 (2008).

[19] Y. Liu, *et al.* Nano Letters **10**, 2178 (2010).

[20] B. I. Yakobson, *et al.* ACS Nano **5**, 1569 (2011).

[21] P. Y. Huang, *et al.* Nature **469**, 389 (2011).

[22] K. Wan, *et al.* Thin Solid Films **425**, 150 (2003).

[23] K. Min, *et al.* Appl. Phys. Lett. **98**, 013113 (2011).

[24] V. B. Shenoy, *et al.* Phys. Rev. Lett. **101**, 245501 (2008).

[25] N. M. Bhatia, *et al.* Int. J. Non-Linear Mech. **3**, 307 (1968).

[26] R. Grantab, *et al.* Science **330**, 946 (2010).

[27] S. J. Stuart, *et al.* J. Chem. Phys. **112**, 6472 (2000).

[28] S. Plimpton, Journal of Computational Physics **117**, 1 (1995).

[29] T. Belytschko, *et al.* Phys.Rev.B **65**, 235430 (2002).

[30] Pei, Q. X., *et al.* Nanotechnology **21,** 115709 (2010).

[31] O. V. Yazyev, *et al.* Phys. Rev. B **81**, 195420 (2010).

[32] X. Li, *et al.* Nano Letters **10**, 4328 (2010).

CHAPTER 5

STRUCTURE AND PROPERTIES OF GRAINS AND GRAIN BOUNDARIES IN CVD GRAPHENE

5.1 Overview

This chapter is adapted from P. Y. Huang*****, C. S. Ruiz-Vargas*****, A. M. van der Zande*****, W. S. Whitney, M. P. Levendorf, J. W. Kevek, S. Garg, J. S. Alden, C. J. Hustedt, Y. Zhu, J. Park, P. L. McEuen, D. A. Muller, ***Nature*** 469 (2011).

We have directly encountered the effects of grain boundaries in graphene on the mechanical properties of graphene membranes, as described in the previous chapter. This should not be too surprising, as the properties of polycrystalline materials are often dominated by the size of their grains and by the atomic structure of their grain boundaries. These effects should be especially pronounced in two-dimensional materials, where even a line defect can divide and disrupt a crystal. These issues take on practical significance in graphene. Single-atom-thick graphene sheets can be produced by chemical vapor deposition on scales of up to meters [1], making their polycrystallinity almost unavoidable. Theoretically, graphene grain boundaries are predicted to have distinct electronic [2-4], magnetic [2], chemical [5] and mechanical [6,7] properties that strongly depend on their atomic arrangement. Yet because of the five-order-of-magnitude size difference between grains and the atoms at grain boundaries, few experiments have fully explored the graphene grain structure. In this chapter, results obtained with old and new transmission electron

microscopy techniques bridge these length scales. Using atomic-resolution imaging, we determine the location and identity of every atom at a grain boundary and find that different grains stitch together predominantly through pentagon–heptagon pairs. Rather than individually imaging the several billion atoms in each grain, we use diffraction-filtered imaging to rapidly map the location, orientation and shape of several hundred grains and boundaries, where only a handful have been previously reported. The resulting images reveal an unexpectedly small and intricate patchwork of grains connected by tilt boundaries, as it will be shown in later in this chapter.

These techniques open a new window for studies on the structure, properties and control of grains and grain boundaries in graphene and other two-dimensional materials. For example, by correlating grain imaging with scanning probe techniques, we have already shown in the previous chapter that these grain boundaries severely weaken the mechanical strength of graphene membranes. In this chapter we find that they do not as drastically alter their electrical properties.

5.2 Sample preparation

We grew single-layer graphene using CVD on copper foils in three ways. Growth method A: similar to methods described in the previous chapter, we annealed a 99.8% pure copper foil (Alfa Aesar #13382) at 1,000 °C at low pressure with an H_2 flow of 7 standard cubic centimetres per minute (sccm) for 10 min. We then grew the graphene at 1,000 °C by flowing CH_4:H_2 at 150:7 sccm for 10–15 min (varying growth time within this range did not yield noticeably different results). Samples are cooled for ~50 min while the CH_4:H_2 flow is maintained. Growth method B: this is identical to method A, except we used higher purity (99.999%) copper foil (Alfa

Aesar #10950). Growth method C: we used a rapid thermal processor tube furnace with a ~4″ inner diameter (MTI Corporation). We annealed copper foil (99.8% purity) at 1,000 °C (H_2, 300 sccm) for 30 min, and then grew the graphene at 1,000 °C (CH_4:H_2, 875:300 sccm) for 60 min. In all cases, our initial characterization of the resulting CVD graphene is done by Raman spectroscopy and scanning electron microscopy (SEM), as shown in Fig. 5.1.

We transferred the graphene either to commercial holey SiN TEM grids (such as PELCO Holey Silicon Nitride Support Films) with 2.5-μm-diameter holes or to Quantifoil holey carbon TEM grids to allow imaging of larger grains. Quantifoil grids are typically 10–20 nm thick, which is thin enough to allow DF-TEM imaging through the carbon support.

The fabrication for DF-TEM samples is a gentle graphene transfer method using a thin PMMA support, which produced roughly 90% coverage of TEM grid holes (that is, 90% of grid holes were uniformly covered with suspended graphene). After graphene growth on a copper foil, a thin layer of PMMA was spun onto the graphene (2% in anisole, 4,000 r.p.m. for 30 s), without a post-baking step. Copper was then etched away by floating the foil, PMMA side up, in a HCl/$FeCl_3$ copper etchant (Transene, Type 100/200). Next, the graphene and polymer support were washed by transferring them to deionized-water baths, taking care not to bring the PMMA into contact with liquids, to avoid depositing unwanted residues on the PMMA side of this layer. Finally, the PMMA–graphene layer is scooped out in pieces onto TEM grids. PMMA can be thermally decomposed [8], which is a gentler process than using liquid solvent rinses. We baked our samples in air (350 °C for 3–

4 h), without the use of an argon flow, which can slow the cleaning effect substantially. This step removes the PMMA layer, leaving the graphene freely suspended in a liquid-free release process. These high-yield samples were used in DF-TEM because they provided enough clean graphene to image large numbers of grains.

Our secondary technique produced cleaner, but lower-yield, graphene using a polymer-free transfer method. TEM grids are placed on top of the foil before etching and attached by dropping methanol on the grids. Our main addition to this technique

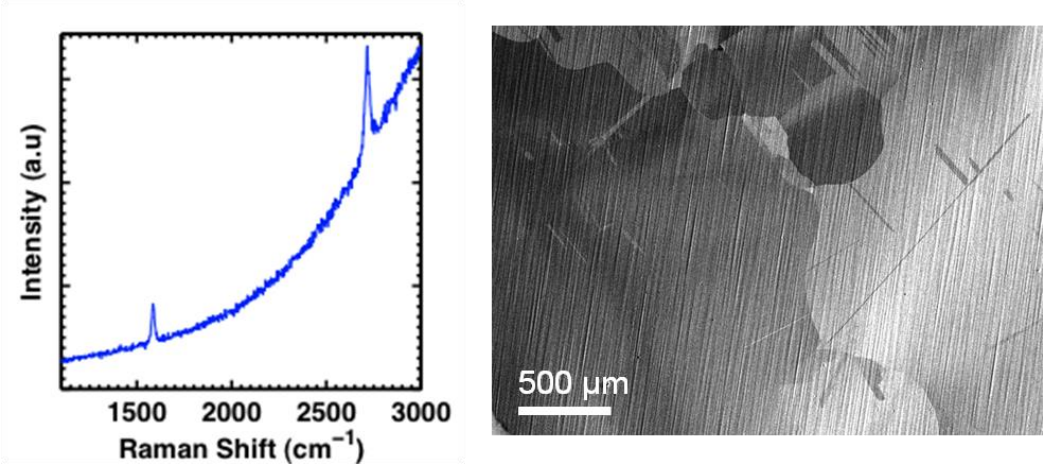

Figure 5.1 Representative Raman spectrum of single-layer graphene samples on copper. In most samples, we measure a very small or, as in this spectrum, undetectable D peak, indicating low disorder in our samples. The sloping background is due to the copper growth substrate. The SEM image corresponds to a copper substrate after graphene growth. Because of electron channeling effects, different copper grains have different brightness.

was to bake the final samples in a series of annealing processes increasing in temperature. The grids were then baked in air at 350 °C for 2 h. In this method, the samples are annealed in ultrahigh vacuum by ramping the temperature to 950 °C, holding this temperature steady for 15 min and then cooling to room temperature without active cooling. This annealing is done below the graphene growth temperature, and the micrometre-scale grain structure did not change afterwards. Thus, any change that may result from annealing should be small in comparison with changes occurring during the formation of the grain boundaries. A final step was to anneal the grids at 130 °C for >8 h before transferring them in air to the TEM. Because this transfer method uses no support film for the graphene as it is transferred, this method was a comparatively low-yield transfer process with coverage of just a few per cent over the holes. The advantage to this technique over the polymer-based transfer is that it produced graphene with less surface carbon contamination—regions hundreds of nanometres wide appeared atomically clean in ADF-STEM images.

5.3 Atomic resolution imaging

Figure 5.2a shows a large array of the suspended, single-layer graphene membranes used in this study. Unless otherwise stated, all data were taken on graphene grown with method A. To characterize these membranes at the atomic scale, we used aberration-corrected annular dark-field scanning transmission electron microscopy (ADF-STEM), where a 60-keV electron beam is scanned over the sample to study the lattice and atomic defects of graphene [9,10]. Figure 5.2b shows

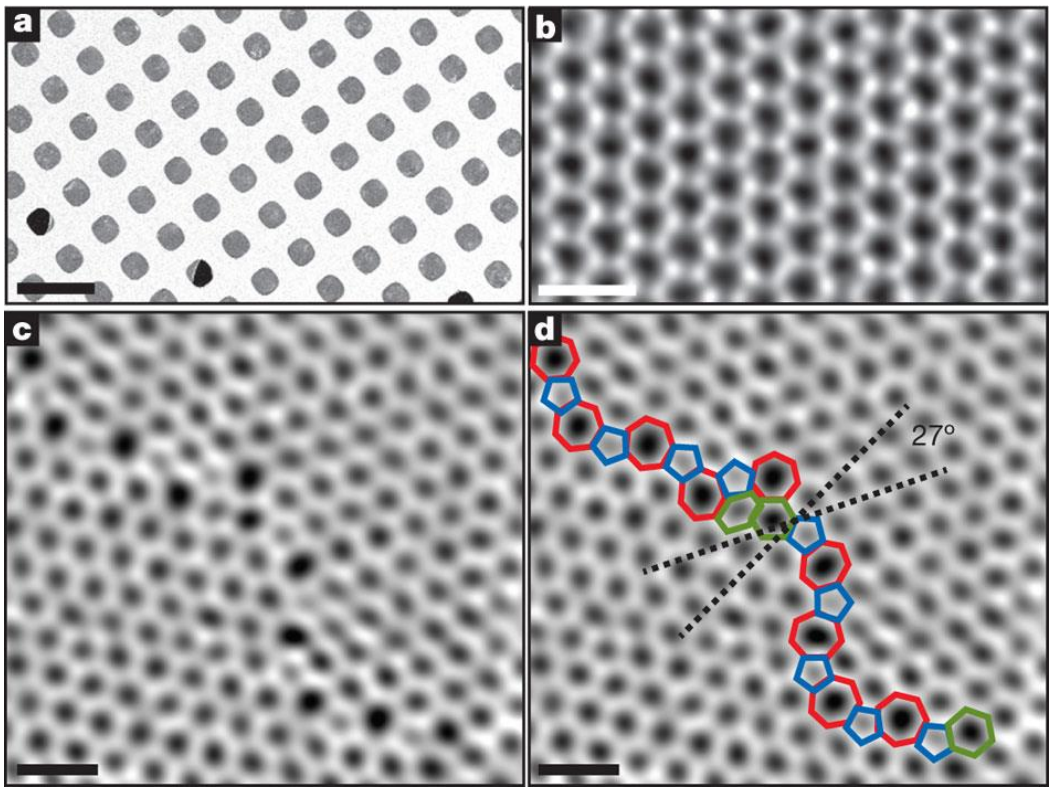

Figure 5.2 a) Scanning electron microscope image of graphene transferred onto a TEM grid with over 90% coverage using novel, high-yield methods. Scale bar, 5 μm. b) ADF-STEM image showing the defect-free hexagonal lattice inside a graphene grain. c), Two grains (bottom left, top right) intersect with a 27° relative rotation. An aperiodic line of defects stitches the two grains together. d), The image from **c)** with the pentagons (blue), heptagons (red) and distorted hexagons (green) of the grain boundary outlined. b)-d) were low-pass-filtered to remove noise; scale bars, 5 Å.

an ADF-STEM image of the crystal lattice within a single graphene grain. Away from the grain boundaries, such regions are defect free.

Imaging was conducted using a NION UltraSTEM100, with imaging conditions were similar to those used in ref. [9]. Using a 33–35-mrad convergence angle, our probe size was close to 1.3 Å. Because the low-voltage electron beam was below the damage threshold energy, the pristine graphene lattice remains stable and defect free. Images presented were acquired with the medium-angle annular dark-field detector with acquisition times of between 16 and 32 μs per pixel.

In Figure 5.2c, two graphene grains meet with a relative misorientation of 27°, forming a tilt boundary. As highlighted in Figure 5.2d, the two crystals are stitched together by a series of pentagons, heptagons and distorted hexagons. The grain boundary is not straight, and the defects along the boundary are not periodic. Although the boundary dislocation resembles structures proposed theoretically [4,6], its aperiodicity contrasts with many of these models and will strongly affect the predicted properties of grain boundaries. By analysing atomic scattering intensities [9], we confirm that the boundary is composed entirely of carbon. In addition, although high electron beam doses could induce isolated bond rotations, the boundary was largely stable under the 60-keV electron beam. Thus, the polycrystalline graphene is a strongly bonded, continuous carbon membrane. We also note that many grain boundaries are decorated by lines of surface particles and adsorbates, as discussed in other sections of this thesis, suggesting that, as predicted [5], they may be more chemically reactive than the pristine graphene lattice.

5.4 Dark-field TEM

Both STEM and TEM, which determine the positions and identities of atomic nuclei, are invaluable for understanding the local properties of grain boundaries. Using these atomic-resolution approaches, however, tens of billions to hundreds of billions of pixels would be needed to image even a single micrometre-scale grain fully, with estimated acquisition times of a day or more. Other candidates for characterizing grains on larger scales, such as low-energy electron microscopy and Raman microscopy, typically cannot resolve small grains and may be difficult to interpret. Fortunately, electron microscopy offers an ideal technique for imaging grains on the necessary length scales: dark-field TEM (DF-TEM), which is a high-throughput, diffraction-sensitive imaging technique that can be implemented on most TEMs built in the past sixty years [11]. This method is usually applied to foils about 100–300-nm thick, but we demonstrate below that, remarkably, it also works on single-atom-thick sheets—even on samples too dirty for atomic-resolution imaging. In this manner, DF-TEM provides a nanometre- to micrometre-scale grain analysis that complements ADF-STEM to give a complete understanding of graphene grains on every relevant length scale.

Figure 5.3a,b show a bright-field TEM image of a graphene sheet along with the selected-area electron diffraction pattern created from this region of the membrane. Owing to graphene's six-fold symmetry, electron diffraction from a single graphene crystal results in one set of six-fold-symmetric spots. Figure 5.3b contains many such families of spots, indicating that the field of view contains several grains of different

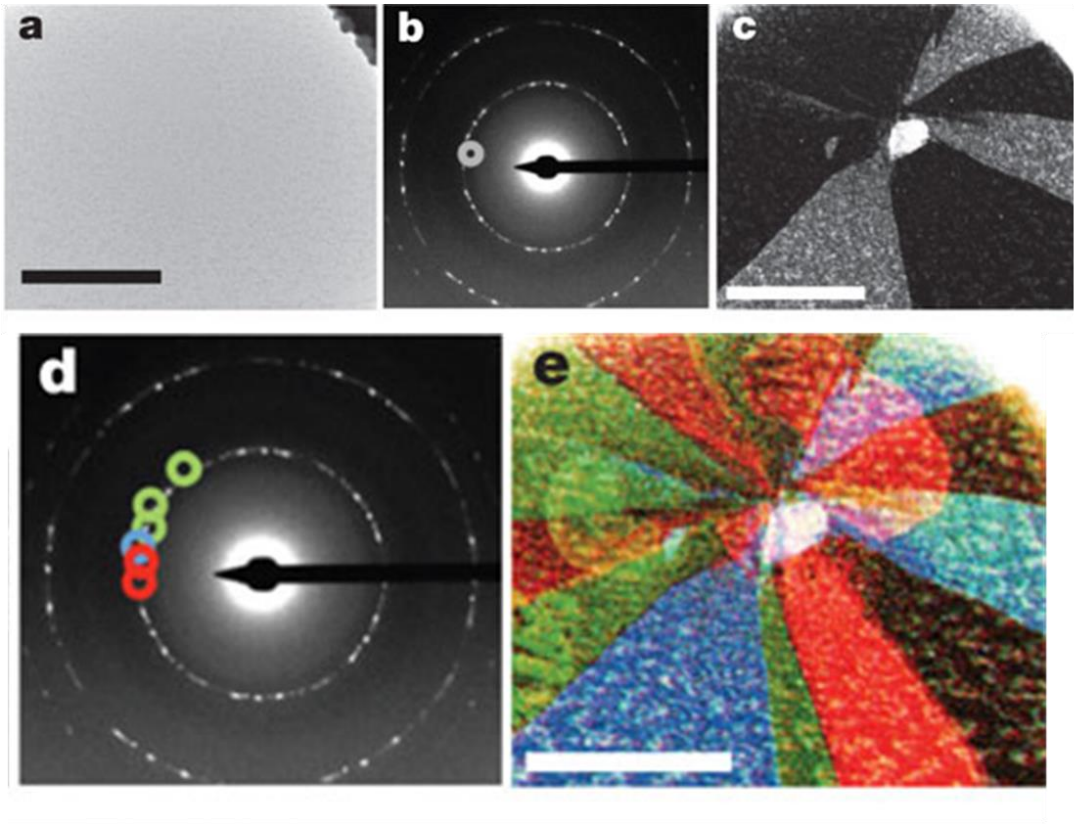

Figure 5.3 Grain imaging process. a) Samples appear uniform in bright-field TEM images. b) Diffraction pattern taken from a region in a) reveals that this area is polycrystalline. Placing an aperture in the diffraction plane filters the scattered electrons forming c), a corresponding dark-field image showing the real-space shape of these grains. d), Using several different aperture locations and colour-coding them produces e), a false-colour, dark-field image overlay depicting the shapes and lattice orientations of several grains.

orientations. DF-TEM images these grains one by one with few-nanometre resolution using an objective aperture filter in the back focal plane to collect electrons diffracted through a small range of angles, as shown by the gray circle in Figure 5.3b. The resulting real-space image (Figure 5.3c) shows only the grains corresponding to these selected in-plane lattice orientations and requires only a few seconds to acquire. By repeating this process using several different aperture filters, then coloring and overlaying these dark-field images (Figure 5.3d,e), we create

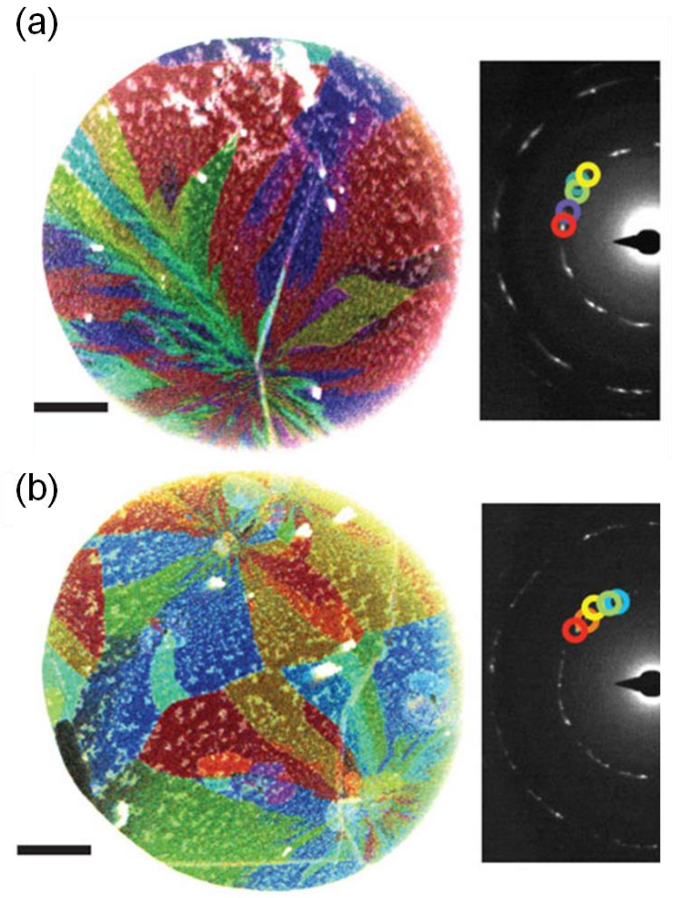

Figure 5.4 Images of regions where many grains emanate from a few points. Scale bars, 500 nm.

complete maps of the graphene grain structure, colour-coded by lattice orientation.

The images obtained are striking. The grains have complex shapes and many different crystal orientations, as can be seen in the additional examples in Figure 5.4. We observe special locations from which many grains emanate. Small particles and multilayer graphene also are often found near these sites. Both the average spacing (2–4 μm) and shapes of these radiant sites when we use growth method A are comparable with Raman and scanning electron microscope observations of graphene nucleation [12], suggesting that these locations are probably nucleation sites. Similar structures have been observed in studies of crystallization in colloids and are consistent with crystallization around impurities. Significantly, each apparent nucleation site gives rise to many grains of different orientations, resulting in a mean grain size much smaller than the nucleation density.

5.4.1 Dark field composite image process

TEM imaging was conducted using a FEI Technai T12 operated at 80 kV, which did not cause any apparent damage to the graphene membranes. Acquisition time for dark-field images were 5–10 s per frame. The spatial resolution in dark-field images ranges from 1 to 10 nm and is set by the size of the objective filtering aperture in a trade-off between real-space resolution and angular resolution in reciprocal space.

First, each raw DF-image is read in as a layer and aligned by hand to the other layers if necessary. Next, the images are adjusted to maximize brightness and contrast, making sure to adjust each image to the same brightness/contrast levels. Each layer is then colorized according to the color code on the boxes, and the layers are merged. The levels in the final image are adjusted, clipping the highest and

lowest intensities to enhance the image contrast. The overall color balance may be adjusted to enhance the color contrast in the image.

5.5 Grain size and orientation statistics

The distributions of grain size and relative angular orientation are readily determined from DF-TEM images. As discussed below, grain sizes are dependent on growth conditions, here ranging from hundreds of nanometres to tens of micrometres for slight changes in growth conditions.

In Figure 5.5a, we plot a histogram of grain sizes across several samples grown using method A. The mean grain size, defined as the square root of the grain area, is 250 ± 11 nm (s.e.m.). This size is much smaller than the grain size of the copper substrate [1,13] (100 μm–1 mm) and typical lateral grains measured in bulk, highly ordered pyrolytic graphite (6–30 μm) [14]. The inset in Figure 5.5a shows the cumulative probability of finding multiple grains in a given area. This plot demonstrates that micrometre-scale CVD graphene devices produced from this set of films will nearly always contain multiple grains. Figure 5.5.b shows a histogram of the relative crystallographic angles between adjacent grains. Because of graphene's six-fold crystal symmetry, the diffractive imaging technique only determines grain rotations modulo 60°. Consequently, the measurable difference between grain orientations is from 0 to 30° (with, for example, 31° measured as 29°). We observe a surprising and robust preference for low-angle (~7°) grain boundaries and high-angle (~30°) boundaries similar to that seen in Figure 5.3.

Additional information about these orientations comes from the larger-area diffraction patterns in Figure 5.5c, which we created by averaging diffraction data

sampled across 1,200-μm^2 regions of graphene. The broadened diffraction peaks in Figure 5.5c (left) show a distinct six-fold pattern, indicating that a significant fraction of the grains are approximately aligned across large areas This alignment

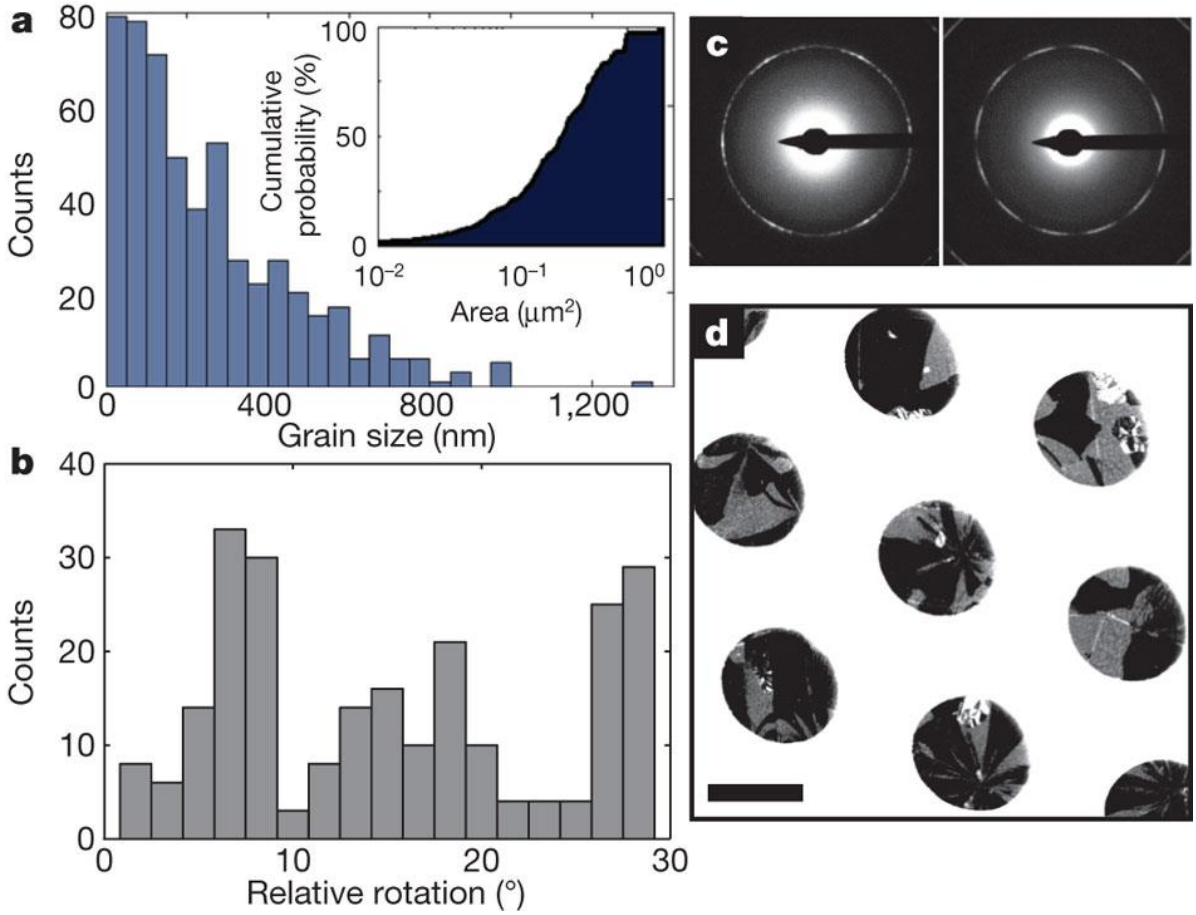

Figure 5.5 a), Histogram of grain sizes, taken from three representative samples using DF-TEM. The mean grain size is 250 ± 11 nm (s.e.m., n = 535). Inset, plot of the cumulative probability of having more than one grain given the area of a device. b), Histogram of relative grain rotation angles measured from 238 grain boundaries. c), d), Large-area diffraction patterns (c) and a low-magnification DF-TEM image (d) show that grains are globally aligned near particular directions. Scale bar, 2 μm.

can also be seen in Figure 5.5d, which is a low-magnification DF-TEM image showing grains with a small (~10°) range of in-plane lattice orientations. Almost half of the membrane appears bright, indicating that these grains are all approximately aligned. In contrast, a dark-field image of randomly oriented grains would only show roughly one-sixth (10°/60°) of the graphene membrane. In the diffraction pattern of a separately grown sample (Figure 5.5c, right), we instead find a clear 12-fold periodicity, indicating that there are two main families of grains rotated from one another by 30°. These distributions, which often contain smaller sub-peaks, are consistent with the frequent observation of low-angle and high-angle (~30°) grain boundaries. We attribute these alignments to registry to the copper substrate used for graphene growth. Such registry has recently been observed in low-energy electron microscopy and scanning tunneling microscopy studies of graphene growth on copper (100) and (111) surfaces [15].

5.5.1 Methods

In order to extract the statistics shown, grain sizes and orientations were measured on three different samples. To measure grain sizes, we determined the size of grains using raw DF-TEM. The original image contrast was too low to be extracted by simple thresholding, but high enough that grains were clearly recognizable. To make size determination easier, we first traced the edge of each grain by hand using the Magnetic Lasso tool in Photoshop and then filled them with color. The images were then fed into ImageJ where the grains were picked out by thresholding and their areas were measured. With these methods, we counted 535 grains for a sample obtained with Growth Method A, shown in the histogram. The

mean grain sizes reported in the text are number-averaged grain sizes (each grain is weighted equally in the average). The area-averaged grain sizes (each grain is weighted proportionally to its area), are roughly a factor of two larger than the number-averaged sizes: Growth Method A, 520 nm; Growth Method B, 830 nm; Growth Method C: 3.5 μm. To get relative grain orientations, we referred to DF-TEM composite images and their corresponding diffraction patterns. An example is shown in S5d, where the measured angles are displayed over the grain boundaries in question. For Growth Method A, we recorded 238 data points on 8 different membranes. Error in this measurement varies by data point and is typically ±2º, though it may be up to ±5º, depending on whether it is clear which diffraction peak results each grain. The upper bound on the angle is determined by the size of the objective aperture, and applies to highly polycrystalline regions with very closely spaced diffraction peaks.

5.6 Towards grain size control

By directly correlating grain structure with growth methods, these DF-TEM methods can be used to build on recent studies [12] that have demonstrated links between island nucleation density and growth conditions. Figure 5.6 shows three composite DF-TEM images of graphene grown using methods A, B and C. The slight differences between growth methods effected significant changes in the grain size, shape and crystallographic orientation of the CVD graphene. For example, with growth method C we observed grains averaging 1–4 μm, which is an order of magnitude larger than the grains grown using method A. Our DF-TEM methods

provide a powerful characterization tool for understanding and controlling grain growth, which will be a rich field of study important for graphene applications.

The ability to image the grain structure in graphene monolayers easily opens the door to the systematic exploration of the effects of grain structure on the physical, chemical, optical and electronic properties of graphene membranes. We find that such studies are further facilitated because grain boundaries are visible in scanning electron microscopy and atomic force microscopy (AFM) phase imaging owing to preferential decoration of the grain boundaries with surface contamination.

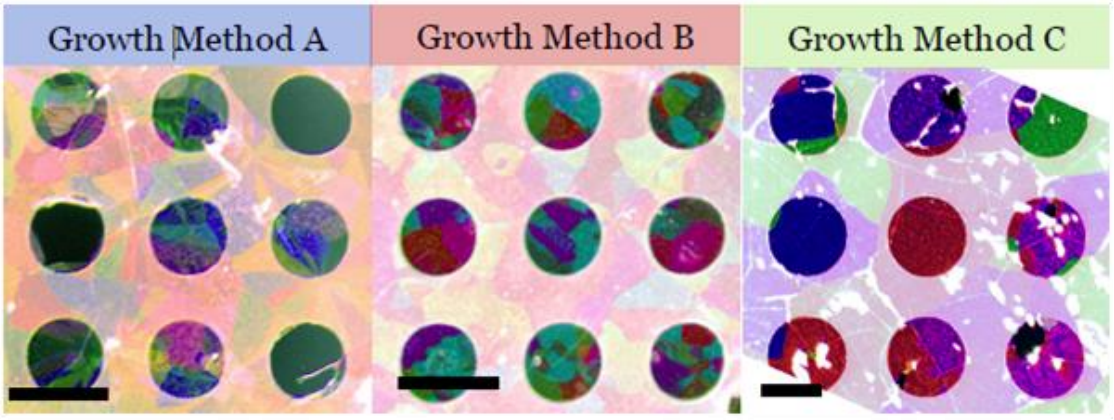

Figure 5.6 Composite DF-TEM images of grain structure show variations with growth condition. The mean grain sizes are 250 ± 11 nm (s.e.m.; growth method A, 99.8% pure copper), 470 ± 36 nm (s.e.m.; growth method B, 99.999% pure (ultrapure) copper) and 1.7 ± 0.15 μm (s.e.m.; growth method C (rapid thermal anneal)). The graphene is visible through the 20-nm, perforated amorphous-carbon Quantifoil support film. The graphene is broken over three of the perforations in a. Scale bars, 2 μm.

5.7 Electrical properties in polycrystalline graphene

We probed the electrical properties of polycrystalline graphene by fabricating electrically contacted devices (Figure 5.7) using graphene from all three growth methods. We fabricated top-gated graphene devices in four-point probe geometry. A transferred graphene film was patterned by photolithography and a 10-s exposure to an oxygen plasma to define the graphene strips. This was followed by fabricating 1.5-nm Ti/5.6-nm Au electrodes. We patterned a top gate, to measure the charge

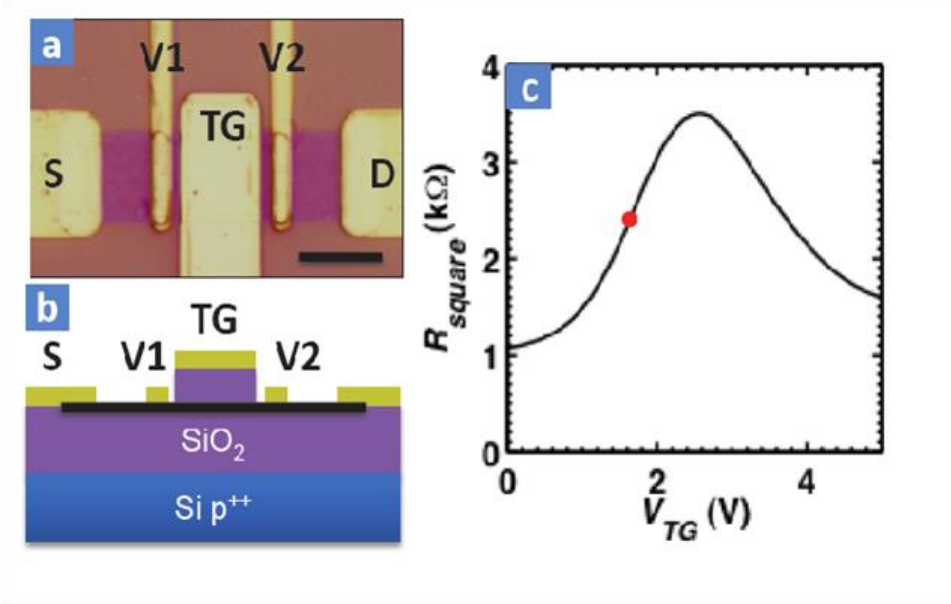

Figure 5.7 a), Contrast enhanced optical image of top-gated electrically contacted graphene in four probe geometry (Scale bar 10 μm). b), Side schematic of top-gated graphene device. Material thicknesses are not to scale. c), Four point transport measurement of graphene grown in Growth B as a function of top gate voltage. We extract a mobility of 9000 cm2/V*s from the point of largest slope (red dot).

mobility in graphene, by electron beam evaporation first of 90 nm of silicon oxide as a dielectric layer and then of a Cr/Au layer (1.5 nm/50 nm), without breaking vacuum between each evaporation.

We perform four probe transport measurements by applying a 30 mV source-drain bias on the outer electrodes. We then measure both the current flowing through the drain and the voltage difference between the inner electrodes *V1* and *V2*. By dividing these two numbers and scaling by the graphene size, we get the intrinsic resistivity of the graphene R_{square}. Figure 5.7c shows the graphene resistivity versus top-gate voltage V_{TG}.

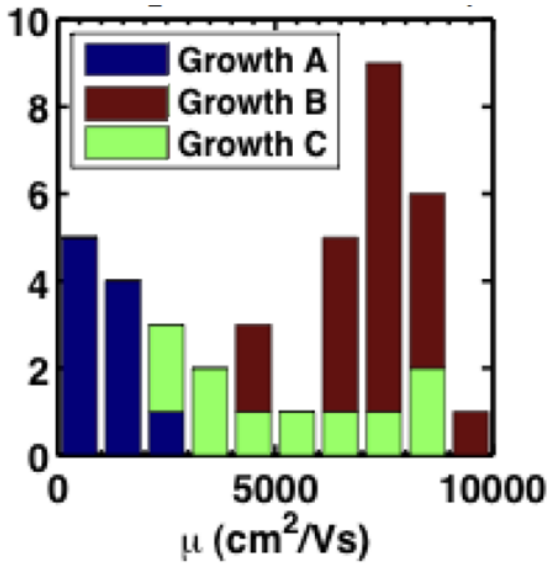

Figure 5.8 Vertically stacked histogram of number of devices with room-temperature mobilities, μ, measured from 39 devices using graphene growth methods A, B, and C.

Figure 5.8 shows a histogram of mobilities extracted from four-point transport measurements. Devices grown using methods A, B and C have room-temperature mobilities of $1{,}000 \pm 750$, $7{,}300 \pm 1{,}100$ and $5{,}300 \pm 2{,}300\ \mathrm{cm^2\ V^{-1}\ s^{-1}}$(s.d.), respectively. The mobilities for growth method A are comparable to previous results on CVD graphene, whereas the mobilities of growth methods B and C are closer to those reported for exfoliated graphene (1,000–$20{,}000\ \mathrm{cm^2\ V^{-1}\ s^{-1}}$). By comparing these measurements with the corresponding DF-TEM images in Fig. 5.6, we were surprised to find that, although mobility is clearly affected by growth conditions, high mobility does not directly correlate with large grain size.

Further work, by Q. Yu *et al.* and A. Tsen *et al.* [16, 17] investigated in more detail the effect of grain boundaries on electrical properties. One major conclusion from the latter work is that grain boundaries can differ depending on growth conditions, noticeably electric transport across them.

5.8 Conclusion

The imaging techniques reported here provide the tools to characterize graphene grains and grain boundaries on all relevant length scales. These methods will be crucial both for exploring synthesis strategies to optimize grain properties and for studies, such as those described above, on the microscopic and macroscopic impact of grain structure on graphene membranes. Thus, these results represent a significant step forward in realizing the ultimate promise of atomic membranes.

REFERENCES

[1] S. Bae, *et al.* Nat Nano **5**, 574 (2010).

[2] J. Cervenka, *et al.* Nat Phys **5**, 840 (2009).

[3] N. M. R. Peres, *et al.* Phys. Rev. B **73**, 125411 (2006).

[4] O. V. Yazyev, *et al.* Phys. Rev. B **81**, 195420 (2010).

[5] S. Malola, *et al.* Phys. Rev. B **81**, 165447 (2010).

[6] Y. Liu, *et al.* Nano Letters **10**, 2178 (2010).

[7] R. Grantab, *et al.* Science **330**, 946 (2010).

[8] L. Jiao, *et al.* J. Am. Chem. Soc. **130**, 12612 (2008).

[9] O. L. Krivanek, Nature **464**, 571 (2010).

[10] A. Hashimoto, *et al.* Nature **430**, 870 (2004).

[11] P. Y. Huang, *et al.* Nature **469**, 389 (2011).

[12] X. Li, *et al.* Nano Letters **10**, 4328 (2010).

[13] X. Li, *et al.* Science **324**, 1312 (2009).

[14] S. Park, *et al.* Carbon **48**, 797 (2010).

[15] J. M. Wofford, *et al.* Nano Lett. **10**, 4890 (2010).

[16] Q. Yu, *et al.* Nat. Mater. **10**, 443 (2011).

[17] A. Tsen, *et al.* Science **336**, 1143 (2012).

CHAPTER 6

ELECTRON TRANSPARENT GRAPHENE WINDOWS

6.1 Motivation

This chapter is adapted from the unpublished manuscript by C. S. Ruiz-Vargas, M. Wojcik, and J. Park, titled "Graphene windows for low-voltage scanning electron microscopy of samples in water".

Significant progress has been made in the use of electron microscopy for specimens in ambient conditions as well as in aqueous environments [1,2], a desired capability for studying various biological and material samples [3]. An important challenge in imaging these samples is ensuring their compatibility with the tool's vacuum environment during imaging [4]. From the early days of electron microscopy, the environmental transmission electron microscope (E-TEM) was developed for such purposes [5], which has enabled, for instance, TEM studies of multiphase interactions in a liquid environment [2]. Environmental scanning electron microscopes (E-SEM) with electron detectors operating in the presence of unreactive gases (pressures up to approximately 10 torr) were also developed [4,6,7]. Alternatively, a different approach relying on the encapsulation of the sample in a small environmental cell, with electron-beam transparent windows, has been explored for a few decades [1,8]. Various windows made from polyimide [9,10], silicon dioxide [11] or silicon nitride [12-14] membranes, with thicknesses in the few

tens to hundreds of nanometers, have been used to isolate the sample from the tool's vacuum.

With this method, both the thickness and the electron scattering efficiency of the window affect the image quality and spatial resolution. The choice of material for the encapsulating windows is particularly important for SEM, since much lower electron energies are used in comparison with TEM. Specifically, secondary electrons, emitted by the sample through inelastic processes, can provide detailed surface and topographic information in SEM imaging [15]. However, secondary electrons have energies lower than 50 eV, making windows transparent in this energy range a requirement for their detection. Currently available encapsulating windows for SEM are at least tens of nanometer in thickness, requiring electron energies usually larger than 10kV to ensure sufficient penetration of the electron beam through the membrane and reach the sample and to allow scattered electrons to reach the detector. Images obtained through these membranes are generated by collecting electrons backscattered from heavier elements in the sample and/or secondary electrons generated near the outer surface of the window. On the contrary, secondary electrons emitted by the sample itself, containing most surface and topographic information, are blocked by the membrane [16] and do not contribute to the image. Furthermore, spatial resolution is limited due to beam broadening caused by the electron-window interaction; while increasing the electron beam energy can reduce broadening, the interaction volume of the electrons with the sample increases for higher energies, also limiting imaging resolution. For these reasons, minimizing the thickness of the window is desirable in the design of better environmental cells

for SEM. The ultimate limit for reducing window thickness (thus increasing electron transmission) would be achieved by using atomically thin films, such as graphene [17,18]. Graphene would also provide additional benefits, including its outstanding in-plane thermal [19] and electrical conductivity, useful in dissipating heat and charge buildup during imaging [20]. Recently, graphene windows were used for the dynamic TEM imaging of nanoparticles in a liquid environment [21,22], and multi-layer graphene oxide windows ~20 nm in thickness were used for SEM imaging of nanoparticles at voltages as low as 3.0 kV [16].

6.2 Electron transparency of graphene membranes

The SEM images in this chapter were obtained with a Zeiss Ultra 55 microscope, using a high efficiency in-lens annular secondary electron detector (unless otherwise noted). Figure 6.1 shows examples of graphene membranes, imaged with the InLens detector (at an accelerating voltage of 1.5 kV), demonstrating graphene's transparency to electrons. We will also show some images obtained with an Everhart-Thornley type detector (SE2), which mostly collects type-II and type-III secondary electrons as well as some backscattered electrons. Images taken with these two detectors provide different information, and in general, graphene is much more visible when it is imaged using an in-lens detector, due to the detector's high sensitivity to surface composition (as this detector collects secondary electrons with the lowest energies).

To characterize graphene's transparency to electrons, we imaged gold nanoparticles on a partially torn graphene membrane, where a graphene fold covered

a number of the nanoparticles (region A in Figure 6.2). Images were obtained for various accelerating voltages for both detectors. While the same imaging conditions were used for all images, except for the different electron detectors used, the images

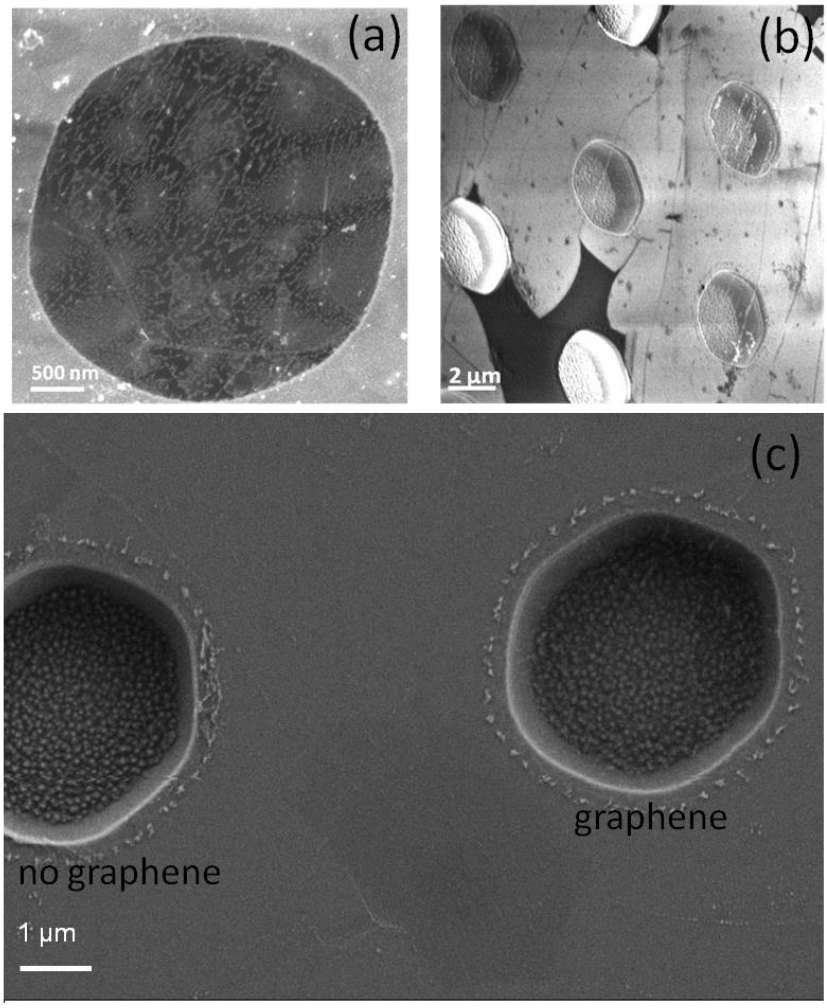

Figure 6.1. In-lens detector SEM images: a) Graphene is suspended over a through-wafer hole, so there is no bottom seen. b) Graphene suspended over some of the cavities shown in the image, etched into a Si wafer. The bottom of the cavities is still visible in the covered cavities. c) SE2 detector SEM image of similar cavities, and graphene is only covering the cavity on the right.

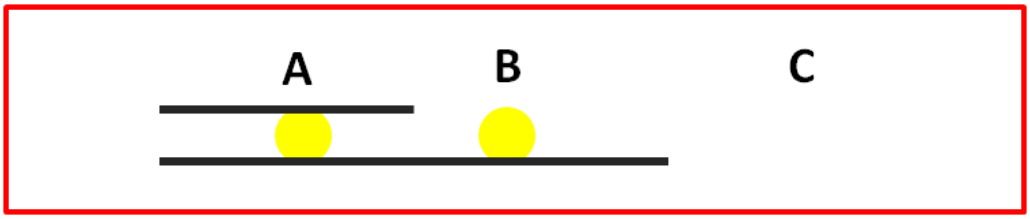

Figure 6.2 Schematic of graphene/nanoparticles arrangement for SEM images in Figure 6.3

were normalized to account for differences in the detectors' collection efficiencies and differences in the nanoparticles' secondary electron yield. This normalization was performed by taking the intensity of uncovered nanoparticles to be a gray scale maximum (region B), and aided by determination of the dark level in the area were graphene was torn (region C). The resulting images are shown in Figure 6.3. We calculated the relative contrast as a function of primary beam energy, by calculating the value I_{NP}-$I_G/I_{NP,}$ where I_{NP} and I_G are the gray scale value intensities for covered nanoparticles and a single layer of graphene, respectively. This value is similar for both detectors, and it rapidly increases even at the low-energy range tested.

We also calculated a "transparency ratio", obtained from the intensities of covered and uncovered nanoparticles. It can be seen that graphene appears more transparent when using the SE2 detector, as the ratio of the intensities is close to unity for electron energies of 1.5kV and above. For the in-lens detector, this ratio is close to 0.8 throughout for these low primary beam electron energies. The 20% loss is due to having fewer electrons from the primary beam impinging on the covered nanoparticles, as well as less secondary electrons crossing back the graphene membrane.

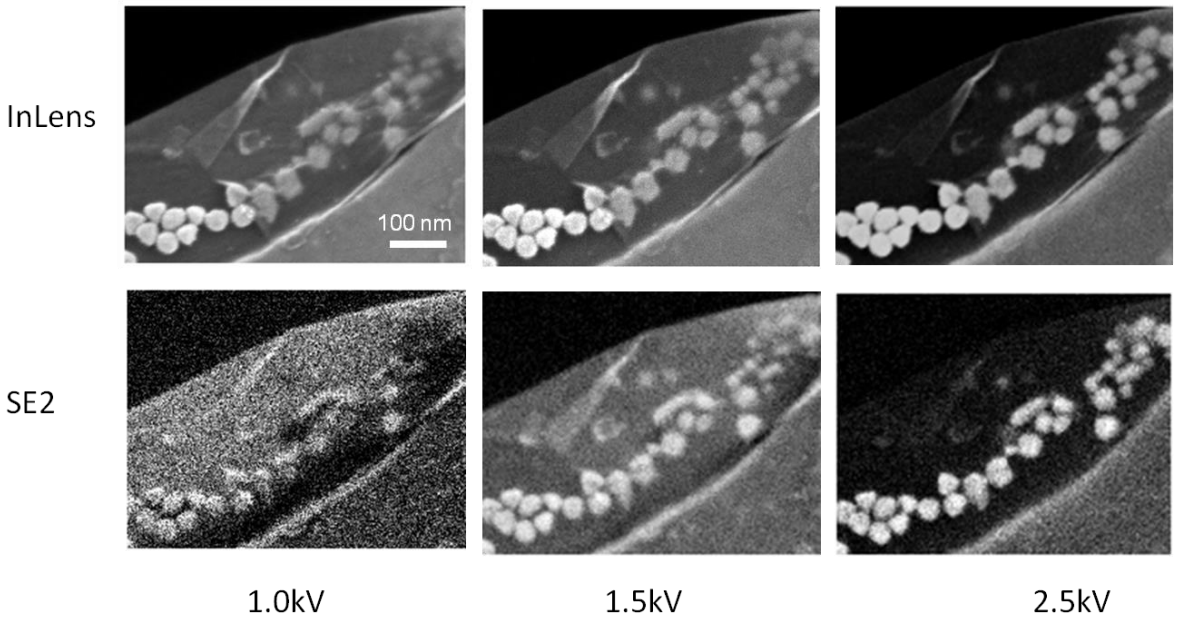

Figure 6.3. Images of gold nanoparticles on partially torn graphene membrane. The upper left part of the membrane is torn, and the right part of the membrane is folded over many of the gold nanoparticles. Images were obtained with InLens detector and SE2 detector, for electron beam energies of 1.0, 1.5 and 2.5kV.

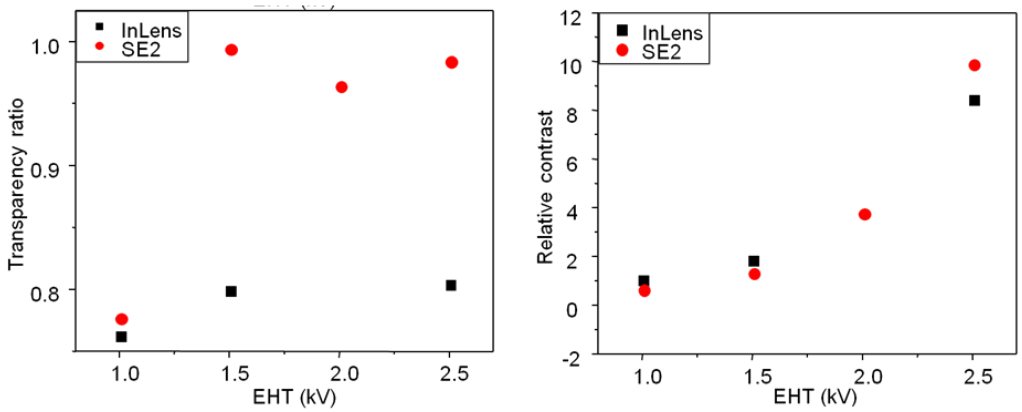

Figure 6.4. Relative contrast and transparency ratios, as a function of primary beam electron energies, from normalized images shown in Figure 6.3.

6.3 Fabrication of sealed chambers

We have fabricated SEM microcapsules containing water samples with the thinnest SEM windows to date, consisting of double-layer graphene, as shown in Figure 6.5. The capsules were first fabricated on Si wafers with low-stress silicon nitride membranes, defined by photolithography and a wet etch process. A small hole in the silicon nitride membrane, with a diameter ranging from 2 to 10 microns, was etched and then sealed by transferring a double-layer graphene window on top [23]. The double-layer graphene, produced by transferring two single layer graphene films grown by chemical vapor deposition, was used to increase the tear resistance of the windows [24]. The microcapsule (with a volume of ~0.1 microliters) can then be filled with a liquid, and then closed from the back with a cover glass and PDMS sealant (Fig. 6.5a,b). The optically transparent silicon nitride membrane further allows for the monitoring of the completed capsule before and after SEM imaging. For instance, the presence of water can be confirmed by the addition of fluorescein, which fluoresces only in an aqueous environment (Fig. 6.5c, inset). We found that liquid in a micro-capsule can remain sealed for 48 hours or longer. Figure 6.5c shows an SEM image of a water-filled micro-capsule with a graphene window.

To fabricate our micro-capsules we utilized standard {100} silicon wafers, 500 microns in thickness. A low-stress silicon nitride layer, ~300 nm in thickness, is grown on wafers by low pressure chemical vapor deposition. This is followed by standard contact photolithography, on the front and backside of the wafers, and a dry

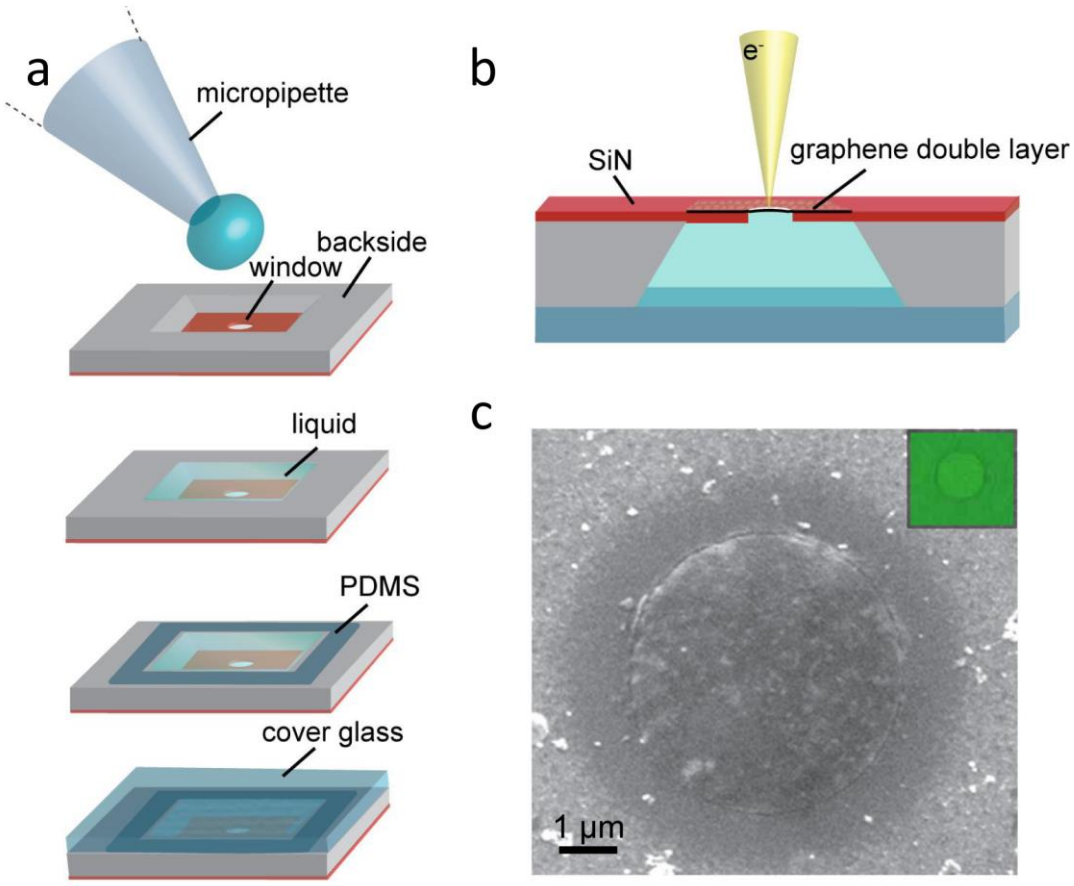

Figure 6.5. a) Schematic of microcapsule preparation. b) Sideview schematic of microcapsule. c) SEM image of graphene window, in-lens secondary electron detector at 1.0 kV. Inset: optical image of fluorescence in the same capsule, indicating the presence of water. The silicon nitride (SiN) membrane is partially transparent to light.

etch process to define features in the silicon nitride layer. The next fabrications step is to etch through the wafer, with a KOH etch. The silicon nitride is an ideal mask for this etch, which is performed at ~90°C, with an aqueous solution ~25% KOH by volume. The wafers are then rinsed and diced into separate devices onto which

graphene membranes are transferred to. To increase the mechanical resilience of our graphene membranes, double-layers are fabricated by growing graphene on two separate pieces of copper of similar size. Only one of them is coated with a PMMA layer (~75 nm in thickness). The copper foil covered with PMMA is etched (in an iron chloride solution), and the resulting PMMA/graphene film is rinsed and transferred to the copper piece without PMMA. After drying, the copper etch step is repeated, resulting in an additional layer of graphene being adhered to the PMMA protective layer. Finally, the resulting double-layer graphene/PMMA film is transferred to the front-side of the microcapsules. The PMMA layer is removed by thermal decomposition, by baking at ~350°C under the flow of argon.

Finally, the micro-capsule is filled and sealed as shown in Fig. 6.5. First, a thin layer is PDMS is manually applied to the backside, then the cavity is filled from the backside with a micro-pipette, and then a cover glass is gently placed on top, with the PDMS conforming to it providing a gentle seal.

6.4 Indentation of graphene on water

The presence of water can be confirmed optically, and it is also detectable in the indentation measurements. Figure 6.6 shows a height image in 3D, obtained by atomic force microscopy (AFM). This membrane was indented with the AFM tip, before and after introducing water to the chamber. As described in Chapter 4 and in other studies [24,25], the membrane's mechanical response can be used to calculate its effective 2D elastic modulus and pretension. The 2D effective elastic modulus,

E_{2D}, roughly doubles from 115 N/m before introducing water, to 239 N/m in the same membrane, after water is introduced in the chamber (Fig. 6.6b). The pretension, σ_{2D}, increases in the presence of water, from 0.026 N/m to 0.068 N/m. The incompressibility of water is likely responsible for the change in the elastic modulus. Surface tension at the water-graphene interface could also affect graphene's response to indentation.

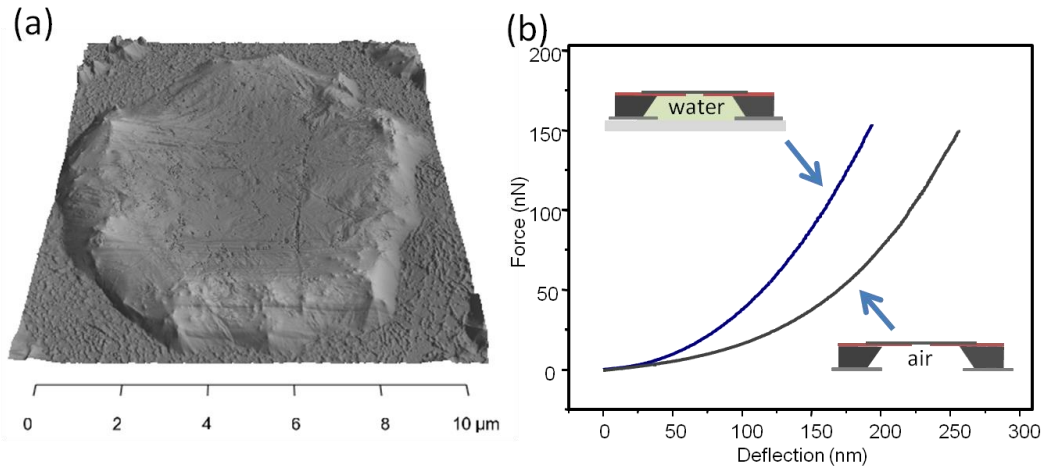

Figure 6.6. a) 3D rendering of the AFM height image of a graphene membrane, sealing a liquid-containing enclosure. b) Nanoindentation curves obtained from the same membrane before and after the enclosure was filled with water.

6.5 SEM testing of graphene-sealed capsules

In Figure 6.7, we demonstrate the use of our graphene covered microcapsules. We imaged gold nanoparticles (60 nm in diameter) in water with the in-lens secondary electron detector. As comparison, we also tested a commercially available polyimide-based environmental cell (Quantomix) by imaging Au NPs with

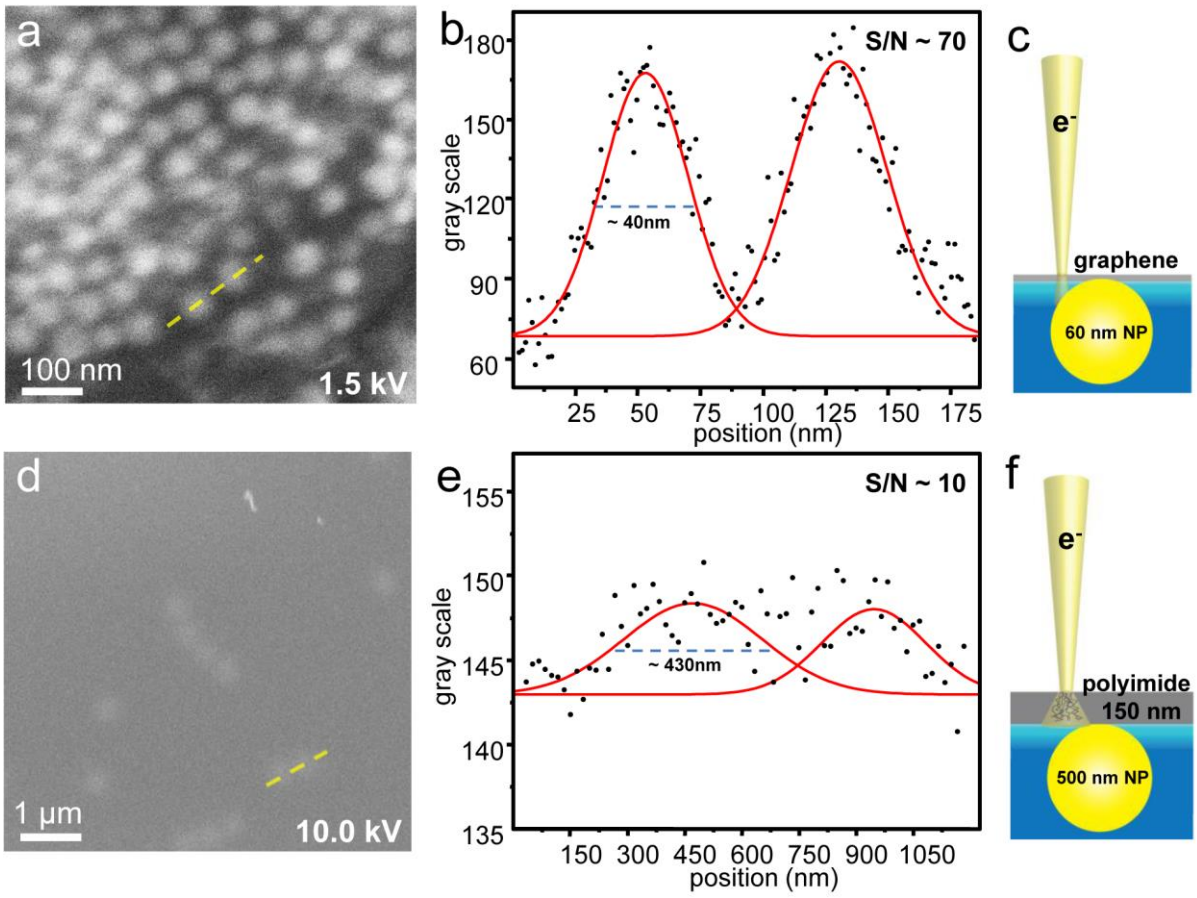

Figure 6.7. a) SEM image of gold nanoparticles (60 nm) in water obtained through a graphene-window with an in-lens secondary electron detector. b) Gray scale values along dashed line in previous image. c) An atomically thin window allows for good image contrast and resolution. d) SEM image of gold nanoparticles (500 nm) in water through a commercially available polyimide window, 150nm in thickness. Same in-lens detector was used. e) Gray scale values corresponding to two gold nanoparticles in the previous image (dashed line). f) Schematic of electron beam broadening due to scattering through the polyimide membrane.

a much larger average diameter (500 nm) using the same electron detector (Fig. 6.7d). In the case of the graphene windows, images were obtained at acceleration voltages as low as 1.5kV with good image contrast and resolution. On the other hand, the use of a polyimide membrane (150nm thick) did not allow imaging of the larger nanoparticles, at similar low voltages, and could only be imaged with larger beam energies (>10.0 kV). Furthermore, we found that the signal to noise ratio was nearly an order of magnitude higher when imaging through graphene, despite the smaller size of AuNPs. The improvement is a result of a higher electron transmission and a weaker background signal; the graphene membrane transmits both the primary beam and electrons emitted from the sample, while generating fewer backscattered and secondary electrons than its polyimide counterpart. The spatial resolution when imaging through the graphene window is also improved, as electron beam broadening is minimized (Fig. 6.7c, f).

6.6 Dynamics during SEM imaging

One important application of electron microscopy of samples in water is the observation of dynamic processes. An example of dynamic imaging is shown in Figure 6.8, where three SEM images of AuNPs in water taken at different times (30 seconds interval) are compared. While most NPs remain static in all three images (examples marked by white arrows), new particles appear in the second and the third image. These changes, in the position and density of the AuNPs, suggest two distinct behaviors of NPs in water during the SEM imaging. While most NPs at the interface

of water and the graphene window tend to remain static, NPs away from the surface continue to move around but get stuck when reaching the interface. This explains the general tendency toward increased NP density. We also note that other residues (marked by the dashed line in Fig. 6.8a) also undergo visible changes during imaging both in brightness and shape.

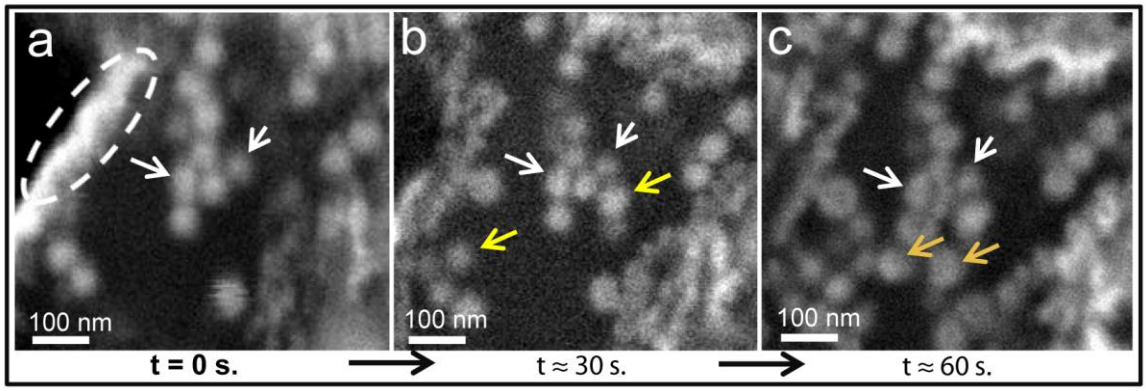

Figure 6.8. a) SEM images of gold nanoparticles in water, 30 seconds apart. The particles shown by the white arrows remain static throughout. Images were taken at 1.5 kV with the in-lens secondary electron detector. The region enclosed by the dashed line is an example of non-metallic residue visible during imaging. b) The new arrows show two examples of particles which were not visible previously. The contrast and shape of unidentified residues in the image has also changed. c) The new arrows show two more examples of particles which have just become visible.

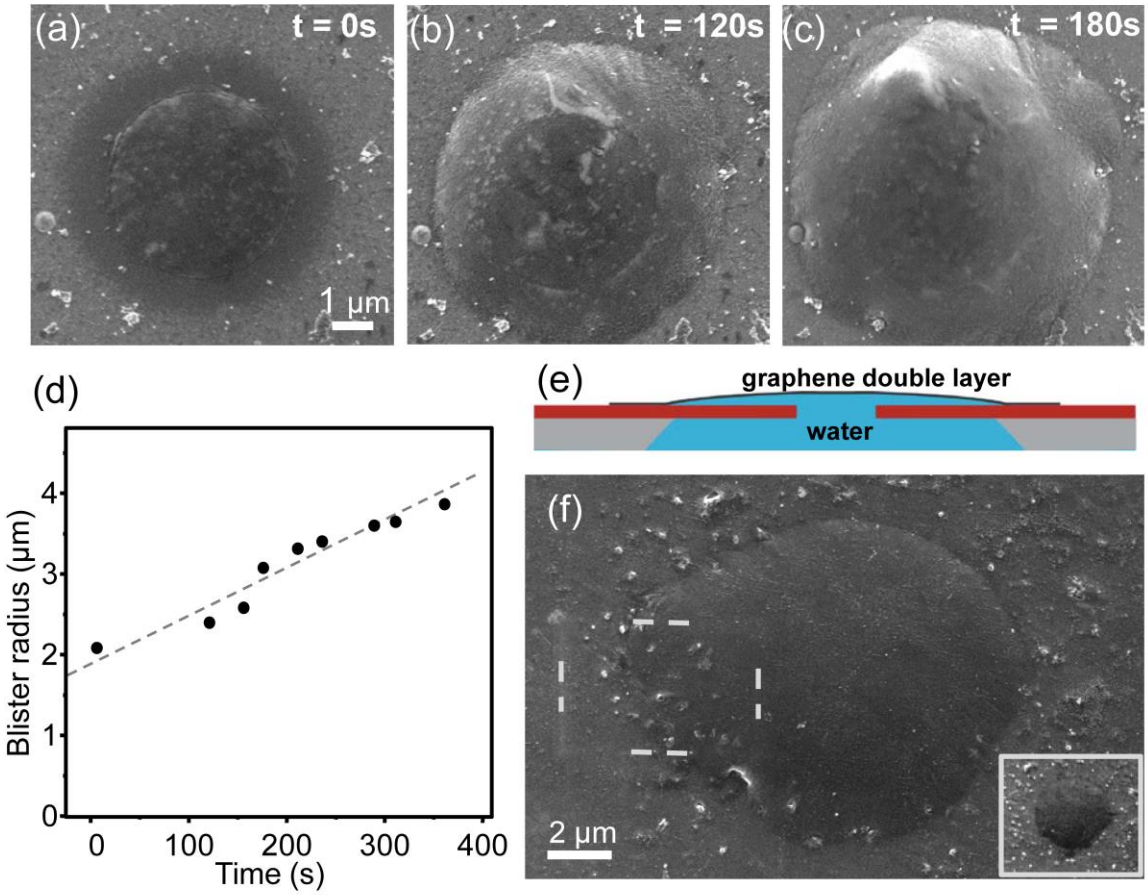

Figure 6.9. a) SEM image of graphene window, taken with in-lens detector at 1.0 kV. b) SEM image of same graphene window, obtained with the 120 seconds later. c) SEM image taken 180 seconds after the first image. d) Plot of radius of delaminated graphene window with time, measured from the graphene window shown in the previous images. e) Schematic of graphene delamination, forming a blister above the silicon nitride membrane. f) Asymmetric delamination in a different graphene window, induced by the electron-beam focused on the left side of the window (along dashed lines). Inset: same graphene window, before delamination.

During imaging, we also observe the effect of the electron beam on the environmental-cell itself. For example, the graphene window shown in Figure 6.9a-c changes shape during extended SEM imaging. Figure 6.9d shows that the radius of a delaminating graphene blister increases roughly linearly with time. The images were

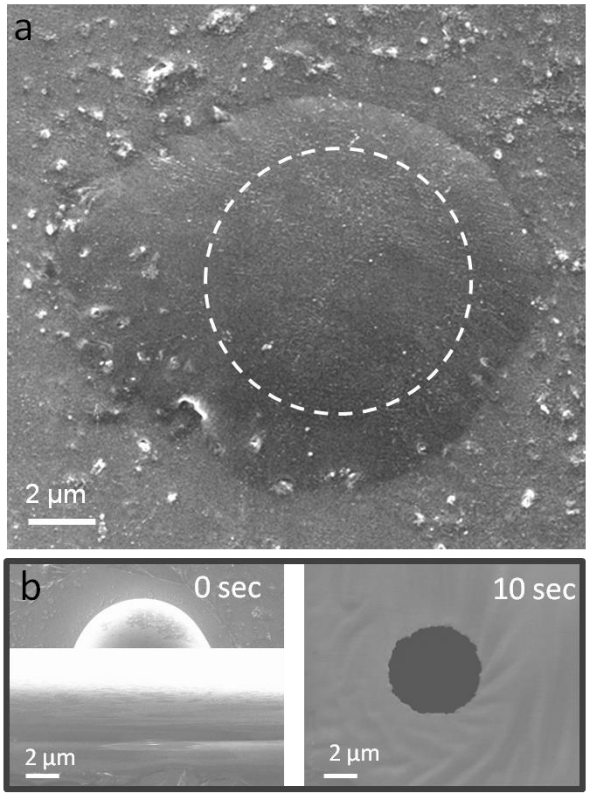

Figure 6.10. Image of graphene window, before and after sudden bursting. a) Before it bursts, the hole in the nitride membrane is obscured by a thin layer of water (dashed line). b) During bursting, the contour of the hole in the nitride membrane is

taken with a primary beam electron energy of 1.0 kV. It is likely that these changes are caused by water seeping between the silicon nitride and graphene interface. We notice that these changes occurred only in the presence of the scanned beam, as exposing sealed microcapsules to vacuum prior to SEM imaging does not cause delamination. Furthermore, by zooming in on one edge of a graphene window, an assymetric delamination was induced, as shown in Figure 6.9f (a different graphene window than the one shown in the previous images). In this last image, a few scans were performed in the rectangular region denoted with the dashed lines. Finally, as shown in Figure 6.10, a graphene window can burst.

Graphene delamination might be caused by local heating of water near the surface, weakening adhesion at the silicon nitride/graphene interface. The incompressible nature of water, in comparison to gases, will prevent graphene from re-adhering to silicon nitride as the delamination advances, making the process irreversible. This effect should be taken into consideration in revised capsule designs, for example by transferring the graphene window to the inside of the capsule, which would prevent exposing the silicon nitride/graphene interface to liquid.

6.7 SEM images with different detectors

Graphene windows could enable direct observations of the graphene-water interface. We can compare SEM images obtained with two different secondary electron detectors at an electron energy of 1.0kV (Fig. 6.11). The in-lens detector (Fig 6.11b) collects secondary electrons with the lowest energies [26] and is highly

sensitive to surface composition. On the other hand, the SE2 detector (Fig 6.11c; Everhart-Thornley type) located at a larger angle from the sample, is more sensitive to the sample's surface topography [27]. Both images show a water capsule sealed by a doble layer graphene window, where the original edge of the hole in the silicon nitride membrane is marked by a dashed line in Fig 6.11b. They also show a thin layer of water present between the double layer graphene and the silicon nitride membrane after continuous imaging (schematic shown in Fig 6.11a).

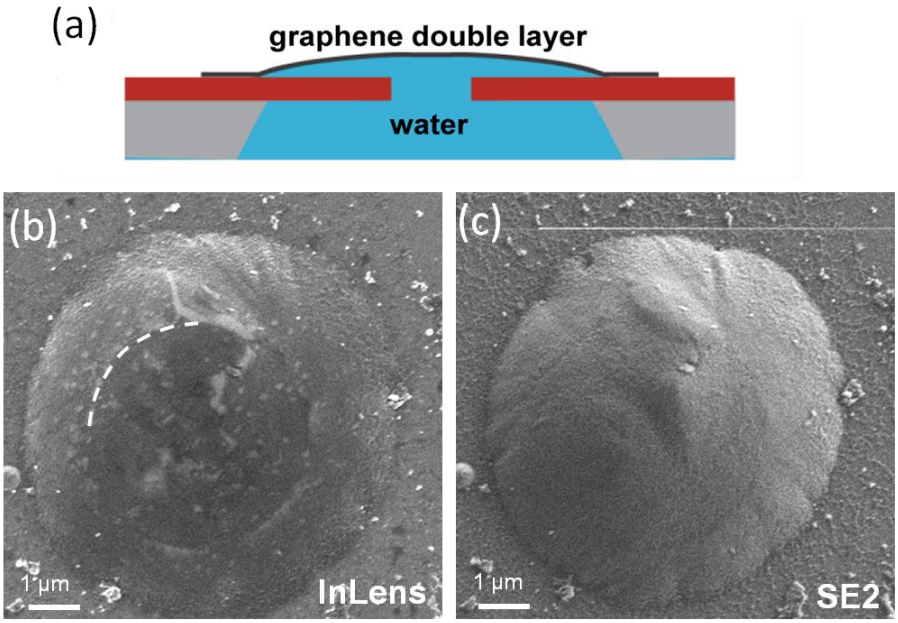

Figure 6.11. a) Sideview schematic of a thin water layer between graphene and the SiN membrane. b) SEM image at 1.0 kV. c) SEM image of the same region, obtained with the SE2 secondary electron detector at 1.0 kV.

With the in-lens detector (Fig 6.11b), the graphene-covered water region appears darker than the silicon nitride due to the lower secondary electron emission coefficient of water, while arbitrary particles present inside of the chamber and the edge of the hole in silicon nitride are clearly visible. We estimate that the features located within ~50nm from the graphene-water interface can be imaged, as a penetration depth of ~50 nm in water is estimated for a 1.0 kV beam according to the Kanaya and Okayama expression [28], assuming negligible electron scattering by graphene. On the contrary, in the image obtained with the SE2 detector (Fig. 6.11c) the bulged topography of the graphene membrane is brighter than the surrounding regions, while the edge of the hole in the silicon nitride membrane is barely discernable. Our results suggest that it is possible to study the top-most layer of water (and other liquids) and its contents using our graphene-sealed microchamber, which could be useful for the investigation of surface and/or interface specific dynamics.

6.8 Conclusions

We have demonstrated the use of double-layer graphene windows for SEM imaging of samples in water. We further expect that advances in CVD graphene growth could enable the use of single-layer graphene for this purpose by minimizing graphene defects and weak grain boundaries, for instance. Improved transfer techniques could also increase the fabrication yield of these structures, enabling the batch fabrication of graphene-sealed micro-capsules. Such improvements may lead to the integration of a graphene-based imaging platform with microfluidic

technology [29], which could enable SEM imaging under a continuous flow of samples. Such graphene-based imaging devices for SEM could prove useful in a variety of fields, including the study of biological systems, electrochemical and catalytic reactions.

REFERENCES

[1] D. F. Parsons, *et al.* Adv. Biol. Med. Phys. **15**, 161 (1974).

[2] L. L. Dai, *et al.* Langmuir **21**, 2641 (2005).

[3] N. de Jonge, *et al.* Nat Nano **6**, 695 (2011).

[4] D. J. Stokes, Phil. Trans. R. Soc. Lond. A **361**, 2771 (2003).

[5] E. Ruska, Kolloid Z. **100**, 212 (1942).

[6] Collins S.P., *et al.* Microsc. Res. Techniq. **25**, 398 (1993).

[7] S. E. Kirk, *et al.* J. Microsc. **233**, 205 (2009).

[8] I. M. Abrams, *et al.* J. Appl. Phys. **15**, 607 (1944).

[9] S. Thiberge, *et al.* Proc. Natl. Acad. Sci. **101**, 3346 (2004).

[10] E. U. Donev, *et al.* Nano Lett. **9**, 2715 (2009).

[11] K. L. Liu, *et al.* Lab Chip **8**, 1915 (2008).

[12] M. J. Williamson, *et al.* Nature Mater. **2**, 532 (2003).

[13] N. de Jonge, *et al.* Proc. Natl. Acad. Sci. USA **106**, 2159 (2009).

[14] J. M. Grogan, *et al.* J Microelectromech Syst **19**, 885 (2010).

[15] Jaksch, H., *et al*, Springer Berlin / Heidelberg, (1995).

[16] M. Krueger, *et al.* ACS Nano **5**, 10047 (2011).

[17] J. C. Meyer, *et al.* Nature **446**, 60 (2007).

[18] J Y Mutus, *et al.* New Journal of Physics **13**, 063011 (2011).

[19] A. A. Balandin, *et al.* Nano Lett. **8**, 902 (2008).

[20] N. Mohanty, *et al.* Nano Lett. **11**, 1270 (2011).

[21] H. Zheng, *et al.* Nano Lett. **9**, 2460 (2009).

[22] J. M. Yuk, *et al.* Science **336**, 61 (2012).

[23] X. Li, *et al.* Science **324**, 1312 (2009).

[24] C. Ruiz-Vargas, *et al.* Nano Lett. **11**, 2259 (2011).

[25] C. Lee, *et al.* Science **321**, 385 (2008).

[26] K. Kumagai, *et al.* Ultramicroscopy **109**, 368 (2009).

[27] J. Hejna, Scanning **17**, 387 (1995).

[28] S. O. K Kanaya and Okayama, J. Phys. D **5**, 43 (1972).

[29] E. A. Ring, *et al.* Microsc. Microanal. **16**, 622 (2010).

CHAPTER 7

OUTLOOK AND CONCLUSION

7.1 In the meantime

One can attempt to find absolute answers to important research questions. However, graphene related fields are still growing, and progressing at tremendous speed. Partly due to the urgency with which results need to be published, the existing literature will present the latest results from around the globe without considerable delays. Most impactful findings are rapidly verified by other research groups, while also motivating further work. This final chapter provides a brief review on recent progress related to this thesis, reported after the manuscripts that compose the majority of the previous chapters were published.

7.1.1 Mechanical properties

We reported that grain boundaries in CVD graphene severely weakened graphene membranes [1]. Our explanation, to attempt to reconcile theoretical predictions with our observations, was to consider a more realistic model where grain boundaries could include larger defects, rather than consisting purely of 5-7 defects, which are known to be stronger. Simulations on defected grain boundaries matched our experimental results.

We observed graphene tearing along identified grain boundaries and we concluded that tears in graphene membranes would be more likely to begin at a boundary, and then an “unzipping” process would result in tearing continuing along

the boundary. On the other hand, K. Kim *et al.* [2] have also reported that graphene tears preferably occur along ziz-zag or armchair directions, largely ignoring grain boundaries as tearing can be observed to continue across them. Further theoretical modeling added one more piece to the puzzle, as J. Kotakoski and J. Meyer [3] pointed out that the intersection of grain boundaries are particularly weak, and further explain the dramatic decrease in the breaking force in polycrystalline graphene.

We believe that a combination of factors, including those reported by other research groups, will determine the mechanical failure of graphene membranes. Future work is needed to also explain the role of defects in the mechanical properties of other polycrystalline 2D materials.

7.1.2 Towards crystal size control

As previously noted in Chapter 5, being able to easily determine CVD graphene's polycrystalline structure, immediately provides feedback to adjust

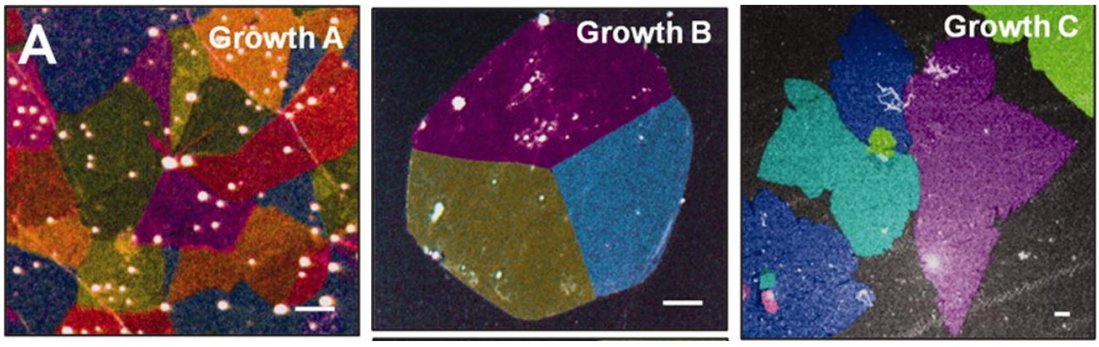

Figure 7.1 Composite false-color DF-TEM images of CVD graphene produced using three different growth conditions—A, B, and C—yielding average domain size *D* of 1, 10, and 50 μm, respectively, in continuous films (from [4]).

graphene growth parameters, and obtain larger graphene crystallites. For example, as shown in Figure 7.1, various growth conditions result in different graphene grain sizes and shapes [4]. In general, high reactant flow rates produce faster growth, and a larger amount of nucleation sites. As a result, the average grain size is also smaller. On the other hand, restricting the amount of reactants [5], for example by utilizing an enclosure around the copper foil during growth, will result in a more controlled environment for slower graphene growth, as well as less nucleation sites.

In agreement with previous findings [6], grain boundaries formed under highly reactant conditions were found to be highly conductive, and appropriate for high-performance devices (with high carrier mobilities). On the other hand, grain boundaries formed during slower graphene growths yielding larger grains, were found to be often composed of overlap or amorphous graphene layers, terminating growth rather than forming well defined boundaries composed of line-defects [4]. We expect that this compromises the mechanical strength of membranes composed of large crystal domains.

The size of CVD graphene grains was once a cause for greater concern. It is now known that fast growing conditions can yield higher-quality grain boundaries, and CVD graphene appropriate for many potential applications, such as graphene windows as described in Chapter 6). Films with small graphene domains but higher-quality grain boundaries are often preferable to larger graphene domains with poorly "stitched" boundaries.

7.2 Outlook

The techniques described in this thesis have been important in the characterization of graphene. Going forward, the properties of CVD graphene will continue to be tailored and improved, inching closer towards the actual incorporation of this material in actual applications.

The methods described in this thesis (for synthesis, fabrication and characterization) will likely continue to be revised, but the lessons learned are not specific to CVD graphene. The work in this thesis focused entirely on graphene, but it sets forth one of many possible paths in the study and development of other 2D materials, such as boron nitride and molybdenum disulfide just to give two well known examples [7,8], as well as the integration of many of these promising 2D materials into hybrid structures [9] with new and exciting functionalities.

REFERENCES

[1] C. Ruiz-Vargas*, et al.* Nano Lett. **11**, 2259 (2011).

[2] K. Kim*, et al.* Nano Lett. **12**, 293 (2012).

[3] J. Kotakoski*, et al.* Phys. Rev. B **85**, 195447 (2012).

[4] A. W. Tsen*, et al.* Science **336**, 1143 (2012).

[5] X. Li*, et al.* J. Am. Chem. Soc. **133**, 2816 (2011).

[6] P. Y. Huang*, et al.* Nature **469**, 389 (2011).

[7] DeanC. R.*, et al.* Nat Nano **5**, 722 (2010).

[8] RadisavljevicB.*, et al.* Nat Nano **6**, 147 (2011).

[9] M. P. Levendorf*, et al.* Nature **488**, 627 (2012).